The First 2.5 Years of HETE: Toward an Understanding of the Nature of Short and Long Duration Gamma-Ray Bursts

by

Nathaniel Richard Butler

Submitted to the Department of Physics
in partial fulfillment of the requirements for the degree of

Doctor of Philosophy in Physics

at the

MASSACHUSETTS INSTITUTE OF TECHNOLOGY

September 2003

Author .....
Department of Physics
August 29, 2003

Certified by .....
George R. Ricker
Senior Research Scientist, Center for Space Research
Thesis Supervisor

Accepted by .....
Thomas J. Greytak
Chairman, Department Committee on Graduate Students

The First 2.5 Years of HETE: Toward an Understanding of the Nature of Short and Long Duration Gamma-Ray Bursts

by

Nathaniel Richard Butler

Submitted to the Department of Physics
on August 29, 2003, in partial fulfillment of the
requirements for the degree of
Doctor of Philosophy in Physics

Abstract

The HETE satellite became operational on the 2nd of February, 2001. In the first 2.5 years of the mission prior to July 1 of 2003, 42 Gamma-ray bursts (GRBs) were promptly localized and publicized over the GRB Coordinates Network (GCN). The first part of this thesis deals with the detection of GRBs in data down-linked from the HETE satellite using a suite of automated routines. This "ground triggering" was designed to supplement the HETE on-board triggering systems. To date, it has facilitated the broadcast of six HETE GRBs to the GCN. A novel trigger search routine using wavelets, which is included in the suite, is discussed. Near real time searches for very long duration (> 300s) GRBs using this and other methods are presented. The second part of the thesis focuses on imaging observations with Chandra of two GRB X-ray afterglows and high-resolution spectroscopic observations of five GRB X-ray afterglows. The imaging observations explore the nature of the class of short/hard GRBs and the class of "optically dark" GRBs, while the spectroscopic observations probe the relation of the long/soft class of GRBs to supernovae. Our observations suggest that no long/soft GRBs are optically dark. Rather, many appear to be "optically faint." In one case, a short/hard GRB may have been optically dark, because it lacked entirely an afterglow in the optical, radio, and X-ray bands. Finally, If the emission lines we detect in a Chandra spectrum of the X-ray afterglow to GRB 020813 are real, then a supernova likely occurred $\gtrsim 2$ months prior to the GRB. The statistical significance of the discrete spectral features reported to date in high resolution spectra taken with Chandra are discussed in detail, as the believability of the features is critical to moving forward in the field.

Thesis Supervisor: George R. Ricker
Title: Senior Research Scientist, Center for Space Research

Acknowledgments

I am severely indebted to my advisor, George Ricker, for guidance and support over the last five years. Thanks also to Saul Rappaport, Walter Lewin, and Erik Katsavounidis for being indispensable critics and for serving on my thesis committee.

None of this work would have possible without the tremendous spirit of cooperation, learning, and humor within the HETE operations team. I thank Geoff Crew, Bob Dill, Jon Doty, Allyn Dullighan, Jean Farewell, Glen Monnelly, Gregory Prigozhin, Roland Vanderspek, and Joel Villasenor at MIT for every bit of your help. Also, of our collaborators at other institutions, Carlo Graziani, Kevin Hurley, Garrett Jernigan, and Don Lamb have been essential and wonderful to work with.

Special thanks to Peter Ford for his crucial role in facilitating the arrival of every byte of our Chandra data. And thanks to Herman Marshall for his expert guidance in the analysis of spectra with Chandra.

Thanks to everyone, previously unmentioned, at the MIT CSR.

Work doesn't happen without home, and I have so many to thank for making home such a wonderful place while I've been at MIT. Thanks to the Millstone Co-op, Somerville, MA, and thanks to everyone who lives or who has lived there. Thanks especially to Basak Alkan, Monica Aufrecht, Bailey, Sarah Bertucci, Molly Graves, Micha Josephy, Adam Kessel, Kelly McCoy, Mike Reed, Ransom Richardson, Eowyn Rieke, Pete Rowinsky, Sarah Shamel, Simon, Nate Smith, Scarlet Soriano, Dylan Thurston, and Nirmal Trivedi. Thanks also to my friend Erin Kirkpatrick for loving kindness.

Finally, thanks family, mother Helen, father Richard, brother Tyler, sister Jordan, grandparents William and Mary, all you aunts, uncles, cousins in Clearfield, and elsewhere. I'll visit soon! And thank you to every single member of the Pagans, Worf, and Ninja.

Contents

List of Figures

List of Tables

Chapter 1

Overview: GRB Detection with HETE and From the Ground

1.1 Thesis Overview

The High Energy Transient Explorer (*HETE*) satellite was launched into equatorial orbit on October 9, 2000 and became fully-operational on February 2, 2001 (Ricker et al., 2001). It is dedicated to the study of Gamma-ray bursts (GRBs) using instruments sensitive in the soft X-ray (2-10 keV), X-ray (2-25 keV), and Gamma-ray bands (30-400 keV).

GRBs were first detected in 1969 by the Vela satellites (Klebesadel et al., 1973). From then until the mid 1990's, thousands of GRBs were detected by experiments like *BATSE*, *GINGA* (Strohmayer et al., 1998), and satellites taking part in the Interplanetary Network (IPN) (see, e.g., Hurley et al., 2002). The Burst and Transient Source Experiment (*BATSE*) (Fishman et al., 1989) detected some 2704 GRBs between 1991 and 2000 and carried out the detailed study of their prompt emission properties. *BATSE* determined that GRBs occur approximately once per day, and that they form a uniform distribution on the sky (Figure 1-1). Due to the relatively poor localization accuracy of *BATSE* ($\gtrsim 1$ degree), however, and also due in part to the theoretical concerns over the extreme energy release common in GRBs ($\sim 10^{52}$ erg at $z = 1$), it was not widely accepted that GRBs were cosmologically distant

until the mid 1990's. The Dutch/Italian satellite *BeppoSAX* (Jager et al., 1997, and references therein) was able to localize and slew to a number of GRBs in 1997 (see, e.g., Costa et al., 1997), finding that each burst was succeeded by an "afterglow" in X-rays. *BeppoSAX* determined positions for the afterglows with $\sim 1'$ accuracy, and this enabled optical observers to establish that the GRB host galaxies were at high redshift ($z \gtrsim 1$) (see, e.g., Metzger et al., 1997). The afterglows are observed at energies ranging from radio to X-ray. In some cases, they can be observed for months, before fading to obscurity. In all cases, there is an incredible, frenzied rush to detect and study the afterglow while it is bright. By studying its multi-wavelength emission, it is possible to unlock a treasure-trove of information about GRBs and their host environments.

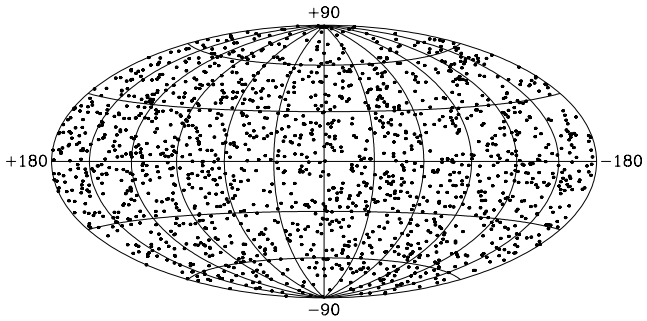

Figure 1-1: Early strong evidence for the cosmological origin of GRBs came from the *BATSE* experiment. This plot shows an isotropic spatial distribution for the 1637 bursts in the 4Br (4th *BATSE*, revised) catalog on an Aitoff-Hammer projection in Galactic coordinates, taken from Paciesas et al. (1999).

The first part of this thesis (Section 1.4.1 below and Chapters 2 and 3) deals with the detection of GRBs in data downlinked from the *HETE* satellite using a suite of automated routines. This "ground triggering" was designed to supplement the *HETE* on-board triggering systems. It will become clear that this work deemphasizes to some degree the prompt emission properties of the bursts, while focusing on increasing the number of rapidly localized GRBs suitable for afterglow studies. Thanks in large part to *BATSE*, the GRB prompt emission has been well-studied. However, the lack of GRB host redshifts and the resulting ignorance of the precise GRB energy budget made these studies incomplete. Current efforts are primarily focused on prob-

ing the afterglows. The second part of the thesis focuses on imaging observations with *Chandra* of two GRB X-ray afterglows (Chapter 4) and high-resolution spectroscopic observations of five GRB X-ray afterglows (Chapters 5 and 6). The imaging observations explore the nature of the class of short/hard GRBs and the class of "optically dark" GRBs, while the spectroscopic observations probe the relation of the long/soft class of GRBs to supernovae (SNe).

1.2 Science Overview

1.2.1 "Optically Dark" and Short/Hard GRBs

More than half of all GRBs to date have been "optically dark" (see, e.g., Berger et al., 2002). This term refers to bursts which are detected in prompt emission with reliable localizations allowing for rapid optical followup, but for which optical afterglows are not detected. *HETE* has discovered and rapidly disseminated localizations for several GRBs, which would have previously been categorized as optically dark GRBs (Section 4.2). For example, *HETE* trigger 2493 (Crew et al., 2002) and the rapid optical follow-up observations of GRB 021211 (see, e.g., Fox et al., 2002; Park et al., 2002; Li et al., 2003; Wozniak et al., 2002) demonstrate that, for some GRBs, the optical afterglow at early times ($\gtrsim$1 hour) can be much fainter than previously thought. Thus, the burst afterglows appear to be intrinsically faint in the optical. Two other popular explanations for the optically dark GRB phenomenon involve intrinsic properties of the GRB host galaxy. First, the GRB may lie at very high redshift ($z > 8$), in which case the optical afterglow is expected to be absorbed by neutral hydrogen along the line of sight. No such GRB hosts have been confirmed to date, though it is suspected that they may be present out to redshifts as high as $z \approx 20$ (see, e.g., Lamb & Reichart, 2000; Bromm & Loeb, 2002). In the second explanation, the GRB optical afterglow is extinguished by dust near the GRB host or in a star-forming region within the GRB host (see, e.g., Lamb, 2000; Reichart & Price, 2002). The *HETE* (Kawai et al., 2002) detections and the rapid optical and IR follow-up observations of GRB 030115 (see,

e.g., Levan et al., 2003; Bourban et al., 2003) suggest that the optical afterglow of this burst is just such a case. Clearly, optically dark bursts are interesting for probing the intrinsic properties of GRBs and their host galaxies.

As the optical emission from these bursts is expected to be undetectable or extremely difficult to detect, observers must turn to other wavelengths. *BeppoSAX* was able to detect and slew toward several GRBs, observing the X-ray afterglows ∼2-3 hours after the GRB. These observations are consistent with all GRBs having X-ray afterglows (see, Costa et al., 1999). Working with Peter Ford, George Ricker, Roland Vanderspek (MIT), Don Lamb (U. Chicago), Garrett Jernigan, and Kevin Hurley (U.C. Berkeley), I have exploited this fact in three ToO ("target of opportunity") campaigns using *Chandra* in two epochs to detect fading X-ray afterglows. A second epoch is important because the afterglow may not be differentially brighter than typical field objects, and the second epoch confirms that a candidate object from the first epoch has faded in flux. We time the two epochs so that the decrease in brightness of the afterglow over the inter-observation period is greater than likely fluctuations in typical field objects (e.g. AGN). Our first attempt with *Chandra*in December of 2001 (GRB 011130, Ricker et al., 2001a; Monnelly et al., 2001; Butler et al., 2002) was unsuccessful, possibly because the very large *HETE* error region did not allow for the GRB to be within the *Chandra* field-of-view. The GRB 011130 observations are explained in detail in Monnelly (2002). Our second attempt in June of 2002 was also unsuccessful, though it yielded extremely important constraints on the afterglow of the very interesting short/hard GRB 020531 (Section 4.1). However, our third (Section 4.2) and fourth (Butler et al., 2003a,b) attempts in May of 2003 and in July of 2003 were successful. The analyis of the burst in July of 2003 (XRF 030723) is still underway and is not discussed in this thesis. Finally, Fox (2002b,c) employed a strategy very similar to ours to detect the probable X-ray afterglow of GRB 020127 (Ricker et al., 2002).

As displayed in Figure 1-2, the sample of *BATSE* bursts contained in the 4Br catalog appears to separate into two duration classes, with the dividing line around $t_{50} = 1.0$s. Here t_{50} is the time from the start of the bursts at which point 50%

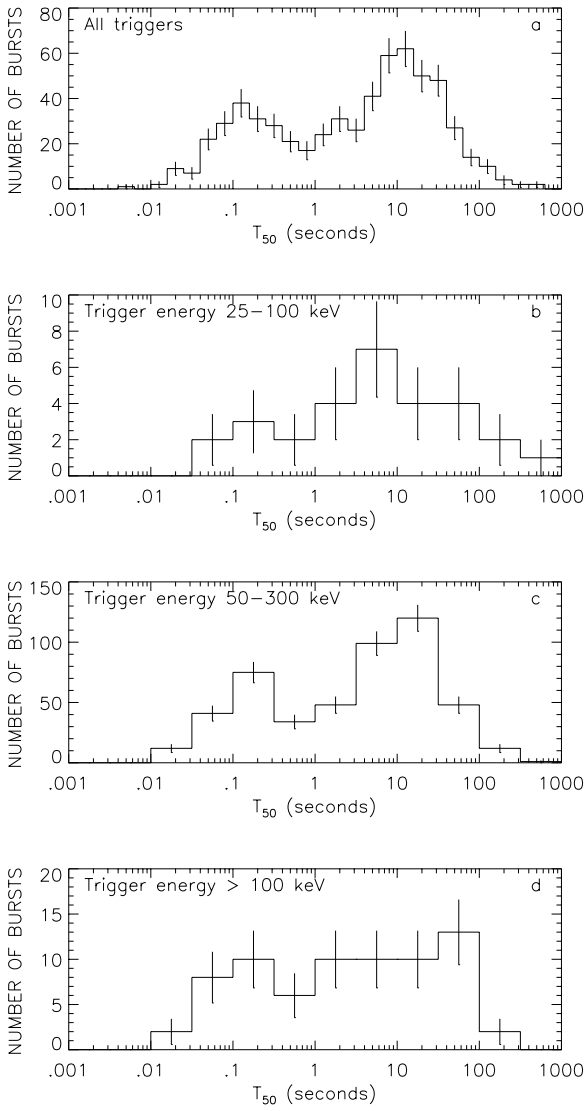

Figure 1-2: The separation of GRBs into two duration classes (short/hard and long/soft GRBs) is indicated by the presence of two populations in the *BATSE* catalogs. Here the t_{50} distributions for events in the 4Br catalog (Paciesas et al., 1999) are plotted. a) all bursts, b) trigger energy range 25–100 keV, c) trigger energy range 50–300 keV, d) trigger energy range $>$ 100 keV.

of the total burst counts have been detected. Approximately one-third of all the *BATSE* events have $t_{50} \lesssim 1.0$s, and this fraction increases when the high-energy triggers are considered alone. This provides evidence for a class of short/hard GRBs, as recognized in the early 1990s (see, e.g, Hurley et al., 2002; Kouveliotou et al., 1993). It is has been postulated that short/hard GRBs may lack bright afterglows at all wavelengths due to their possible association with compact mergers (see, e.g., Eichler et al., 1989). These objects are likely born with large peculiar velocities that move them far away from the region in which they were formed, resulting in potentially very clean circumburst environments. This picture is supported by our non-detection and strong upper limits for the afterglow to GRB 020531 (Section 4.1.3). Long/soft GRBs are thought to arise in more dense regions where star formation is active. Evidence tying these GRBs to SNe is essentially air-tight (Section 1.2.2).

1.2.2 Long/Soft GRBs and Supernovae

Much evidence has accumulated in recent years connecting long/soft GRBs to SNe. The detection of SN 1998bw in association with GRB 980425 (Galama et al., 1998) and the detection of late-time SN "bumps" in several afterglow light curves (Bloom et al. (1999), Reichart (2001) and references therein), the observed positional coincidences between star-forming regions and long-duration GRB afterglows (e.g. Sahu et al. (1997), Kulkarni et al. (1998), Kulkarni et al. (1999)), and the evidence for dust extinction in some GRB afterglows all pointed toward this association. With a clear Type 1c SN signature detected in the afterglow spectrum (Stanek et al., 2003; Khokhlov et al., 1999; MacFadyen, Woosley, & Heger, 2001) of the bright, nearby GRB 030329 discovered by *HETE* (Vanderspek et al., 2003a), the association is now air-tight. In this context, X-ray spectroscopic observations of early GRB afterglows are tremendously interesting, because they potentially allow us to view directly the effects of the GRB on the progenitor stellar material and possibly on metals freshly synthesized in the SN.

Several authors have claimed detection of Fe lines in GRB X-ray afterglows (Piro et al. (1999), Piro et al. (2000) (Section 6.3), Antonelli et al. (2002)). Beyond very

weak evidence in Piro et al. (2000) for an emission line from H-like S in GRB 991216, Reeves et al. (2002) were the first to strongly assert evidence for emission from light, multiple-α elements (e.g. Mg, Si, S, Ar, Ca) in a GRB X-ray afterglow. If valid, this claim has broad implications for GRB emission models and it would strongly link GRBs to SNe. The reduction of these data and the statistical significance of the results has been called into question by Borozdin & Trudoyubov (2002) and Rutledge & Sako (2002), respectively. In a follow-up paper (Reeves et al., 2002b), the *XMM-NEWTON* (Jansen et al., 2001) observers address those concerns. Physical interpretations aside, the Reeves et al. (2002) results are controversial largely due to the small number of observed counts and the low spectral resolution of the EPIC-pn instrument, which would blur some fraction of the line emission into the continuum. These hinder an accurate measurement of the continuum emission and make it difficult to gauge the significance of discrete spectral features.

Recently, Watson et al. (2003) have claimed detection of line emission from light elements similar to that of Reeves et al. (2002) in the afterglow spectrum of GRB 030227 taken with *XMM-NEWTON*. The significance of these lines appears to be somewhat greater than that of the Reeves et al. (2002) lines, though the concerns of the preceding paragraph are likely valid here as well. In Figure 1-3, I show the spectra taken from the literature for all of the X-ray afterglow lines reported to date. The data for all but two bursts (GRB 991216 and GRB 020813) are CCD (Charge Coupled Device) imaging data, rather than high-resolution X-ray spectrometer grating data. As a result, the features appear broad, and it is not clear what portion of the broadening is due to intrinsic line width and what portion is due to smearing of the line profiles by the CCD detector response. Until there is a high significance (reliably $> 5\sigma$) detection of discrete spectral features in a GRB X-ray afterglow, the statistical validity of each of these measurement will be a critical question. Though the shear number of observations may appear to favor their likely validity, any given line detection remains uncertain. Thus, we cannnot be confident of the apparent diversity of circumburst environments which have been inferred until we have strong detections.

Lines from CCD imaging data are difficult to validate because the continuum is

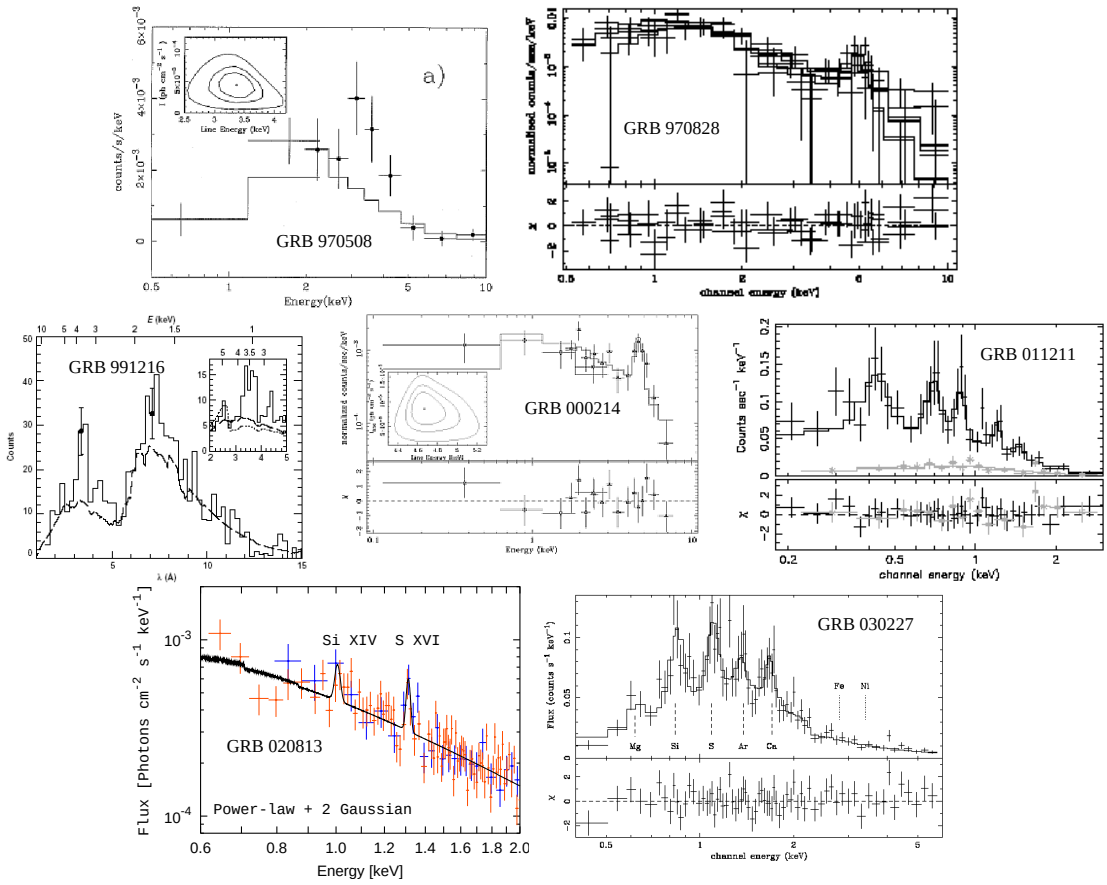

Figure 1-3: Several low ($\sim 3\sigma$) to moderate significance ($\lesssim 5\sigma$) emission lines have been reported in the literature. From top left to bottom right, Fe lines have been reported in the X-ray afterglows of GRB 970508 (*BeppoSAX*) (Piro et al., 1999), GRB 970828 (*ASCA*) (Yoshida et al., 1999), GRB 991216 (*Chandra* high resolution) (Piro et al., 1999), and GRB 000214 (*BeppoSAX*) (Antonelli et al., 2002), while light metal lines have been reported in the X-ray afterglows of GRB 011211 (*XMM-NEWTON*) (Reeves et al., 2002), GRB 020813 (*Chandra* high resolution) (Section 5.3.3), and GRB 030227 (*XMM-NEWTON*) (Watson et al., 2003). Line emission has also been claimed for the *XMM-NEWTON* spectra of GRB 010220 and GRB 001025A, though these are apparently of low significance and no discernible plots are available in the paper by Watson et al. (2002).

often blended with the lines. X-ray gratings spectrometer data do not suffer from this limitation, though the gratings spectra often have considerably fewer counts, rendering the lines statistically less significant than they otherwise might be. Working with Herman Marshall, George Ricker, Roland Vanderspek, Peter Ford, Geoff Crew (MIT), Don Lamb (U. Chicago), and Garrett Jernigan (U.C. Berkeley), I have reduced the *Chandra* High Energy Transmission Gratings Spectrometer (HETGS) (Canizares et al. (2002), Weisskopf et al. (2002)) data for GRB 020813 and GRB 021004. In Section 5.3.3, we discuss candidate lines we detect in a *Chandra* high-resolution gratings spectrum of GRB 020813. As the continuum is clearly separable from the line emission, our result is probably the cleanest detection of emission lines to date. We discuss the interpretation of the candidate lines in that section. We have also reduced the spectrum of GRB 021004, also taken with the *Chandra* HETGS. In Chapter 6, I apply the techniques used to establish the GRB 020813 lines to other high resolution spectra taken with *Chandra*. Only for GRB 991216 have lines been claimed in the literature, and this claim depends somewhat on the CCD imaging data in addition to the gratings data.

1.3 HETE Overview

HETE detects GRBs and localizes the X-ray (2-25 keV) component of the prompt emission, rapidly disseminating the localization to the ground to facilitate followup observations. As the crucial first link in a world-wide network of GRB research facilities, *HETE* enables the real-time study of GRBs and their afterglows. Here I briefly summarize the *HETE* instruments from which measured data will be important in later sections. Three instruments on-board *HETE* detect and/or localize GRBs. These and the other *HETE* instruments are coordinated with one another and with the spacecraft via eight Motorola 56001 digital signal processors (DSPs), with a simple operating system developed at MIT (Doty et al., 2003). In addition, four Inmos T805 Transputer processors (which have greater memory capacity than the Motorola 56001 DSPs) are utilized to store data and to run processor-intensive code. All commands

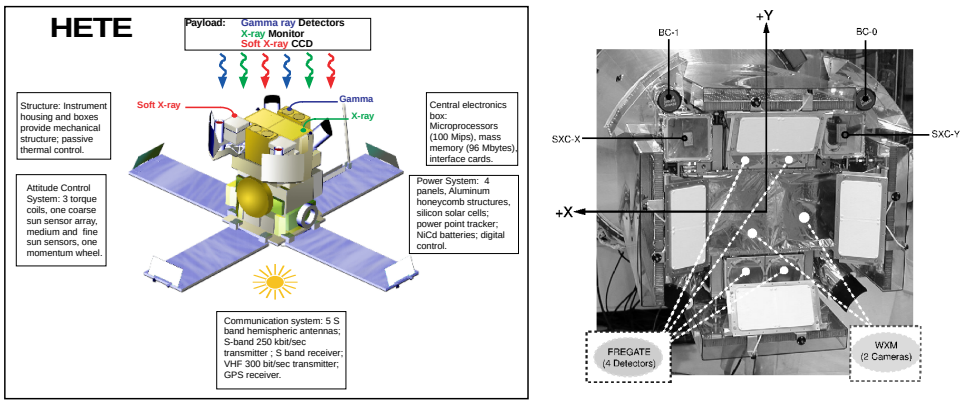

Figure 1-4: The left panel shows a sketch of the *HETE* satellite. In this view, the two pairs of units comprising FREGATE are located on the lower left and the upper right of the top face of the satellite (labelled "Gamma"); the two 1-D masks and detectors comprising the WXM are located at the upper left and lower right of the top face of the satellite (labelled "X-ray"); and the two cube-shaped units comprising the SXC are located at the left and bottom corners of the top face of the satellite (labelled "Soft X-ray").
The right panel shows the instrument face of the *HETE* satellite. In this view, the two pairs of circular detectors comprising FREGATE are labeled "FREGATE (4 Detectors);" the two 1-D masks and detectors comprising the WXM are located in the center of the picture and are labeled "WXM (2 cameras);" and the two square units comprising the SXC are located at the upper left and upper right corners of the picture and are labeled "SXC-X" and "SXC-Y."

(uplink, downlink, within the satellite, etc.) are issued using a common packet format.

Most sensitive in the Gamma-rays, the French Gamma-ray Telescope (FREGATE) (Atteia et al., 2003) is set of four cleaved NaI scintillators with a very wide ($\sim$ 4 steradian) field-of-view and a sensitivity over the energy range 6-400 keV (Table 1.1). Each detector is operated and read-out by its own analog and digital electronics. Within the analog circuitry, a discriminator with four adjustable channels and a 14-bin PHA (Pulse Height Analyzer) encodes the detected energy of each photon with associated dead times of 9 and 14 μs, respectively. In addition to the output of spectral data, time histories are output in four energy channels every 20ms. A circular buffer with high time (6.4μs) and energy (0.8 keV) resolution is also maintained and dumped for flight triggered GRBs. The FREGATE hardware triggering system is described in Section 1.4.1.

FREGATE triggers on GRBs as count rate increases, as does the Wide Field X-ray Monitor (WXM) (Kawai et al., 2003). The WXM triggers on the 1-25 keV

FREGATE performances	
Energy range	6 - 400 keV
Effective area (4 detectors, on axis)	160 cm^2
Field of view (FWZM)	70°
Sensitivity (50 - 300 keV)	10^{-7} erg cm^{-2} s^{-1}
Dead time	10μs
Time resolution	6.4μs
Maximum acceptable photon flux	10^3 ph cm^{-2} s^{-1}
Spectral resolution at 662 keV	$\sim 8\%$
Spectral resolution at 122 keV	$\sim 12\%$
Spectral resolution at 6 keV	$\sim 42\%$

Table 1.1: FREGATE performance and instrumental characteristics from Atteia et al. (2003).

band over a 1.6 steradian field-of-view, and it is also used as a localizing instrument (Table 1.2). It consists of two identical Position Sensitive Proportional Counters (PSPCs), each containing Xenon gas (and 3% CO_2 for quenching) and three carbon fibre anode wires and four tungsten wires. The PSPCs are mounted below a coded mask, which produces a shadow pattern on the wires and allows for positions (typically 5-10$'$ accurate) to be determined by correlating the mask pattern with the detected counts. In addition to housekeeping and spectral data, the WXM generates time history data in four energy bands every 80ms and position histogram (imaging) data in two energy bands every 320ms. The time histories are searched for bursts in flight using the software triggers discussed in Section 1.4.1.

Within a WXM error region, the Soft X-ray Camera (SXC) (Villasenor et al., 2003) is used as a fine vernier. Both the WXM and the SXCs are crossed 1-dimensional imagers using coded masks. For each of four SXC units, a coded mask is mounted atop a CCD. Each CCD is a front-sided CCID-20 2048×4096 array with $15 \times 15\mu$m pixels (Table 1.3). Data from each are summed along the CCD columns over 1.2s integration intervals. Due to the loss of two SXC units from the erosion of their optical blocking filters by atomic oxygen, only two units are currently operating. The SXC typically localizes to 1-2$'$ accuracy (over a 1.3 steradian field-of-view) using

Wide Field X-ray Monitor	
Built by	RIKEN and LANL
Instrument type	Coded Mask with PSPC
Energy range	2 - 25 keV
Timing Resolution	1ms
Spectral Resolution	$\sim 25\%$ @ 20 keV
Detector QE	90% @ 5 keV
Effective Area	~ 175 cm^{2*}
Sensitivity (10σ)	$\sim 8 \times 10^{-9}$ erg/cm^2/s (2-10 keV)
Field of view (FWZM)	1.6 steradians
Localization resolution	$19'$(5σ burst)
	$2.7'$(22σ burst)

Table 1.2: WXM performance and instrumental characteristics from Kawai et al. (2003). * each of two units

photons in the 2-10 keV band. It is not a GRB time series triggering instrument as are FREGATE and the WXM.

General SXC parameters	
Camera Size	$100 \times 100 \times 100$ mm
Instrument type	Coded Mask with CCID-20
Field of View	0.9 sr (FWHM)
Angular Resolution	33 ″per CCD pixel
Detector-Mask Distance	95 mm
Mask Open fraction	0.2
Mask element size	45 μm
Timing Resolution	1.2s

Table 1.3: SXC performance and instrumental characteristics from Villasenor et al. (2003).

Finally, *HETE* uses optical cameras to relate instrumental positions to positions on the sky by tracking stars. The positions are transmitted at VHF frequencies down to one of approximately a dozen autonomous ground stations along the equator (Villasenor et al., 2003a) in transit to the mission command and control center at MIT. From MIT, valid burst positions are conveyed over the internet to the astronomical community via the GRB Coordinates Network (GCN) at Goddard (see e.g. Vanderspek et al., 2003). *HETE* is currently localizing GRBs at a rate ~ 20 yr^{-1}. GRB

localization are routinely transmitted to the GCN in real time (i.e. during the GRB). In a few instances (e.g., Fox, 2002a) this rapid dissemination has enabled optical observers to find the GRB afterglow more rapidly (on the timescale of minutes) than the *HETE* science team has been able to manually view the downlinked data from *HETE*.

1.3.1 My Role in HETE

I have been working on various aspects of the *HETE* mission since coming to MIT in September of 1998. Prior to launch, I was involved in calibration and testing of the SXCs and the optical cameras. Around the time of the launch, I traveled to the remote Primary Ground Station (PGS) site on the Kwajalein Atoll (Figure 1-5) on a number of occasions, to prepare the ground station located there and to ready the satellite for launch. Post-launch, I have been primarily involved in verification efforts of the flight GRB triggering systems. As described below, I have developed an automated suite of routines which search for triggers once the down-linked data reaches MIT. I have also been intensely involved in carrying-out and planning observations of the optical, IR, and X-rays afterglows of *HETE*-discovered GRBs.

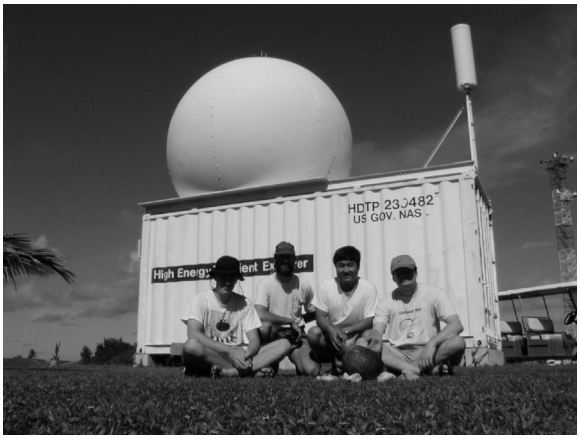

Figure 1-5: The *HETE* launch team at the Kwajalein Atoll remote PGS site. From left to right, Nat Butler, Geoff Crew, Joel Villasenor, and Bob Dill. Photo courtesy of Geoff Crew.

1.4 Ground Triggering Overview

1.4.1 HETE On-board GRB Triggering Systems

The FREGATE instrument can trigger independently over the 8-85 keV band ("Band B") and the 30-400 keV band ("Band C"). WXM triggers over the 2-25 keV band. As the *HETE* obserational strategy involves primarily anti-solar pointing, the field-of-view of each instrument during the Summer months (roughly May through August) tends to contain multiple known X-ray sources. Due to this, often only Band C triggering is enabled. This can also be the case during periods of excessive solar activity, as discussed in Section 3.1. When a significant count rate increase is found and a trigger is declared, the DSP associated with the WXM (Section 1.3) works to find an optimal burst region and to localize the burst.

The FREGATE triggers are hardware triggers very similar to the triggers proven successful with *BATSE*. Four burst region durations are searched: 20 ms, 164 ms, 1.3s and 5.2s. Counts over each of the window durations are accumulated in a "leap frog" (stepsize 20ms) fashion as the data are accumulated. The counts are compared to a background sample accumulated in 5.2s pieces prior to the burst window. The time series data from each of the four FREGATE units is searched in this manner, and two 1-detector triggers within 1.3s are required to declare a trigger based on preset count thresholds. Also, rising background trends are tested for on a regular interval, and if the background under a trigger is found to be rising beyond a preset threshold, the trigger is declared invalid.

As evidenced by the success of *BATSE* untriggered burst searches (Stern et al., 2001, and references therein), trigger schemes like the one in the preceding paragraph can be insensitive to various burst temporal morphologies. In particular, if significant power is not present on timescales as short as the burst windows, a trigger may well be missed. Though a test is made for background trends, false triggers are also more likely when the background is varying. As a result, flight trigger treshholds must be set conservatively. The triggers for WXM are software triggers designed to be versatile and commandable in order to overcome the shortcomings of the *BATSE*-like trigger

(Tavenner et al., 2003). They can be applied to both the WXM and FREGATE Band C data (summed across detectors).

The WXM system works by defining a set of trigger "criteria" and "types." The type is either 0 (disabled), 1 (fully-enabled) , or 2 (updating-only). The type 2 triggers are only invoked if a type 1 trigger has previously fired, in an attempt to find a more optimal (higher S/N) burst duration region. The trigger criterion refers to the durations of the burst region and the background region(s). Some of the criteria have background regions accumulated prior to and after the burst. These are more stable under background fluctuations, but they require more time for data accumulation and are thus slower to report bursts than single background accumulation triggers. Several criteria are tested simultaneously, with burst windows ranging from 80ms to 27.2s. Often, only the double-background triggers are enabled, and these only search the FREGATE Band C data. The longest burst duration for such a trigger is approximately 10s. If a trigger is found, multiple type 1 and 2 triggers are tested to optimize the burst region, and this can extend (or contract) the burst region in time. When the orbit background is calm (i.e. no Galactic sources, no solar activity), triggering on longer timescales and at X-ray energies is enabled.

1.4.2 Motivation for Ground Triggering

To attempt to detect bursts missed by flight, either because the the flight triggers lacked sensitivity or were disabled, also to verify that the flight triggers were indeed working as planned early in the mission, I have developed a powerful, largely autonomous "ground triggering" system. As described below, the routines in the system search the *HETE* data (Table 1.4) once it reaches MIT for potential bursts. An outer layer plots all of the data, creates html, runs burst pipeline software normally run for flight-triggered bursts, and sends notification emails for discovered bursts. After this, a human must read his/her email and check the processing, possibly deciding to send a circular to the GCN.

Verification of the flight triggers has been necessitated in part by the complex, and flight-unproven system employed by the WXM (Section 1.4.1). Ground triggering has

made it possible to optimize the WXM triggers for somewhat longer burst durations than it had been initially able to detect by demonstrating that such bursts were present in the data (see e.g. Table 1.6). Ground triggering helped blow the whistle on a software bug which had disabled flight triggering entirely for approximately a month early in the mission.

As mentioned in Section 1.4.1, the flight triggers are occasionally disabled due to unpredicatable in-orbit backgrounds. On several instances, which I describe in more detail in Section 1.4.4, the *HETE* operations team has used ground triggering to perform various observational campaigns. On the ground, there are essentially no limits due to memory and computation (unlike flight). The data are therefore combed-through much more meticulously, and background variations are better accounted for. Overall, it is possible to increase *HETE*'s sensitivity to GRBs, while not over-inflating the false event rate. To date, my efforts have not focused on extending the sensitivity to lower S/N, as has been common in untriggered burst searches with *BATSE*. This is achieved to some extent, as the flight triggers are set somewhat conservatively in order to avoid a large number of false events. Primarily, however, I have been interested in bursts which are prominent enough for localization with the WXM (S/N$\gtrsim 7$), and these are characteristically relatively bright. These are discovered and propagated as rapidly as possible for further study. A broad class of these bursts, to which flight is potentially insensitive, are bursts with duration long relative to the flight burst detection windows ($\gtrsim$ 10s). If these are smooth on those timescales, flight will potentially miss them. Long bursts are also interesting because the total number of counts in the event can be large, and a localization is somewhat more probable than for shorter events. Ground triggering is insensitive to bursts with durations $\lesssim$ 100ms, due to telemetry restrictions on the data mass downloadable from the satellite, and these bursts must be found in flight.

1.4.3 Ground Triggering Implementation

The system is built upon three core routines into which time series data are piped and which detect bursts and report statistics for each burst. The first, "hete_wave"

(Chapter 2), is substantially different in approach from the flight trigger systems. The second, "drive-trigger", is similar to the flight systems, though downhill simplex optimization is utilized to increase sensitivity. This algorithm is described in Graziani (2003). The third algorithm, which I will wait until Section 3.3 to describe, focuses on long duration bursts. The first two routines are run on all of the data described in the next paragraph, while the third routine only operates on one particular WXM data product (6.6s resolution imaging data, Table 1.4).

Instrument	Type	Energy Range (keV)	Time Resolution
FREGATE	TH	6-40	160ms & 1.2s
FREGATE	TH	8-85	160ms & 1.2s
FREGATE	TH	30-400	160ms & 1.2s
FREGATE	TH	>400	160ms & 1.2s
WXM	TH	2-5	1.2s
WXM	TH	5-10	1.2s
WXM	TH	10-17	1.2s
WXM	TH	17-25	1.2s
WXM	POS	2-10	6.6s
WXM	POS	10-25	6.6s
SXC	POS	2-10	1.2s

Table 1.4: Several "survey" data products regularly telemetred to the ground from *HETE*are autonomously searched for bursts in ground triggering. "TH" designates time history data, and "POS" designates position histogram data which can be used for imaging.

Prior to searching for triggers, known systematic effects are cleaned from each data product (Table 1.4) and each data product is summed across detectors (4 FREGATE detectors, 2 WXM detectors) to increase sensitivity. The FREGATE data are searched over four energy bands (A 6-40 keV, B 8-85 keV, C 30-400 keV, D > 400 keV) and at two time resolutions (160ms and 1.2s). At the finer time resolution, the FREGATE data are prone to a particular systematic effect ("parasites") of unkown origin, elimination of which requires comparison between the four detectors prior to summation. The WXM data at a single time resolution (1.2s) are searched over four energy bands (2-5 keV, 2-10 keV, 10-25 keV, 2-25 keV). Data from the SXC are

plotted but not searched for triggers due to erratic instrumental backgrounds which require time-intensive cleansing.

The *HETE* orbital period is approximately 1.6 hrs, and data are downlinked from the satellite three times per orbit from one of the three Primary Ground Stations (PGSs). When the data reach MIT, they are promptly extracted to ascii format and added to a circular buffer containing data from the previous ten orbits. Data reach MIT $\sim$ 15min after the start of each contact. The trigger searches commence approximately 7.5min later and require approximately 2.5min to complete. This entails plot generation, the initiation of further analysis, and email notification for each burst trigger detected. The minimum response time is thus $\sim$ 25min. However, with typical PGS spacings of $\sim$ 45min, the maximum typical response time is $\sim$ 70 min. This does not include the time necessary for a human to review the trigger reports and to initiate additional analyses. Table 1.6 shows the times required for several bursts discovered in ground triggering to be manually propagated to the GCN as circulars. Ground triggering has detected all flight triggered GRBs with durations $\gtrsim$ 0.1s, and these are autonomously denied post-processing and notification.

The amount of post-processing a burst trigger receives, and whether or not notification for the trigger is sent-out, is dependent upon the trigger "score." This is a quantity set based on the number of independent instruments and energy bands for which the burst is detected, meant to convey the degree to which the burst is likely to be localizable. Automated localization software is run, though this is not typically consistent enough to allow one to conclude that a burst is localizable. The trigger score is set via the recipe in Table 1.5. This is initially done by correlating each of the triggers reported by the trigger search algorithms based on trigger time and event duration. The score is then verified by integrating a denoised (Section 2.3) version of the highest S/N detection against the signal in the other instruments and bands. This is compared against a quadratic background model to decide whether or not burst signal is present. Email notification is currently activated for scores 3 and higher only.

Score	Criterion
0	Weak Trigger
1	FREGATE Only
2	WXM Only or (FREGATE A and FREGATE C)
3	WXM and FREGATE A
4	WXM and FREGATE A and FREGATE C

Table 1.5: The ground trigger scoring system is designed to filter for WXM localizable bursts.

1.4.4 Results to Date

Prior to July 1, 2003, the localizations of forty-two *HETE* GRBs had been published in the GCN as circulars (Table 1.7). Circulars are verbose messages manually issued by the *HETE* team for each GRB with a trustworthy localization. These are to encourage followup observations of the GRB afterglow. A small, but important, fraction (6 of 42) of these bursts have been flight-untriggered bursts caught in ground analysis, as displayed in Table 1.6. These are several of *HETE*'s most important bursts, because they are frequently very soft (and rare) GRBs. Four of the six untriggered events in Table 1.6 were propagated by the automated ground trigger robots. The other two were detected, though they were not propagated over email. In one case, the burst S/N was too low. In the other, the burst occurred when *HETE* was passing through the South Atlantic Anomaly (SAA), and it was incorrectly deemed a false event due to particles. Both short-comings were compensated for by members of the *HETE* operations team.

Ground triggers for which FREGATE Band C emission is present result in the sending of automatic email notices to Dr. Kevin Hurley at Berkeley for autonomous correlation with observations made by satellites in the IPN. Dr. Kevin Hurley also manually reviews the *HETE* time series data for each to check that each is likely to be a GRB. In this manner, very hard GRBs unlocalizable by *HETE* can be localized by triangulation. Between October 2000 and December 2002, 144 untriggerd events were sent to and reviewed by Dr. Kevin Hurley. Approximately 70% of these were discovered by (or with the help of) my ground triggering software. Of the total

GCN#	Name	t_{50}	Comment	Time until GCN
1109	GRB 011019	8.6s	soft	12.1hrs
1194	GRB 011212	35.4s	disabled triggers	10.3hrs
1442	GRB 020625	24.7s	full moon	9.3hrs
1649	XRF 021021	26.2s	very faint/soft	17.1hrs
1888	GRB 030226	35.1s	over SAA	17.8hrs
2209	XRF 030416	8.4s	very soft	7.8hrs

Table 1.6: GCN Circulars have been issued for six flight-untriggered GRBs. All of these were detected by ground triggering and four (1109, 1194, 1442, and 2209) were autonomously propagated to the *HETE* operations team. In the "Comments" column I give a likely explanation for the lack of a flight trigger. An additional factor is the likely failure of the flight algorithm due to long GRB event duration (Section 3.1), in four of the six cases. The time between the GRB and the receipt of the GCN circular at Goddard is given in the "Time until GCN" column. Positions were sent to the GCN as (less verbose) "notices" (typically) a few hours prior to each circular.

number, 19 (13%) have been confirmed present in IPN satellite data. These numbers can be compared with the 189 total GRBs sent from *HETE* for correlation with the IPN, 96 of which were also detected by the IPN.

Ground triggering has also been used to monitor objects other than GRBs, to which the *HETE* operations team chose not to make the flight triggers sensitive. During the Summer months of 2001 and 2002, ground triggering was used to monitor and detect X-ray burst (XRB) sources in the Galactic bulge. The XRB event rate was simply too high for the onboard systems, and flight GRB detection efficiency would have been seriously reduced. Between the 21st of May 2002 and the 10th of August 2002, 350 XRBs were detected with S/N greater than 8 in the FREGATE 8-40 keV band. A large fraction of these (199) were localized to known XRB sources. No new XRBs were discovered. XRBs detected in the Summer of 2001 are discussed in Section 2.5. Also during the Summer of 2001, ground triggering was able to supplement the large number of Soft-Gamma Repeater (SGR) bursts detected by *HETE*. In addition to the fourteen SGR bursts detected by the flight trigger systems, twelve were found by the ground system. These bursts typically had durations < 1s and were missed by the flight triggers because they were too faint.

As discussed in Chapter 3, searches for very long duration bursts are also regulary

Name	Loc. Error	IPN?	XT?	OT?	RT?	z
GRB 030528	$2'$		y	y		
GRB 030519	$17'\times2'$	y				
GRB 030429	$2'$			y		2.65
GRB 030418	$14'$			y		
XRF 030416	$7'$					
GRB 030329	$2'$		y	y	y	0.168
GRB 030328	$2'$		y	y		1.52
GRB 030324	$7'$			y		
GRB 030323	$12'$			y		3.37
GRB 030226	$2'$		y	y		1.98
GRB 030115	$2'$			y	y	
GRB 021211	$14'$			y		1.01
GRB 021204	$29'$					
GRB 021113	$27'$	y				
GRB 021112	$20'$					
GRB 021104	$26'$					
XRF 021021	$20'$	y				
GRB 021016	$30'\times7'$	y				
GRB 021004	$2'$		y	y	y	2.3
XRF 020903	$16'$					
GRB 020819	$2'$	y				
GRB 020813	$1'$	y	y	y	y	1.25
GRB 020812	$14'$					
GRB 020801	$30'$					
GRB 020625	$32'\times18'$					
GRB 020531	$38'$	y				
GRB 020331	$10'$			y		
GRB 020317	$30'$					
GRB 020305	$25'$	y		y		
GRB 020127	$8'$	y	y		y	
GRB 020124	$19'$	y		y		
GRB 011212	$11'$					
GRB 011130	$40'$					
GRB 011019	$35'\times35'$					
GRB 010921	$20'\times15'$	y		y		0.45
GRB 010901	$240'$					
GRB 010629	$15'$	y				
GRB 010613	$60'\times20'$	y				
GRB 010612	$60'\times30'$	y				
GRB 010326B	$20'$					
GRB 010326	$20'$	y				
GRB 010213	$30'$					

Table 1.7: *HETE* detected and promptly distributed localization information for forty-two GRBs prior to July, 1, 2003. Fifteen bursts were also detected by one or more satellites participating in the IPN ("IPN?"). X-ray ("XT?"), optical (or IR) ("OT?"), and radio ("RT?") transients were detected for seven, sixteen, and five bursts, respectively. Observers were successful in determining redshifts ("z") for nine of the bursts. In the above table, adapted from http://www.mpe.mpg.de/∼jcg/grbgen.html (August 26, 2003), the localization error ("Loc. Error") is presented as the error region radius, except in the few cases where boxes were published.

performed in ground triggering.

Chapter 2

A Wavelet Triggering Algorithm

2.1 The GRB Triggering Problem

It is a popular witticism among GRB researches that "if you've seen one GRB light curve, you've seen one GRB light curve." Event durations are typically tens of seconds, though the shortest can last only milliseconds. The longest, continuously active GRB detected to date (*BATSE*'s GRB971208) (Connaughton et al., 1997; Giblin et al., 2002) lasted a couple of thousand seconds. Bursts can be faint and background-dominated or quite bright. Event profiles can be smooth or jagged, single or multiply peaked, triangular, boxy, rounded, etc. There is no canonical burst temporal profile, and algorithms designed to find bursts within noisy time-domain data must be flexible enough to account for this.

In counts data taken with a counting instrument, such as FREGATE or the WXM (Section 1.3), GRBs can appear with a sharp count rate increase or merely as a modest increase in the background count rate over some interval. If the counts data were binned such that this interval corresponded to the width of one bin, and if the counts from the GRB all fell more or less within that bin, then the event would appear as the sharpest rising edge. (When the binning is not so optimal, the significance of the trigger will in general be lower than the significance of the overall event.) A sample from the background after the GRB would help us determine whether or not the increase was due to an increase in the background, rather than due to a transient

event. Traditional GRB triggers employ this procedure by searching the time series data over a preset range of event timescales, comparing the event rate during the time corresponding to the test (or signal, or burst) bin to the background rate before and possibly after that bin. For the *BATSE* experiment, for example, the data were searched on 64, 256, and 1024 ms timescales for significant fluctuations from the background rate as determined from preceding bins only.

Search procedures like the broad class outlined in the above paragraph operate by calculating a test statistic at various points in the data set. This is typically a signal to noise (S/N) ratio. As count rates will always be high (>12/bin), the S/N will be nearly equivalent to the number of Gaussian distribution standard deviations describing the rarity of the event. More precisely, one typically calculates one of two figures of merit: data variance (DV) or model variance (MV). If the total number of detected counts over some burst interval is $S + B$ (total "signal plus background" counts), then the data variance is:

$$DV = \frac{S + B - < B >}{\sqrt{S + B + < B^2 > - < B >^2}},$$

where the background averages are calculated from data before and/or after the burst. The model variance is defined as:

$$MV = \frac{S + B - < B >}{\sqrt{< B > + < B^2 > - < B >^2}}.$$

Here, only the noise from the estimated background is included in the denominator, while the noise from both the burst region and background estimates are used for data variance. In general then, $DV \leq MV$. In the above formulas, the fact has been used that, for a Poisson random variable x, the variance ($< x^2 > - < x >^2$) is equal to the mean $< x >$. And the measured value for x is taken as an estimate for $< x >$. In the case of MV, one is asking the question, "assuming the measured background rate, how significant was the observed fluctuation?" This test for a false positive (disproof of the NULL hypothesis) yields the figure of merit commonly referred to as "significance" by statisticians. Unless otherwise noted, I will be referring to MV

when I refer to the significance of an event.

One additional way to calculate event significance, which falls midway between DV and MV, involves the variable y, defined as $y = \mathrm{Sqrt}(x)$, where $\mathrm{Sqrt}(\cdot)$ is the square-root transformation. Consider $\mathrm{Sqrt}(\cdot) = 2 * \sqrt{\cdot}$. It is straight forward to show by Taylor expansion of $y = \mathrm{Sqrt}(x)$ around $< x >$ that $< y^2 > - < y >^2 \approx 1$. Moreover, y is approximately normally distributed. As was not the case for x, the variance in y is independent of $< y >$. The estimated variance in the signal plus background will be equivalent to the estimated variance in the background only. That is, were one to calculate MV or DV with the variable y instead of x for each data bin, the same answer would be found. And this would fall between DV and MV calculated with the variable x. Write:

$$DMV = \frac{\sum y_{\mathrm{S+B}} - \frac{n_{\mathrm{S+B}}}{n_{\mathrm{B}}} \sum y_{\mathrm{B}}}{\sqrt{n_{\mathrm{S+B}} + \frac{n_{\mathrm{S+B}}^2}{n_{\mathrm{B}}}}},$$

where $n_{\mathrm{S+B}}$ is the number of data bins containing $y_{\mathrm{S+B}}$ and n_{B} is the number of data bins containing y_{B}. This figure of merit generally provides greater contrast than DV, and it can be useful in instances where the background is low and MV would become unstable. Also, it can be calculated by a simple correlation of the trigger function with the transformed data y. A *BATSE*-like trigger function is just a Heavyside function straddling the x-axis, with positive portion lasting $n_{\mathrm{S+B}}$ bins and negative portion lasting n_{B}. To get DMV by integrating this function against the data, two things must be required of the trigger function shape. First, the area under the negative portion must be equivalent to the area under the positive portion. Second, the entire area of the trigger function squared must be equal to unity. It will be clear below that these features are characteristic of wavelets useful in triggering.

A well known theorem in signal processing due popularly to Wiener (see e.g. Press et al., 1997, p. 547ff) has it that the optimal filter to apply to noisy data in order to search for a feature of known shape is the filter with same shape as the sought-after feature. Assuming that the variance in the background estimate is negligible, $DMV \approx \frac{1}{\sqrt{n_{\mathrm{S}}}} \sum y_{\mathrm{S}}$. Integrating the data against the optimal filter and subtracting

background in the same manner as the *BATSE*-like trigger, one finds $\sqrt{\sum y_S^2}$. This is always larger than or equal to DMV by the triangle inequality. We are left with a simple and powerful way to view the GRB triggering problem: one should correlate the data with trigger functions shaped as much like GRBs as possible. Unfortunately, though there are common GRB time profiles, there is no universal profile. Below, I will develop a powerful solution which uses components from a discrete wavelet transform to build complex burst profiles based on the data themselves.

2.2 Wavelets and the Discrete Wavelet Transform

Wavelets are functions in a Hilbert space, much like the sines and cosines of Fourier analysis. But unlike sines and cosines, wavelets are localized in time as well as in frequency. Just as Fourier analysis starts with a sine function, which is stretched from higher to lower frequency to produce the set of functions in the space, wavelet analysis relies on the stretching of a "mother" wavelet. The functions in wavelet analysis also involve shifts in time of the mother wavelet. Two examples of mother wavelets are shown in Figure 2-1. In general, one trades smoothness for compactness in selecting a mother wavelet. The examples in Figure 2-1 are represented on the shortest timescale (i.e. least stretching) by two and four numbers, respectively. These two examples are the simplest wavelets appropriate for use in a discrete wavelet transform (DWT). The DWT is useful because, like a Fast Fourier Transform (FFT), it can be computed rapidly. The wavelet functions also form an orthogonal basis, the set of which generally has simpler noise properties than the original counts data (see below).

When counts data with no rising or falling trends or bursts are convolved in time with one of the two shapes in Figure 2-1, the mean response is zero. This is because the area underneath the wavelets is zero. In triggering, it is often also sensible to require zero response to a linearly rising or falling signal. The first wavelet in Figure 2-1, which is the wavelet primarily used in this study, has this property. Temporally smoother (and less compact wavelets) are generated by requiring higher

order moments to vanish (Press et al., 1997, p. 593). To model burst profiles, which are often narrow and jagged, it is best to choose the most compact mother wavelet which is not overly sensitive to the typical data background variations. As the HETE in-orbit background is typically linear in time (Section 3.1), while rarely becoming curved on timescales $\lesssim$ 300s, I have chosen to focus on the four component Daubechies wavelet (DAUB4) (Figure 2-1). This mother wavelet also has a triangular shape when stretched which is reminiscent of common burst profiles.

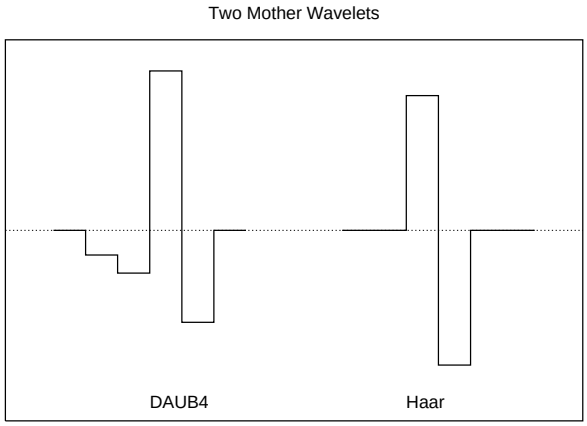

Figure 2-1: The simplest, and most compact wavelets used in the DWT. The left-most example is the 4-component Daubechies wavelet (DAUB4) (Daubechies, 1988). The wavelet on the right is the earliest known, and likely the simplest wavelet: the Haar (1910) wavelet.

Press et al. (1997) discuss the generation of mother wavelets of arbitrary shape. In general these will not have compact support (i.e. they do not go to zero beyond some finite interval). In order to pack them tightly enough to form a functional basis, there will be significant temporal overlap between wavelets in the basis, and this will lead to correlations when the transform is applied to noisy data. Moreover, less compact wavelets will less effectively fit potentially compact burst profiles. Linear independence (i.e. for the inner product: $< \psi_i | \psi_j >_{i \neq j} = 0$, with $< \cdot | \cdot >$ representing the overlap integral in time) makes it possible to view the set of wavelet functions as a set basis function into which the data can be decomposed $\Phi = \sum_i c_i \phi_i$. Here, the location in time and the scale (temporal stretching) of each wavelet is described by the single index i. Wavelet coefficients $c_i =< \phi_i | \Phi >$, which are the results of correlating

a particular wavelet term with a data set Φ, are statistically uncorrelated if the wavelet terms are linearly independent and the data set contains only uncorrelated (from bin to bin) noise. The coefficients are statistically independent if the noise is statistically independent from bin to bin (e.g. Gaussian or Poisson noise). As discussed below, statistical independence of the c_i's makes it simple to build arbitrarily complex wavelets from linear combinations of the basis terms. Without statistical independence, it would be necessary to perform $O(N^2)$ (rather than $O(N)$) operations to determine the error bar for each sum of wavelet coefficients.

One can gain a simple, intuitive picture of the DWT by considering a pyramidal implementation using the Haar mother wavelet. Start on the shortest timescale and correlate the data with the Haar wavelet. That is, maintaining the ordering of the data array of length N, pair adjacent bins, and calculate the N/2 differences for each pair. This yields N/2 pieces of "detail" information. The N/2 averages for each pair are also calculated as "smooth" information in the data. Next, repeat the procedure for the N/4 pairs of the data averaged in the previous step, storing the differences and continuing onward with the means. In this fashion, one calculates the detail information on dyadic duration scales 1, 2, 4, etc. If we write $H(t, s)$ for this Haar differencing operator of duration scale s, then the transform to the wavelet coefficients $c_i = c(\tau, s)$ can be written as:

$$c(\tau, s) = \frac{1}{\sqrt{2s}} \int_{\tau-s}^{\tau+s} H(t, s)\Phi(t)dt = \frac{1}{\sqrt{2s}} \left\{ \int_{\tau-s}^{\tau} \Phi(t)dt - \int_{\tau}^{\tau+s} \Phi(t)dt \right\}.$$

To attain the N c_i's of the DWT, calculate the overall mean of the data and evaluate the above integral for each s between 1 and N-1, $N/(2s)$ times on a grid of $2s$ bins separation per scale s. The relative placing τ between grids at different s is set so that the more compact terms overlap only with the positive or negative portion of the less compact terms, ensuring linear independence. Clearly, this transformation and the pyramidal implementation of the transformation are reversible. Press et al. (1997, p. 594) discuss a pyramidal implementation using the DAUB4 wavelet, which I have employed. The DWT tends to capture detail information in the data to a

relatively small number of terms, while noise is spread more diffusely. This is why wavelets are often used for image compression. One gates on the magnitude ($|c_i|$) of the wavelet coefficients, zeroing those below some threshold. Typically, ten times fewer c_i's (than N) can be stored and then used to accurately reconstruct the input waveform via the reverse DWT. This type of compression is discussed more in the next section. In Section 2.4, I discuss how a simple algorithm is constructed to sort through the small number of c_i's surving the DWT in order to detect bursts in noisy time series data.

2.3 Wavelet Denoising

Figure 2-2 displays the light curve for an XRB measured by *HETE* FREGATE. For the 200 bins displayed, the significance of a single-bin 3.3σ ($\approx \sqrt{2 * \log 200}\sigma$) fluctuation is approximately 1σ. The blue curve is the forward then reverse wavelet transform of the data, with a 3.3σ threshold placed on each wavelet coefficient prior to reversing the transform. All terms less significant than this are zeroed, leaving only 5 (2.5% of the total) terms. The reverse DWT then reconstructs the data to better than 10% accuracy using these five terms. Notice that the blue curve in Figure 2-2 approximately describes the data, though the shape of the mother DAUB4 wavelet is residually apparent. As wavelet terms of given scale are only allowed at certain locations in the data array for the DWT, the performance of the forward/reverse transform in reproducing the data depends on the location of the burst. This is potentially unfortunate if one wishes to use a single forward/reverse transformation to looks for features in the data (Section 2.4).

A straight-forward alternative is to apply the forward/reverse wavelet transform to each of the N permutations of the N-bin data array. Threshold at the 1σ level as above after the forward transform. Finally, permute back the N data arrays and average them bin-by-bin. From the blue curve in Figure 2-2, it is clear that this procedure more accurately reproduces the data, with the shape of the mother wavelet apparently washed out. Signal loss is typically at the percent level. This procedure

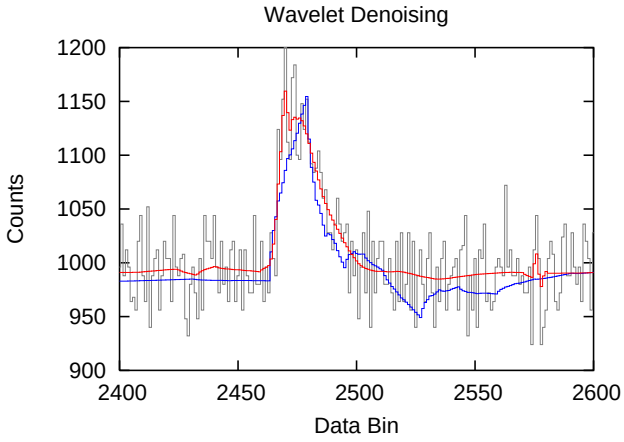

Figure 2-2: A single wavelet transform/threshold/reverse transform operation can denoise a light curve (blue curve), but the shape of the mother wavelet leads to obvious shape artifacts. These can be reduced (red curve) by performing that operation on each of the N permutations of the N-element data array, then averaging the results. The X-axis (time) bins are in units of 0.3 seconds.

is termed "wavelet denoising." Naively, it would require $O(N^2)$ operations, with the single wavelet transform running as $O(N)$. Kolaczyk (1997) discusses speed-up to $O(N \ln(N))$ by exploiting a symmetry in the Haar wavelet transform ("TIPSH denoising"). One can use arbitrary wavelets, with a comparative amount of computation, by employing FFT correlations in the forward transformation, followed by FFT convolutions in the reverse transformation.

2.4 Burst Detection with HETE_WAVE

In the first section of this chapter (Section 2.1), I discussed the relation of a burst's temporal profile to the trigger designed to detect the burst. The optimal trigger, which I will discuss building out of wavelets, will be shaped like the burst. In particular, it will not be sufficient to trigger on the rising edge of a burst, as this procedure can fail if the burst is undersampled or smooth on short timescales. In Section 2.2, I described temporally narrow wavelets, into which a signal can be broken down via the DWT. In this section, I will focus on an algorithm which assembles the wavelet terms from the DWT into burst profiles on-the-fly, determining burst significance and various

statistics describing the burst. The algorithm "hete_wave" is described, in somewhat less detail, in Butler & Doty (2003).

The algorithm has two basic stages: (1) triggering and (2) trigger refinement / parameter estimation. The first stage uses wavelets to find events in the data. This is the novel portion of the algorithm. The second stage employs the first stage output to calculate traditional burst statistics, like the DV or MV discussed in Section 2.1.

2.4.1 Wavelet Triggering

First, the data are passed through a square-root transformation to simplify the statistical interpretation. Transform variable x (binned counts data) to the variable y via:

$$y = \mathrm{Sqrt}(x) \equiv \sqrt{x} + \sqrt{1+x}.$$

This form of the square-root transformation has been found to be stable for low count rates. The inverse transformation is $x = \frac{1}{4}(y - 1/y)^2$. As discussed in Section 2.1, the variable y will be approximately normally distributed with a variance of unity. If the data x are taken from a homogeneous Poisson process (i.e. constant mean), then $< y >= const.$ It will be true that wavelet coefficients $c_i =< \phi_i | y >$ will be approximately normally distributed with mean zero and variance unity. As discussed in Section 2.2, the wavelet coefficients are statistically independent. It is possible to regard linear sums of wavelets as valid wavelets also, in the sense that non-overlapping sets of these sums will be linearly independent. Clearly, a linear sum of wavelets $\psi = \sum_i c_i \phi_i$ will integrate to zero, as each individual wavelet integrates to zero. It is also required that the wavelet be normalized, or $< \psi | \psi >= \sum_i c_i^2 = 1$.

Define a figure of merit:

$$S = \frac{< \psi | y >}{\sqrt{< \psi | \psi >}}.$$

If ψ were generated independently from the data under study, then the composite wavelet coefficient S would share the noise properties of the c_i, and it would be possible to regard S as a measure of signal-to-noise. If ψ is generated using the raw data, then

it will be true that $S = \sqrt{\sum c_i^2}$. If N c_i's are taken to calculate $\sum c_i^2$, then this quantity is approximately χ^2 distributed with N degrees of freedom. The significance in Gaussian σ's can be estimated via the well known formula: $\sigma = \sqrt{2\sum c_i^2} - \sqrt{2N-1}$. The significance σ will be lower (providing less contrast in trigger searches) than would a significance calculated by S. To approximate the conditions needed for S to be a valid measure of significance, the data y are first denoised as discussed in Section 2.3.

So far in Stage 1 of the hete_wave algorithm, the data have been square-root transformed. The data y have been denoised, and the denoised data have been run through the DWT to find the set of c_i's. Finally, the wavelet terms ϕ_i must be grouped, with individual significances $|c_i|$, into composite ψ's for each data trigger. Essentially, this will be done based on proximity in phase space (location, scale). There are many ways to do this, and each would involve constraints which seek to separate "burst-like" composite wavelets from those that are not burst-like in temporal shape. To briefly summarize my implementation, I think of each ϕ_i as a Gaussian with location defined to be the peak of ϕ_i and width defined to be the scale of ϕ_i. (The scale is approximately the width of the positive portion of the ϕ_i.) Ordering the c_i by their magnitudes $|c_i|$ and starting with the largest, temporally overlapping terms are added in. With each addition, the overlap window is calculated and revised. Additions which would push the overlap window to widths broader than a preset value are rejected. This procedure seeks to pack in as many ϕ_i's as possible underneath an excess in the data, ideally forming a ψ shaped as the excess. As discussed in Section 2.1, S would then approach the highest contrast figure of merit.

2.4.2 Refined Triggering and Parameter Estimation

Stage 1 of the hete_wave algorithm finds possible bursts in the data and yields the DMV (Section 2.1) estimates for the burst significances as well as estimates of the burst durations. This also yields a temporal template for the burst in ψ. An example template is shown in Figure 2-3. Primarily because burst statistics traditionally refer to the data in counts space, rather than in the c_i space of the DWT, the counts data

are used to calculate final burst statistics. Also, this stage compensates for signal loss during the denoising in Stage 1, while providing an additional layer of false-detection rejection. Stage 2 of the algorithm is very simple. Significant positive portions of ψ are used to make a quick pass at determining the location of the burst. A linear background estimate is made using data on either side of this window. The burst region is then expanded or contracted to maximize one of the test statistics DV or MV. With the final burst window, the burst peak location and the burst duration are calculated. If desired, a denoised version of the counts data can be used in Stage 2. This provides robustness at the expense of sensitivity loss at the $\lesssim 10\%$ level.

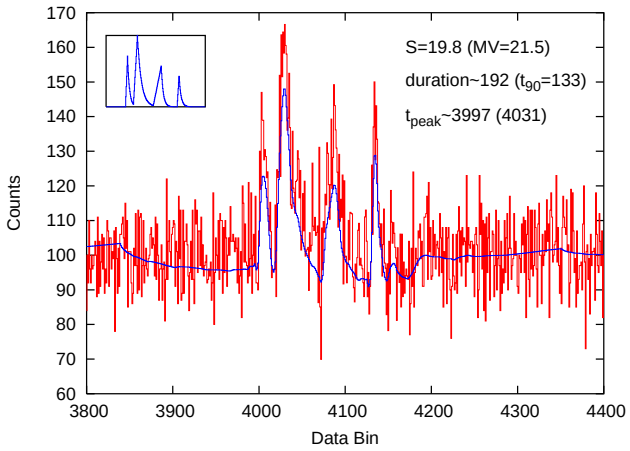

Figure 2-3: A complex burst profile, formed by adding 100 noise counts per bin to the model profile in the figure inset, is detected and reconstructed using wavelets. This yields a temporal model ψ (blue curve) as well as estimates for the significance S, the duration, and the location of the event peak $t_{\rm peak}$. Using the counts data, these are then used to calculate standard burst statistics (quoted in parentheses).

Figure 2-4 shows the stability of the significance calculation (S for Stage 1 and MV for Stage 2) as the data are permuted from left to right. Here S and MV are regarded as indicators of algorithm success and stability. The systematic effects apparent in the S curve are small (<5% level), and these are essentially eliminated in Stage 2. In the next Section, I discuss further tests of the algorithm. In Section 1.4.4, I discuss the success of the hete_wave algorithm in finding near real-time, untriggered bursts for the *HETE* mission.

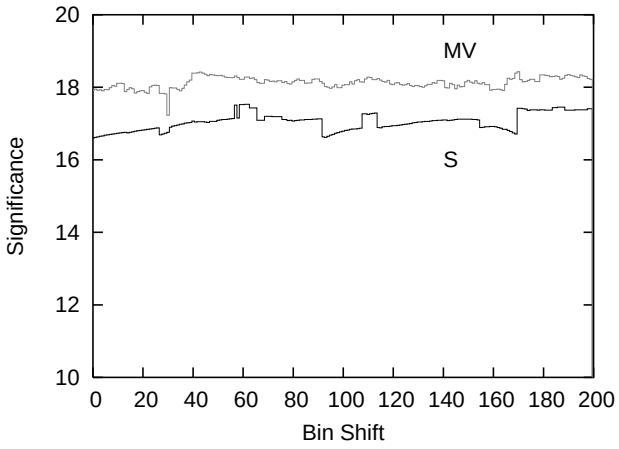

Figure 2-4: The significance for the XRB from Section 2.3 is determined in two stages. In the first stage, the burst is detected and "S" is calculated. In the second stage, the standard model-variance MV is calculated. The robustness for each step can be tested by shifting the data between calls to hete_wave. Calculation of MV helps to remove systematic effect present in the determination of S.

2.5 Monte Carlo Tests of HETE_WAVE

I present here a few simple to tests to gauge the robustness of the hete_wave algorithm. Motivation for developing hete_wave as a supplement to the on-board *HETE* triggers and to other routines run on the ground has been discussed in Section 1.4.2. The actual performance of hete_wave in re-detecting flight GRBs and in supplementing the number of near real-time GRBs detected by *HETE* is discussed in Section 1.4.4. Here I focus on the algorithm's success in detecting simulated bursts with various temporal shapes over noisy, possibly time-varying backgrounds.

Figure 2-5 shows the significance calculation of hete_wave for bursts, of various set brightnesses, simulated from two burst templates. hete_wave has been set to only report the most significant event in the data. The algorithm is loosely constrained to report only events with duration less than 100 bins, whereas the burst templates are 20 bins each. Stage 1 of the algorithm reports only events with $S > 2$, and Stage 2 of the algorithm is set to report only the events from Stage 1 with $MV > 3$. From the plots, it is apparent that hete_wave consistently detects the bursts down to a limiting $MV \sim 4$, while reporting values for MV consistent with the input values. (The

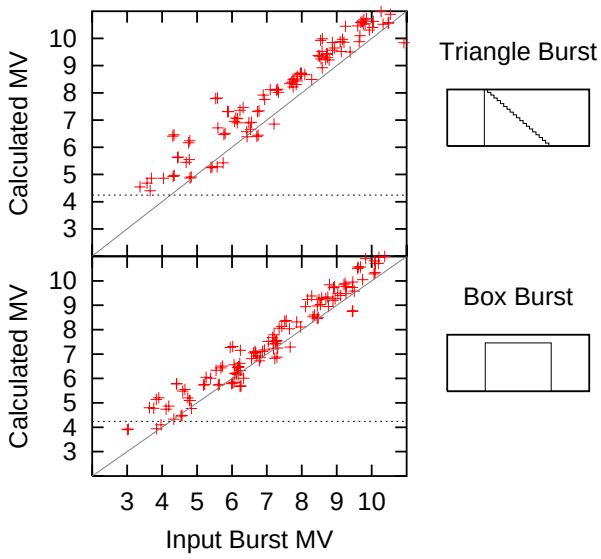

Figure 2-5: Bursts of known MV are simulated using two template temporal profiles. Each template has a duration of 20 data bins, and the background is flat (200 counts per bin). The sum of the background and template is used bin-by-bin as a Poisson mean to noisify the signal, for various burst brightnesses. The uppermost plot shows the performance of hete_wave in detecting a burst shaped like the mother DAUB4 wavelet, while comparable success is apparent for a box-like burst profile. The algorithm fails to detect the burst (in each case) below $MV \sim 4$, which is approximately the Poisson noise floor (dotted curve) for the signal of length 8192 bins.

calculated values are somewhat higher because the Stage 2 algorithm seeks to find the sub-interval which maximized MV.) The data array has a length of 8192 bins; so the Poisson noise floor is at approximately $\sqrt{2 * \log 8192} \approx 4.3$ sigma. The algorithm detects the bursts at approximately 90% efficiency for $MV > 4$, and this efficiency is approximately 100% for $MV > 5$. There appears to be no strong detection preference for one or the other burst profile.

Figure 2-6 shows the trigger efficiency for triangle bursts with $MV \leq 10$ for various event durations. For these data, the calls to hete_wave are the same as above except the maximum allowed event durations varied in proportion to five times the template duration. It is apparent that the efficiency decreases, though only mildly, for increasing event durations. The event detection also appears to become more erratic (see points scatter in Figure 2-6) for longer durations. This can be corrected for by binning up the data prior to searching for very long ($\Delta t \gtrsim 500$ bin events).

Next, the trigger sensitivity is tested against background trends of various sorts. It

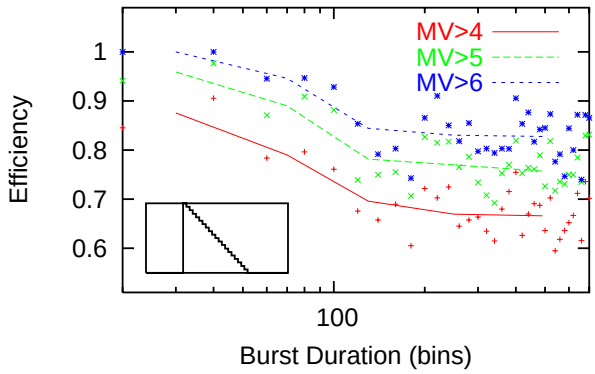

Figure 2-6: Bursts of known MV are simulated using the triangle burst template at various stretchings. The efficiency (fraction of bursts detected) decreases mildly with increasing event duration, especially for low MV events. The solid curves are averages over the points in the plot.

is also demonstrated that the Stage 1 algorithm can reconstruct complex burst profiles in the presence of variable backgrounds. The 185 bin duration, simulated multi-FRED (fast-rise-exponential-decline) burst first shown in Figure 2-3 is used. The complicated structure of this burst could potentially make it difficult to detect above varying backgrounds. In the first test (Figure 2-7, top panel), a uniform background level is slowly increased until the event is no longer detected. This happens consistently below $MV \sim 5$, approximately in agreement with the estimated noise floor. In the second test (Figure 2-7, bottom panel), an extreme background increase (20% over the burst duration) relative to typical rising backgrounds and typical burst durations measured by instruments onboard *HETE* (Section 3.1) is considered. Over a linearly rising background, the burst is easily detected. This is not the case as the background curvature approaches the duration of the burst (rightmost blue points in the bottom panel of Figure 2-7). Stage 2 of the hete_wave algorithm is partially responsible for the failure, because it is currently only capable of fitting a linear model to the background. This can in principle be fixed, though the effect of erroneously large MV's with increasing background curvature will remain due to a more fundamental short-coming in Stage 1. As the mother DAUB4 wavelet used in the algorithm (see Section 2.2) has a non-zero response to signal with curvature, power from the background is increasingly aliased into the burst. If the background is known to vary on short timescales, then

the simple solution is to filter out all but the shortest timescale (temporally finest) wavelet terms during Stage 1 of hete_wave. The green points in the bottom panel of Figure 2-7 demonstrate that hete_wave can effectively trigger on this burst within the strongly time varying background by rejecting all wavelet terms broader than 128 bins. Figure 2-8 shows an example of an XRB trigger on top of an extremely erratic background due to Sco-X1 using this technique.

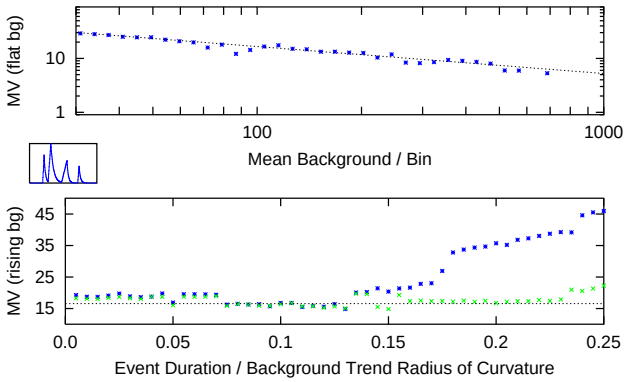

Figure 2-7: Using the inset burst profile, which has a duration of 185 bins, backgrounds of various forms are considered. For a flat background (top panel) the burst is detected accurately until the event MV nears the noise floor. The bottom curve shows the effect of background with curvature. When the curvature is large relative to the burst duration, the algorithm fails (blue points), though this can be corrected for by filtering out all long-duration wavelet components (green points). In each plot, the known MV value is represented by the dotted curve. In the bottom plot, the average background under the burst is approximately 100 counts per bin.

I conclude this section with an estimate of hete_wave's sensitivity based on actual burst detections. During two months in the Summer of 2001, *HETE* was pointed toward the Galactic center and was able to detect numerous XRBs. More than 140 bursts were detected with hete_wave having $MV > 10$. Figure 2-9 shows the cumulative distribution for those and fainter bursts as a function of the significance. During several of the orbits during which XRBs were detected, erratic backgrounds like those in Figure 2-8 were present. Even so, excess noise does not appear to dominate the trigger count until $MV \sim 5 - 6$.

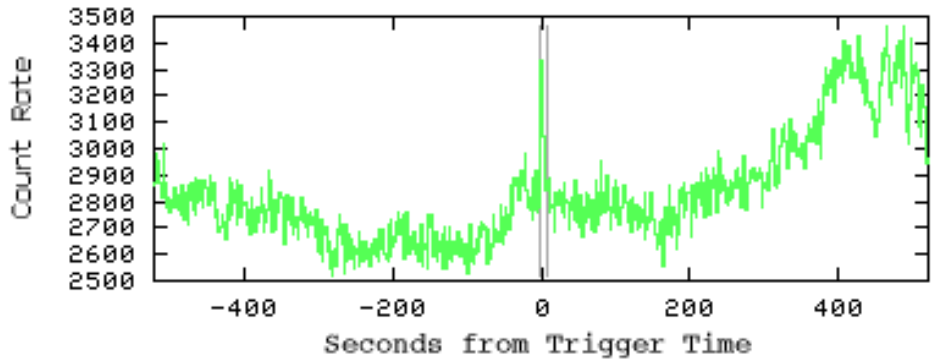

Figure 2-8: Trigger on the "slow burster" (GX 354-00) at 50113 SOD UT on June 6, 2003 ($MV = 15.9$) in the FREGATE 8-85 keV band. Filtering out long-duration wavelet terms allowed for the rejection of unwanted triggers due to the extremely erratic background from Sco-X1.

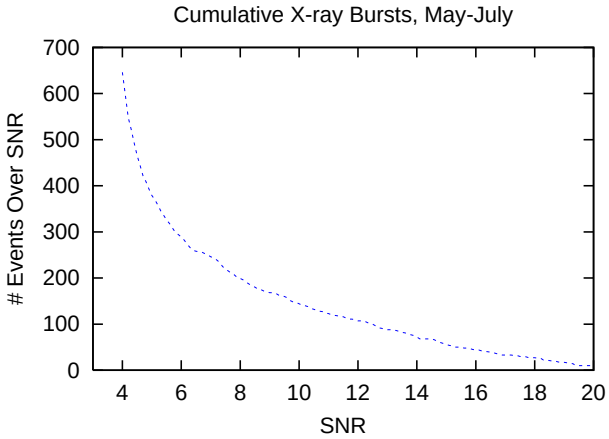

Figure 2-9: The Cumulative distribution of detected X-ray bursts in two months of 2001 in the FREGATE 8-85keV band is plotted versus S/N (MV). It is apparent that hete_wave is affected by excess noise in actual background fluctuations at $MV \approx 5 - 6$.

Chapter 3

Triggering on Very Long-Duration GRBs

3.1 Introduction

As described in Section 1.4.1, the trigger systems on-board *HETE* search over burst durations $\lesssim$ 10s. Longer bursts can be detected if they fluctuate significantly on timescales $\lesssim$ 10s. In Figure 3-1, the distribution of event durations for 265 GRBs detected by the on-board trigger systems is plotted. A possible contribution to the decreasing number of bursts at $t_{50} \gtrsim$ 25s in that plot may be that relatively long duration bursts are missed by the flight trigger systems. This hypothesis is supported by the four (of six) untriggered GRBs relayed to the GCN (Table 1.6, Section 1.4.4) which had $t_{50} \gtrsim$ 25s. It should be noted that the much larger *BATSE* GRB sample (see Figure 1-2) also exhibited a decreasing number of GRBs for $t_{50} \gtrsim$ 20s. To some extent, this may reflect the true source population. However, the *BATSE* triggers (see Section 2.1) only operated on very short timescales ($\lesssim$ 1s), and these triggers would be even more prone than the *HETE* triggers to missing smooth, persistent bursts.

From a theoretical perspective, long duration GRBs should exist. These may actually be GRBs which transition smoothly into their afterglow phase. Or they may be very high redshift ($z > 10$), time-dilated, GRBs. From an observational perspective very long duration GRBs have been detected (e.g. *BATSE* GRB 971208;

Section 2.1). Recently, in't Zand et al. (2003) have discovered four GRBs lasting between 540s and > 2550s in archival data from *BeppoSAX*, and these were found to be fairly typical GRBs.

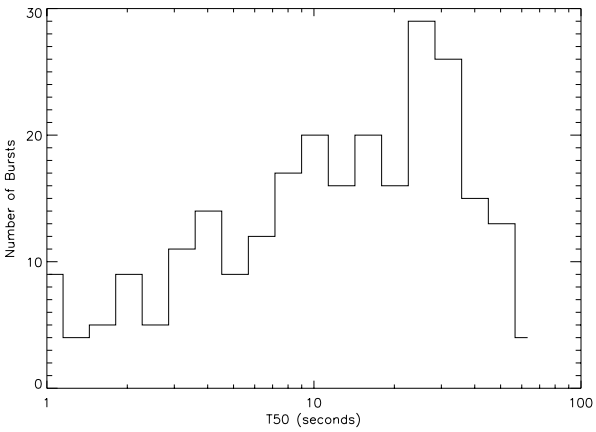

Figure 3-1: The distribution of burst t_{50} durations in the FREGATE 5-40 keV band for 265 flight triggered GRBs. t_{50} is the time over which half of the total burst counts were detected, starting from the onset of the burst. There is a deficiency of events beginning around $t_{50} = 25s$. There are no events with $t_{50} \gtrsim 100s$.

I have worked to increase the sensitivity of the ground triggers to longer duration bursts, in part to look for a previously undetected class of GRBs. I have not yet been successful in this search. Increasing sensitivity to long bursts is also interesting because it helps to improve triggering on typical long/soft GRBs. The more signal captured in a burst detection window, the more likely it is to find a higher S/N (Figure 3-4). In flight, the maximum burst window durations are set by the need to maintain a relatively low false-trigger rate. Long-duration false triggers are overwhelmingly due to rising or falling trends in the *HETE* in-orbit background, though solar activity can occasionally cause more erratic variations.

At X-ray energies ($E < 100$ keV) for WXM and FREGATE, the dominant background arises from the Diffuse X-ray Background (DXRB). At these energies, the DXRB can be modeled by a power-law with photon index $\Gamma = -1.4$. The DXRB background is a non-varying component, except for the case of Earth de-occultation. This de-occultation primarily affects the FREGATE data, creating a rising (falling)

trend at the start (end) of each orbit night. At Gamma-ray energies ($E > 100$ keV), the dominant background is due to the Earth's Gamma-ray albedo, and this is a non-varying background. These steady background components can occasionally be overwhelmed by background variations due to particles trapped in the Earth's magnetic field. *HETE* periodically travels through these overdense regions in its low-Earth, equatorial orbit. Figures 3-2 and 3-3 show the *HETE* in-orbit background count rates due to particles versus Earth latitude, Earth longitude, and altitude of the satellite above the Earth. These plots are described in more detail in Butler et al. 2003. At Gamma-ray energies, the count rate increases are localized within a narrow longitude band (-70 to 0 degrees) corresponding to protons in the SAA, while an overdense (likely lepton-rich) region to the West of the SAA also causes count rate increases typically in the X-ray band. This more Westerly region is also where large increases can occur due to Coronal Mass Ejections (CMEs), though these are rare. The *HETE* flight triggers are often disabled over these regions.

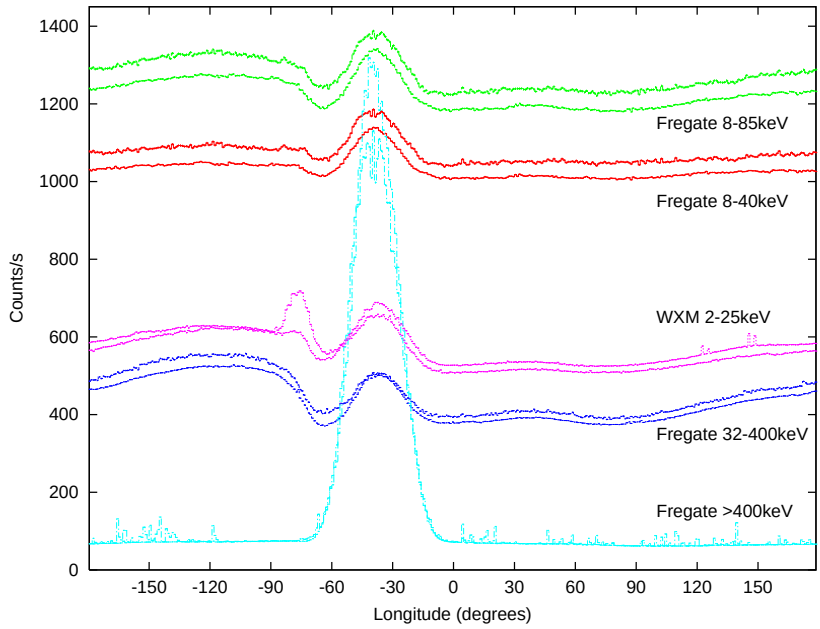

Figure 3-2: Mean instrumental count rates in March (upper curve in each pair) and September of 2001 versus Earth longitude from Butler et al. (2003c). Error bars are plotted. In about 16.1 seconds, *HETE* travels an arc of one degree.

In the sections that follow, I describe three techniques to improve *HETE*'s sensi-

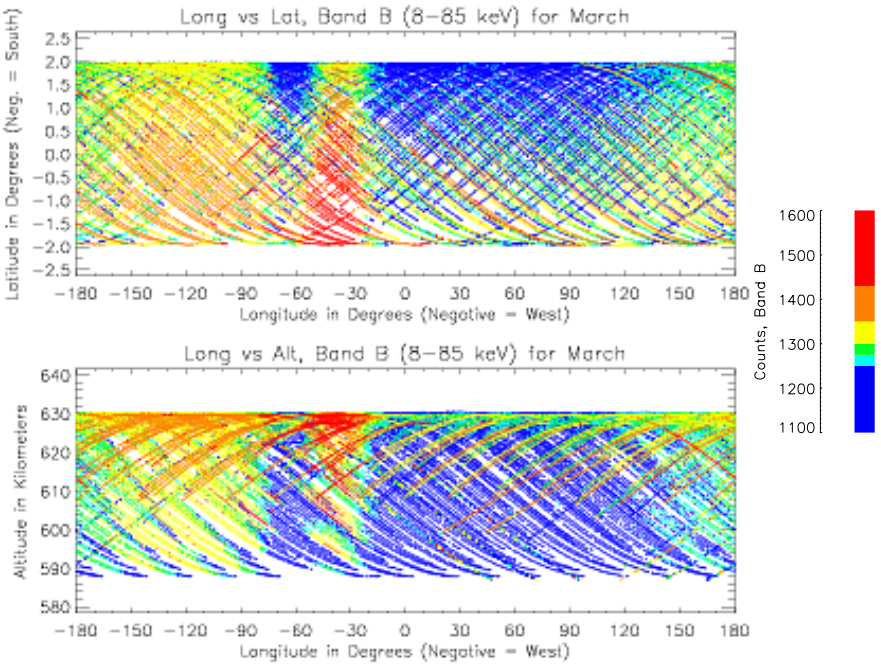

Figure 3-3: Mean instrumental count rates versus latitude (top panel) and altitude (bottom panel) in March 2001 for the FREGATE 8-85 keV band from Butler et al. (2003c). The count rates vary only mildly with these coordinates.

tivity to moderate to long duration bursts. Hypothetical sensitives for each method as a function of burst integration time are shown in Figure 3-4. Extension to longer burst search windows can be viewed as an extension in sensitivity to fainter bursts of a given mean flux. This extension is dependent upon the suppression of typical background fluctuations on long timescale. The first method involves translating the background maps from Figures 3-2 and 3-3 to wavelet space. That yields an average mapping of wavelet coefficients (Section 2.2) to geocentric coordinates, and it allows for the "attenuation" of coefficients likely to be excited by the background, while no attenuation is performed when the background is likely to be smooth. This technique is regularly used in the ground triggering system. The second technique involves searching in image correlation space for the WXM data. Only point sources are expected to produce a strong correlation peak, and background variations can be suppressed. Finally, I review a technique which uses previous orbits to construct count rate templates. This method has not proven successful, and it is likely to be

less effective than correlation map searches.

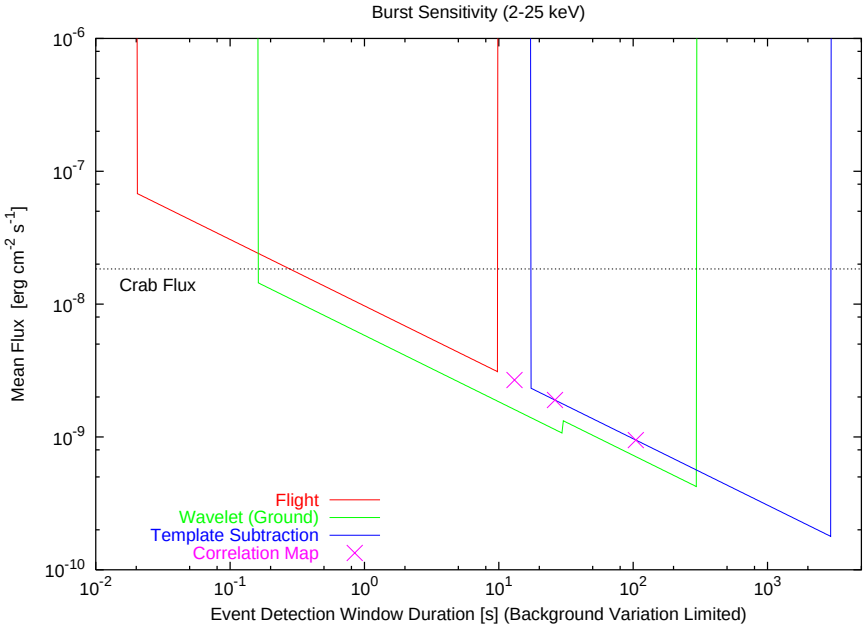

Figure 3-4: The limiting sensitivities for each of the detection methods discussed below is plotted versus detection window duration δt. The hypothetical detection threshold scales as $1/\sqrt{\delta t}$, and it is normalized by the minimal S/N typically necessary for event detection. For the wavelet-based ground triggering with $\delta t \lesssim 30$s, the limiting S/N is approximately 6.0. For the non-wavelet methods, it is approximately 10.0.

3.2 Attenuated Wavelet Coefficients

Wavelet denoising (discussed in Section 2.3) allows one to clean statistically common fluctuations (i.e. noise) out of a data set. In general, an idealized noise model is used. For example, it might be assumed that the noise is Poisson or Gaussian white noise. Alternatively, the essential properties of the noise (i.e. its power on various timescales) can be estimated from the data itself, provided enough data is present so that the noise can be accounted for independent of any possible bursts in the data. A simple recipe for doing this is to pipe a large (say several days worth) of data into a wavelet transform and then to plot the distribution of wavelet coefficients at each scale. For robustness, calculate the median and the median absolute deviation from the median for each set of coefficients, and translate these into Gaussian means μ's

and standard deviations σ's. Assuming the central limit theorem, tail probabilities are easily calculated using $\sigma_N = \sqrt{2 * \log N} * \sigma$ relative to μ. I applied this procedure to 398 orbits of data acquired during September 2001, after rejecting the orbits contaminated by geomagnetic disturbances. This allowed for the construction of tables of 1σ values for wavelet coefficients on scales between 1.2s and 312s, as a function of Earth longitude, Earth latitude, altitude, and orbit phase.

During Stage 1 triggering with hete_wave (Section 2.4), an additional "attenuation phase" is inserted into the burst reconstruction. Here, the wavelet coefficients on each scale are divided by the tabular 1σ values. If the background (here viewed as noise in the frequentist sense) is well behaved enough to follow the central limit theorem, Stage 1 will output true S/N estimates. In general, this will not be crucial, because Stage 2 of the hete_wave algorithm determines event significance. Stage 1 is only used to discover the trigger. This method allows for the burst window to be extended to $\sim$ 300s during orbital periods of typically calm background, while the window is restricted (to $\lesssim$ 30s) where false events due to the background are likely (Figure 3-2).

The attenuated wavelet coefficient method is a regular and essential feature of the ground trigger pipeline. It is run on the 1.2s resolution data from FREGATE and WXM (Table 1.4).

3.3 WXM Correlation Map Searches

In the previous section, I discussed optimization of the wavelet routine hete_wave to operate in orbital regions where false events due to particles are likely or where rising/falling background trends dominate. As suggested by Figure 3-2, about one sixth to one fourth of the data are masked-out in doing this. As *HETE* orbits approximately fourteen times per day, only four to five orbits per day are completely clear of particles regions and sensitively probable for long duration bursts. To get to the rest of the data, one needs a better way of beating down the background. In the next section, I discuss modeling it using previous orbit data. Here, I take advantage of the fact that particles surrounding the spacecraft do not constitute a celestial point

source. They do not result in a correlation peak when the WXM image data are correlated against the WXM mask pattern.

Dr. Garrett Jernigan at Berkeley has implemented a simple correlation map search technique, which I have included in the ground triggering suite of routines. The algorithm runs automatically and has been confirmed to detect flight-triggered GRBs. Dr. Garrett Jernigan's code "wxm-image" facilitated the discovery of *HETE*'s two most recent untriggered bursts (Table 1.6, XRF 030416 and GRB 030226). Figure 3-5 shows how the method catches GRB 030226, while eliminating the particle background.

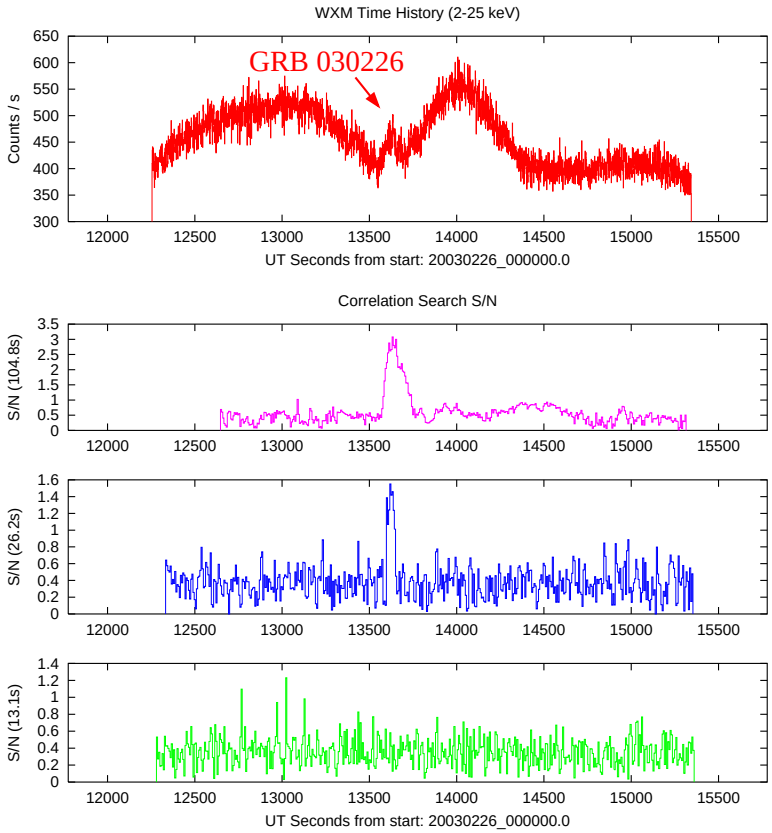

Figure 3-5: Correlations searches can beat down the background and detect a burst where the other methods fail. In the top plot, the WXM 2-25 keV (1.2s resolution) time history is plotted. GRB 030226 is situated near variable background regions due to particles. Flight triggering is thus disabled, and other ground triggering methods are limited. In the bottom three panels, the correlation map S/N is determined at three timescales 13.1s (bottom plot), 26.2s (next from bottom, etc), and 104.8s. The long-duration timescales are most sensitive to the burst, and the particle background is essentially eliminated for all timescales.

The algorithm assumes an idealized WXM mask pattern (essentially a 128 elements vector of one's and zero's), ignoring energy-dependent effects due the finite depth of the detector. The WXM (POS) data for each of the 128 mask elements are summed over energy and detectors (independently for the X and Y direction detectors) at 6.6s resolution (Table 1.4). The data are then correlated with the mask pattern and the value of the highest peak is recorded in addition to the 20th highest peak. The ratio is taken as a signal to noise. These values are summed in time over a preset burst search window, with background taken from before and after the burst window. This method is not sensitive to satellite drift over the duration of the burst window. The current implementation cannot treat multiple bright X-ray sources in the field, though that can, in principle, be changed. Currently, window durations 13.1s, 26.2s, and 104.8s are searched, as displayed in Figure 3-5.

The correlation search described here is a single-orbit differencing method. The requirement that background estimates be made effectively limits the method to events with duration less than half the orbital period (i.e. orbit night). Thus the method is sensitive to bursts with durations $\lesssim$ 1000s.

3.4 Background Template Subtraction

Variations in the *HETE* in-orbit background are largely a function of Earth longitude (Section 3.1). A simple approach which could potentially allow triggering on bursts with duration similar to the orbital period would be to construct template maps of the orbit background versus Earth longitude from previous orbits. Depending upon when those orbits are chosen, it can also be possible to compensate for count rate variations due to Earth latitude and altitude (Section 3.1). Figure 3-6 displays data from the four FREGATE energy bands taken for one orbit. Cleaning and averaging the previous dozen orbits, background templates are generated (dotted curves). It can be seen that these provide a sensible representation of the current orbit's data.

In the Fall of 2002, this technique was implemented in the automated ground trigger searches. It was found to produce too high a false event rate, due to unac-

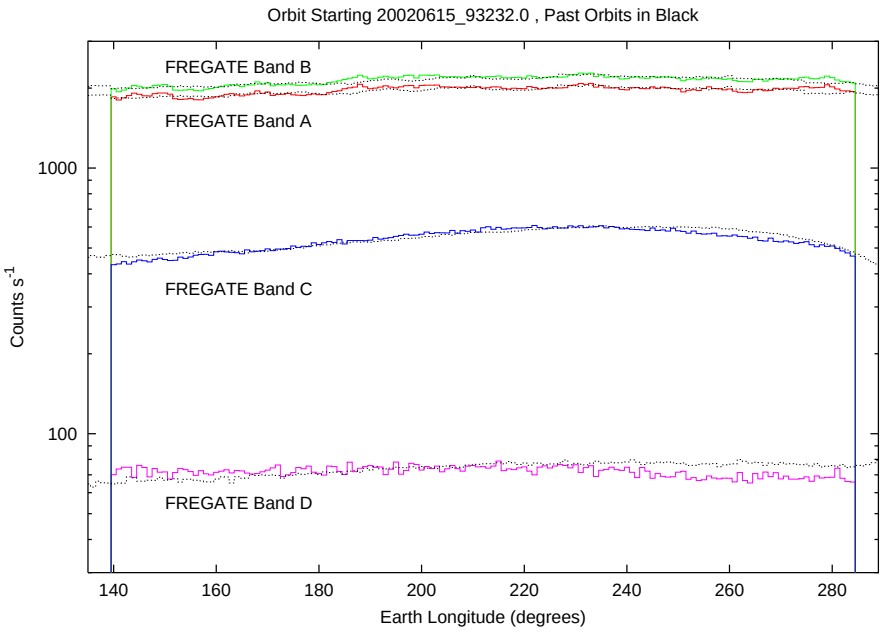

Figure 3-6: Example FREGATE light curves for one orbit in 1 degree longitude (16.1s) bins. Templates created from previous orbits are shown as dotted black lines for each energy band.

counted for variations in the orbit background. Recently, I have tested the method more carefully by selecting 661 orbits over 14 months (∼10% of the data over that period) in 2002 and 2003 for which the background was likely to be well behaved. Primarily, I chose orbits for which the moon was relatively new, for which satellite aspect would likely be stable. I also ignored orbits known to be contaminated by solar activity. Searching over 500s burst windows in the 30-400 keV band, I found 300 events more significant than 10σ. Upon closer inspection, each of these events appear to be due to background fluctuations. This was concluded because the time history data in the vicinity of each candidate burst appeared to be smooth (in a manner consistent with typical background variations) rather than burst-like. Hence, I again found that the method was too sensitive to unaccounted for background variations. Template data from one day prior to each test orbit have been considered in order to minimize variations due to satellite latitude and altitude, and this has not helped. The background template subtraction method is still very much under development, and it may (in spite of the negative results to date) provide a means of triggering

on very high S/N ($\gtrsim 30$) bursts which would previously have been ignored. These burst would currently be ignored by the flight and ground trigger systems if the event durations were very long or if the events occured over the SAA.

This method provides a check on bursts detected via methods discussed in the other sections. It is likely that a multi-orbit image correlation technique will need to be employed to look for bursts on orbital period or longer timescales. Such a method, involving iterative cleansing of known sources, was used by in't Zand et al. (2003) to find the very long duration bursts in archival searches of *BeppoSAX* data.

Chapter 4

Afterglow Imaging Observations with Chandra

4.1 GRB 020531: Observations

To date, there have been no credible detections of a fading X-ray, optical, IR, radio, etc. counterpart to a short/hard GRB (see Figure 1-2) (see, e.g. Kouveliotou et al., 1993; Hurley et al., 2002). The most rapid prompt localization of a short/hard GRB came with the *HETE* detection of GRB 020531, reported over the GCN ∼88 min after the GRB (Ricker et al., 2002a). With a t_{50} duration of roughly 360ms, this was clearly a member of the short/hard class of GRBs (Figure 4-1). The prompt emission characteristics are described more in Lamb et al. (2002). The initial *HETE* error region was refined by the IPN at 18 hours (Hurley et al., 2002a), refined again at 5 days ("IPN Region I") (Hurley et al., 2002b), and refined again at 56 days ("IPN Region II") (Hurley et al., 2002c) after the GRB. Early observations in the optical did not securely detect a counterpart source, though a number of interesting potential candidates were observed (see, e.g., Boer et al., 2002,a).

We began a first epoch (E1) observation with *Chandra* 5.15 days after the GRB. This was a 20 ksec observation placing IPN Region I at the center of the ACIS-I array (Butler et al., 2002a). A second epoch (E2) observation of the same region began 10.86 days after the GRB and lasted for 10 ksec (Butler et al., 2002b). Our

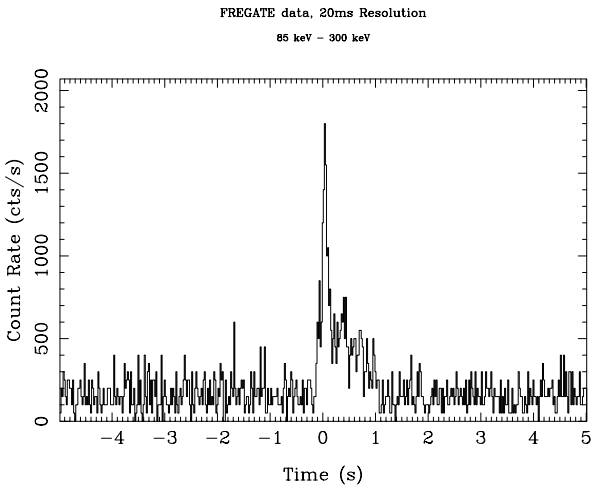

Figure 4-1: In the FREGATE Gamma-ray band (85-300 keV), GRB 020531 has a t_{50} duration of approximately 360ms, making it a clear member of the short/hard class of GRBs.

observations in the optical are described in Dullighan et al. (2003).

4.1.1 GRB 020531: Chandra E1 Sources

As reported in Butler et al. (2002a), 10 candidate sources were discovered within IPN Region I in the 0.5-8 keV band (Table 4.1). The ACIS-I data are shown in Figure 4-2. The three brightest sources on the ACIS-I array were outside of IPN region I. Conspicuous optical counterparts to these three sources were observed (Butler et al., 2002a). Further observations of these 13 sources in the optical (see, e.g., Miceli et al., 2002) and in the radio (Frail & Berger, 2002) failed to implicate any source as the GRB afterglow.

Taking 5 counts as an approximate smallest number of detected counts for a useful E1 source, we estimate a flux limit for this observation of 2×10^{-15} erg cm^{-2} s^{-1}. This assumes the Galactic column density ($N_H \approx 8 \times 10^{20}$ cm^{-2}) and a power-law source spectrum with photon index 1.9, typical for GRB X-ray afterglows (Costa et al., 1999).

The brightest source observed in E1 (Source 0) lies just beyond IPN Region I, but inside the more recent IPN Region II. The source flux is approximately 2.1×10^{-14} erg cm^{-2} s^{-1}. In comparison with sources detected in the Chandra Deep Field South

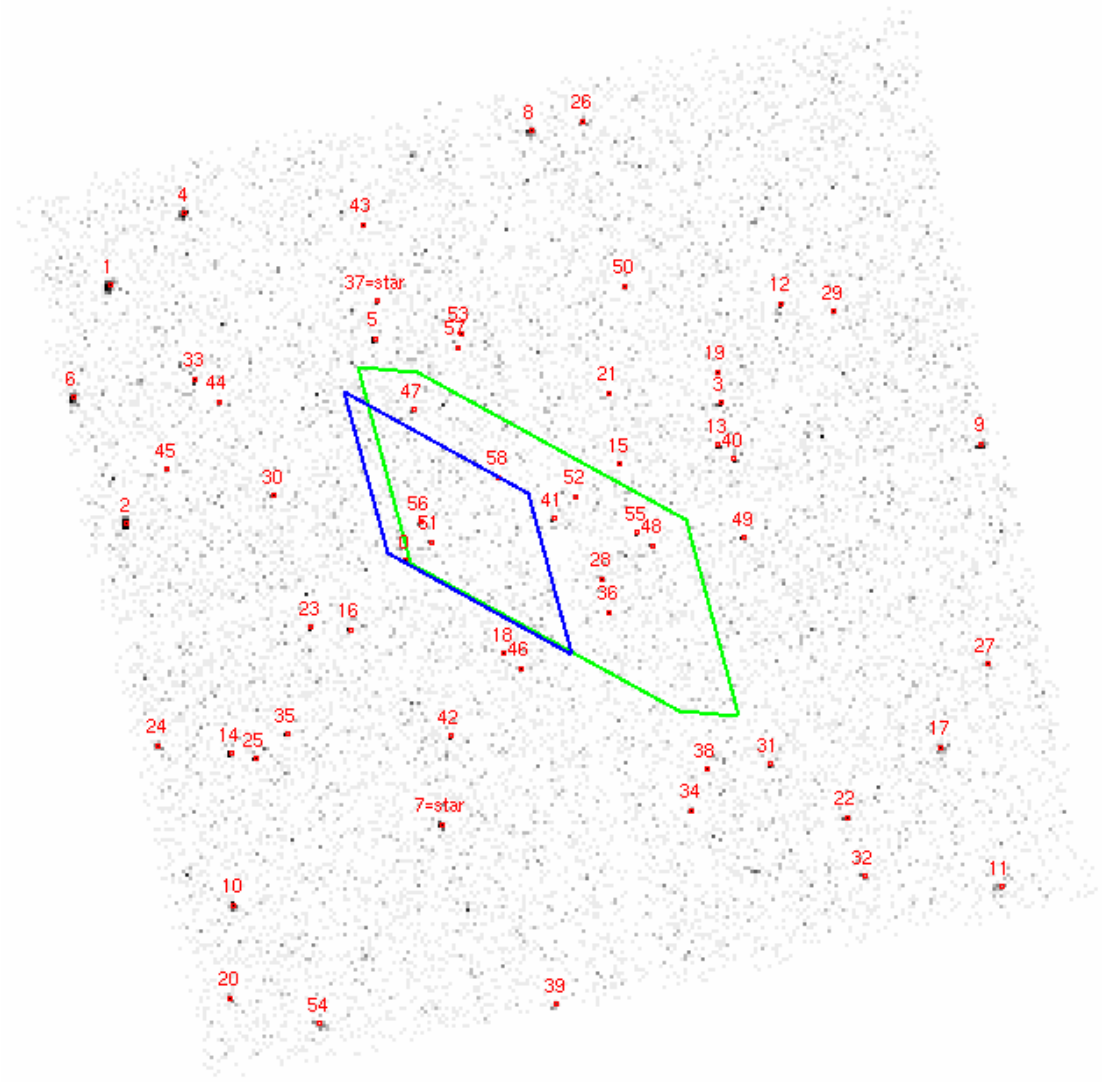

Figure 4-2: The *Chandra* ACIS-I array (18′ by 18′ field-of-view) encloses IPN Regions I and II (outer and inner polygons, respectively). Point sources found by running wavdetect (Freeman et al., 2002) are shown and indexed according to brightness.

(CDFS) (Rosati et al., 2002), the odds of finding a source of equal or higher flux is approximately 1 in 3 for a 9 square arcminute region (size of IPN Region II). The hardness-ratio of the object is similar to that of AGN discovered in the CDFS, and our optical observations indicate that Source 0 is likely a quasar at $z = 0.73$ (Dullighan et al., 2003). Based on their E1 fluxes alone, none of the other sources are unusual objects relative to the CDFS.

4.1.2 GRB 020531: Chandra E2 Sources

Table 4.1 shows the number of counts detected in E1, along with the 90% confidence interval for E2 based on the E1 values. We have used a circular extraction region for each source, with radius set to 2 times the 95% encircled energy radius r. This varies over the chip and is approximated via $r = 2.05 - 0.55 * d + 0.18 * d^2$ arcsec, with d measured in arcminutes from the center of the ACIS-I array. We use an annular background region ten times larger than the signal region, centered on and surrounding the signal region. The exposure is calculated separately for each source extraction region in each epoch. Five sources (0,5,48,56,52) were observed in E2 with a detected number of counts below the 90% confidence lower bound established in E1. We ignore Source 52 because of the very small number of detected counts.

GRB X-ray afterglows typically fade in brightness with time as $t^{-1.3}$, with t measured from the GRB (Costa et al., 1999). Assuming no spectral evolution, this implies a count-rate fade factor of approximately 2.5 between E1 and E2. We can test whether the data for each source prefers a fade versus a constant count rate by fitting the data for each source first with a single-rate model (Model A), then fitting the data with a model allowing the E2 rate to be lower than the E1 rate (Model B). We do the fits by maximizing the logarithm of the Poisson likelihood (i.e. the Cash (1979) statistic C). We then simulate 10^4 data sets for each source using the count rate determined from Model A, and we count the number of these which yield a larger ΔC than the observed value when fit with Model B. These fractions are expressed as probabilities (P_C) in Table 4.1. The most significant source is Source 48, where $P_C \approx 0.8\%$. Considering that approximately ten trials were performed in order to find this fade, the

effective value for chance fade is more like 8%. The fade in this source is greater than the factor 2.5 fade expected for a GRB afterglow; so the source appears interesting. Kulkarni et al. (2002) took a spectrum of the host galaxy observed in the optical near Source 48 (Fox et al., 2002a) and found it to lie at a redshift $z \approx 1$. Unfortunately, Source 48 lies outside of IPN Region II. Of the five fading sources, only Sources 0 and 56 lie within IPN Region II. As discussed above, Source 0 is likely a quasar. Given ten trials to find it, the chance fade probability in Source 56 is unreasonably large ($\sim 60\%$). Moreover, there is no evidence in our observations with Magellan and Subaru (Dullighan et al., 2003) that this source faded in the optical.

		Epoch 1		Epoch 2		
#	Chandra Name	Net (Bg)	$E2_{90\%}$	Net (Bg)	ΔC	$P_C^{(\%)}$
28	CXOU J151459.7-192532	13.0 (1.0)	3.9,10.2	6.6 (0.4)	0.00	42.7
36	CXOU J151459.2-192609	11.5 (0.5)	3.4,9.2	3.6 (0.4)	0.27	21.5
48	CXOU J151455.8-192454	7.3 (0.7)	1.7,6.6	-0.2 (0.2)	2.92	0.8
41	CXOU J151503.6-192423	7.1 (0.9)	1.7,6.5	3.6 (0.4)	0.00	46.9
56	CXOU J151514.1-192428	6.6 (0.4)	1.6,6.1	0.7 (0.3)	1.00	8.8
51	CXOU J151513.3-192450	6.5 (0.5)	1.5,6.0	6.6 (0.4)	0.00	46.0
47	CXOU J151514.7-192221	6.2 (1.8)	1.2,6.1	2.9 (1.1)	0.00	46.5
58	CXOU J151508.0-192338	5.6 (0.4)	1.2,5.4	1.9 (0.1)	0.09	32.7
55	CXOU J151457.0-192439	4.9 (0.1)	1.3,6.1	7.9 (0.1)	0.00	45.6
52	CXOU J151501.9-192358	4.4 (0.6)	0.8,4.6	0.7 (0.3)	0.40	19.5
...						
0	CXOU J151515.3-192511	69.5 (1.5)	28.8,42.9	21.8 (0.2)	1.74	2.8
5	CXOU J151517.8-192102	43.6 (3.4)	16.9,28.4	15.2 (1.8)	0.59	11.1
15	CXOU J151458.3-192322	19.4 (0.6)	6.5,14.1	7.6 (0.4)	0.11	29.6

Table 4.1: Ten point sources are detected between 0.5 and 8.0 keV in the *Chandra* E1 observation lying within IPN Region I. The three brightest *Chandra* sources (0,5,15) are not within this region. Source 0 is, however, within IPN Region II. From the E1 net counts, we calculate $E2_{90\%}$, the 90% confidence region for the expected net counts in E2, following Kraft et al. (1999). The columns labeled "ΔC" and "P_C" are explained in Section 4.1.2. Small values of P_C indicate sources likely to have faded between E1 and E2.

4.1.3 GRB 020531: Discussion and Conclusions

In two imaging observations with *Chandra*, five candidate X-ray counterparts to the short/hard GRB 020531 were discovered based on their fade properties. Two of

these (Sources 48 and 5) were observed with *Hubble STIS* and found to be extended (Dullighan et al., 2003), though we learned later that both were outside of IPN Region II. Neither is thus likely to be associated with the GRB. Source 0 is likely to be an unrelated field object (a quasar). Source 56 exhibited no fade in the optical. Source 52 was deemed too faint to be judged. Further observations with *Chandra* will be necessary to rule decisively on these last two candidates. Most likely, however, none of these sources are counterpart to GRB 020531.

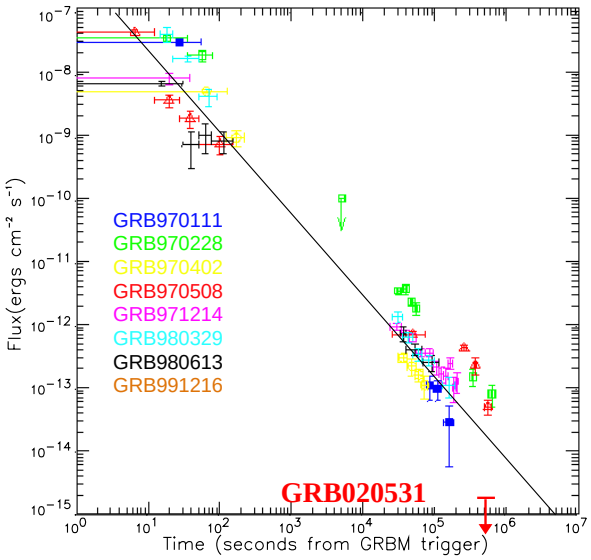

Figure 4-3: In comparison with eight GRB X-ray afterglows measured by *BeppoSAX* (Figure adapted from Costa et al. (1999)), the E1 flux for GRB 020531 (marked with a red "X") is an order of magnitude lower than what is typical for long/soft GRBs.

Given the sensitivity of our E1 observation, the X-ray source flux must have been lower than approximately 2×10^{-15} erg cm^{-2} s^{-1} five days after the GRB. This is an order of magnitude fainter than what is typical for long duration GRBs (Figure 4-3) (Costa et al., 1999), though a rapid fade may be expected for short/hard GRBs given their possible association with compact object mergers (see, e.g., Eichler et al., 1989). One source was reported in the optical $\sim$ 2hrs after the GRB ("TAROT C") (Boer et al., 2002a). From a deep observation with Magellan 1.14 days after the GRB (Dullighan et al., 2003), the source must have faded faster than $t^{-2.1}$, were it to be

the optical transient associated with the GRB. This is rapid, but perhaps not unreasonable for a short/hard GRB. In order to catch the afterglow of a future short/hard GRB, it will be critical to have earlier (< 5 day) X-ray followup observations.

4.2 GRB 030528: Observations

The X-ray-rich (i.e. for the fluence S, $\log[S_X(2-30 \text{ kev})/S_\gamma(30-400 \text{ kev})] > -0.5$) GRB 030528 was detected by the *HETE* satellite (Atteia et al., 2003a) with a $2'$ radius (90% confidence) SXC localization. The Gamma-ray light curve is shown in Figure 4-4. The initial SXC error region was later revised (Villasenor et al., 2003b) after the discovery of an unaccounted-for systematic effect, resulting in a shift in position center and an expansion of the error region to $2.5'$ radius. Early R-band observations reaching $R \approx 18.7$ roughly 140 minutes after the burst (Ayani & Yamaoka, 2003) and unfiltered observations reaching 20.5 magnitude roughly 14 hours after the burst (Valenti et al., 2003) failed to detect a counterpart. Excitement in this optically dark burst was also generated within the *HETE* team as one of our Japanese colleagues reported a possible indication of extremely high N_H in the WXM spectral fits (Sakamoto, 2003). This suggested that the burst might have been situated in an extremely dense or cosmologically distant region.

On 3 June, the *Chandra* Observatory targeted the field of GRB 030528 for a 25 ksec ToO observation (E1) lasting between 5.97 and 6.29 days after the burst. The revised SXC error region was completely contained within the field-of-view of the *Chandra* ACIS-S3 CCD chip. A second observation (E2) was then conducted lasting 20 ksec and ranging from 11.8 to 12.1 days after the burst. With the increased low-energy spectral response of ACIS-S3 (relative to the front-sided ACIS chips), we hoped to measure excess absorption in the afterglow, in addition to detecting and finely localizing the afterglow.

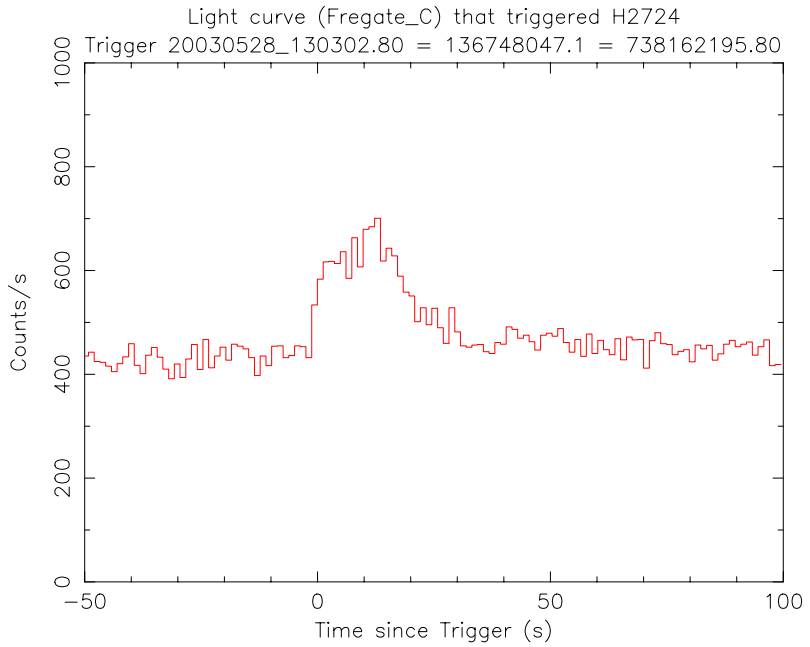

Figure 4-4: Light curve for GRB 030528 in the FREGATE Gamma-ray band (30-400 keV).

4.2.1 GRB 030528: Chandra E1 Sources

As reported in Butler et al. (2003d), 4 candidate sources were detected within the revised SXC error region. Seven additional non-stellar point sources were detected within the entire ACIS-S3 field-of-view (Figure 4-5). Positions and other data for these sources are shown in Table 4.2. None of the sources were anomalously bright relative to objects in *Chandra* deep field observations (see Section 4.1.1). We had performed deep observations with Magellan prior to the *Chandra* observation, but none of the *Chandra* sources were in our field of view. However, IR observations of a portion of the SXC error containing two of the E1 *Chandra* sources revealed a fade in I-band of 0.9 magnitudes in the brightest source (#1) within the revised SXC error region (Greiner et al., 2003). Deep observations in the radio (Frail & Berger, 2003) and in the optical (Mirabel & Halpern, 2003) failed to detect this source after the *Chandra* observation.

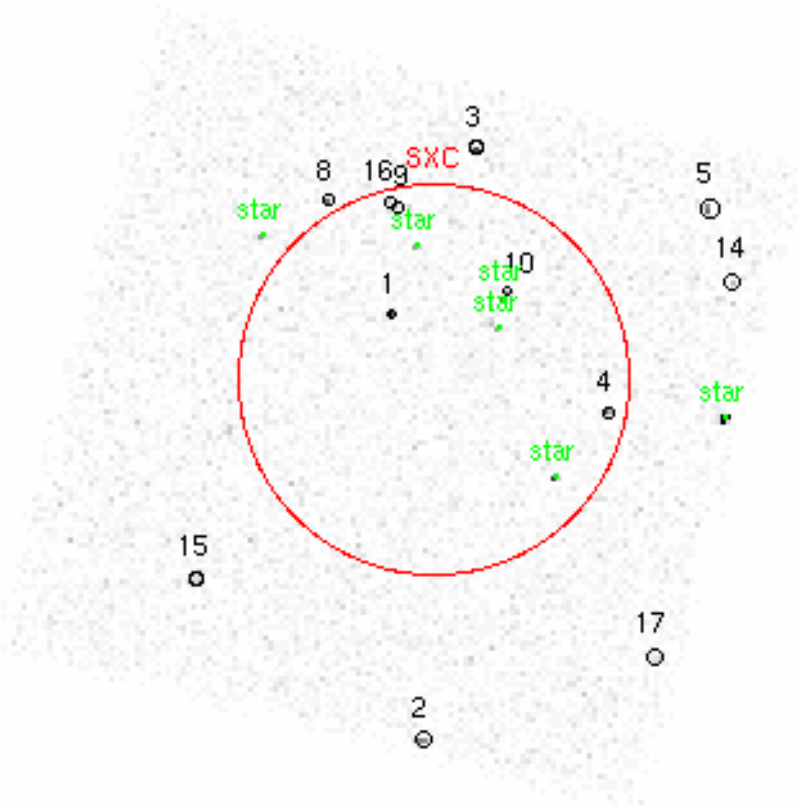

Figure 4-5: The *Chandra* ACIS-S array (9′ by 9′ field-of-view) encloses revised SXC error region (circle). Six field stars were used to register the astrometry according to the positions reported by Henden (2003).

4.2.2 GRB 030528: Chandra E2 Sources

Table 4.2 shows the number of counts detected in E1, along with the 90% confidence interval for E2 based on the E1 values. The E2 observations were reported in Butler et al. (2003e). We have used source and background extraction regions as described in Section 4.1.2. Of the four sources in the revised SXC error region (#'s 1,4,9,10), only source #1 has faded below the 90% confidence range established in E1. The significance of the fade is approximately 3σ, and we estimate the temporal index (assuming a power-law fade) to be $\alpha = 2.0 \pm 0.8$. This is somewhat steeper than the typical $t^{-1.3}$ fade for X-ray afterglows (Costa et al., 1999), though it is characteristic of afterglows which have undergone a so-called "jet-break" (Frail et al., 2001). None of the other *Chandra* sources were observed to fade at a high level of significance, and source #1 (also a fading IR source as discussed above) is extremely likely to be counterpart to GRB 030528.

		Epoch 1		Epoch 2		
#	Chandra Name	Net (Bg)	$E2_{90\%}$	Net (Bg)	ΔC	$P_C^{(\%)}$
1	CXOU J170400.3-223710	39.5 (1.5)	24.1,41.1	8.5 (2.5)	6.97	0.01
4	CXOU J170348.4-223826	30.1 (2.9)	16.4,30.2	20.3 (2.7)	0.01	37.7
9	CXOU J170400.1-223548	10.8 (2.2)	4.1,12.6	5.4 (3.6)	0.17	28.8
10	CXOU J170354.0-223654	9.2 (2.8)	3.4,12.6	8.3 (2.7)	0.00	44.7
...						
2	CXOU J170358.7-224237	30.6 (3.4)	14.1,28.0	23.9 (2.1)	0.00	36.1
3	CXOU J170355.7-223503	23.1 (2.9)	11.8,24.6	15.1 (3.9)	0.03	2.3
5	CXOU J170342.8-223548	23.7 (4.3)	12.4,26.0	10.7 (6.3)	0.85	9.8
8	CXOU J170403.9-223543	12.7 (2.3)	5.7,16.0	4.4 (2.6)	0.94	8.9
14	CXOU J170341.4-223646	6.1 (4.9)	1.1,9.0	9.7 (5.3)	0.00	48.8
15	CXOU J170411.2-224032	11.0 (4.0)	4.3,14.4	5.5 (3.5)	0.20	24.1
17	CXOU J170345.8-224133	10.5 (4.5)	1.1,4.0	...		

Table 4.2: Four point sources are detected in the 0.5-8.0 keV band in the *Chandra* E1 observation lying within the revised SXC error region. Eight additional, non-stellar point sources are detected in the ACIS-S3 field-of-view. From the E1 net counts, we calculate $E2_{90\%}$, the 90% confidence region for the expected net counts in E2, following Kraft et al. (1999). The columns labeled "ΔC" and "P_C" are explained in Section 4.1.2. Small values of P_C indicate sources likely to have faded between E1 and E2. Source #17 was situated on a chip gap in E2.

4.2.3 GRB 030528: Discussion and Conclusions

As was not the case for GRB 020531 (Section 4.1), an X-ray observation ∼5 days after GRB 030528 detected the burst at a flux level (1.4×10^{-14} erg cm^{-2} s^{-1}) typical for GRB X-ray afterglows (Figure 4-3 and Costa et al. (1999)). Here we have assumed a typical power-law spectrum for X-ray afterglows as in Section 4.1.1 and the Galactic $N_H = 1.6 \times 10^{21}$ cm^{-2}. A second epoch observations decisively revealed that source #1 had faded, establishing securely that this was the counterpart X-ray afterglow to GRB 30528.

The prompt GRB X-ray spectrum in the WXM is well fit ($\chi^2_\nu = 16.93/26$) by an absorbed power law with photon index $\Gamma = 1.8 \pm 0.3$ and $N_H = 5^{+4}_{-3} \times 10^{22}$ cm^{-2}, both at 90% confidence. The required N_H is greater than the Galactic value at 3.4σ confidence ($\Delta\chi^2$ =11.29 for 1 degree of freedom). Though there are not enough source counts for spectral fitting with the *Chandra* data, consideration of the source hardness does not suggest excess low-energy absorption. Assuming typical

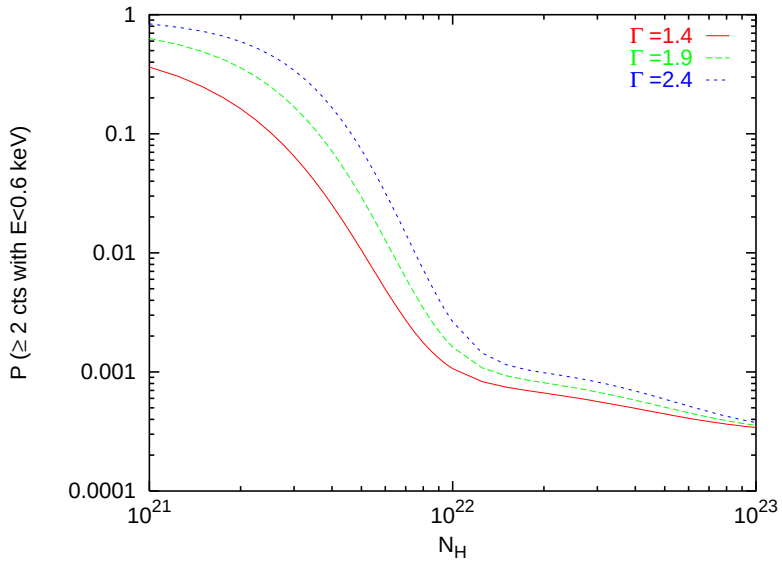

Figure 4-6: The probability is very low that a power-law spectrum with the indeces shown and $N_H \gtrsim 10^{22}$ cm^{-2} could have yielded two source counts below 0.6 keV, as observed. The possibility that the counts could have come from the background is accounted for, using an annular background region approximately 100 times larger than the source region and surrounding the source region. The expected number of background counts in the 3.3″radius source extraction region is 0.02 counts.

burst spectral parameters as in the preceding paragraph and the Galactic N_H, we can calculate the ratio HR of the expected counts flux in the 0.2-2.0 keV band to the expected counts flux in the 2.0-8.0 keV band. This should be approximately 3.5. For a twelve times larger N_H, consistent with the 90% confidence lower limit determined from the prompt emission, this hardness ratio drops to approximately 0.5. For source #1, we find $HR = 4.5 \pm 2.0$. For this hardness ratio to be consistent with the N_H inferred from the prompt emission, the afterglow would need to be fit by a power-law with the unreasonably large $\Gamma = 4.3$. This conclusion can also be drawn from the mere presence of two source counts detected below 0.6 keV (Figure 4-6). Hence, there is considerable flux below 2.0 keV, and no evidence from the X-ray afterglow data for excess absorption as seen in the prompt GRB emission.

It is likely that the explanation for the optical darkness of GRB 030528 has to do with an intrinsic faintness of the optical afterglow. Indeed, *HETE* appears to be solving the problem of optically dark bursts by showing that, given a fine enough

localization (i.e. $\lesssim 5'$ error radius), optical or IR transient are consistently detected. As shown in Table 1.7, optical (or IR) transients were detected for eight out of nine bursts with fine (SXC) localizations. Optical darkness appears to be a selection effect which arose historically due to the difficulty of performing deep observations (with large telescope with small fields of view) of large GRB error regions. Interestingly, *HETE* is showing that there appears to be instead an "optically faint" class of GRB afterglows. Further observations will be necessary to explore the properties of GRB 030528 and its host environment. These may help determine why many GRBs are optically faint.

Chapter 5

Afterglow Spectroscopic Observations with Chandra

5.1 Summary

As mentioned in Section 1.2.2, we find possible evidence for Si and S emission in a *Chandra* HETGS spectrum of the GRB 020813 afterglow. We detect a Ni-K line at very low significance, and we find a strikingly low upper limit to the Fe-K line equivalent width. The emitting material is blue-shifted with velocity $\sim 0.1c$ relative to the GRB host galaxy. These results add weight to the detections claimed by Reeves et al. (2002) and Watson et al. (2002). With the HETGS's high spectral resolution, we are able to resolve the line widths, and we are able to accurately separate the line and continuum emission. Because the lines we associate with S and Si are detected in the full data set, we have ~ 5 times more counts to work with than Reeves et al. (2002), where the line emission is observed during only a short period of time. Moreover, the continuum is an order of magnitude stronger than that reported by Reeves et al. (2002), possibly indicating, in the case of thermal emission, that a power-law component is also present. This may alternatively be a sign that the lines are produced under reflection.

5.2 Observations

Using Directors Discretionary Time, two afterglows of GRBs detected and localized by *HETE* were observed with the *Chandra* HETGS, approximately 1 day after each burst, and lasting for approximately 1 day. Both bursts were long-duration GRBs, with Gamma-ray durations $\gtrsim$100s. The Gamma-ray peak flux from GRB 020813 (Villasenor et al., 2002) was quite high ($\sim 10^{-5}$ erg cm^{-2} s^{-1}), while the peak flux from GRB 021004 (Shirasaki et al., 2002) was approximately two orders of magnitude lower. Gamma-ray light curves for each burst are shown in Figures 5-1 and 5-2.

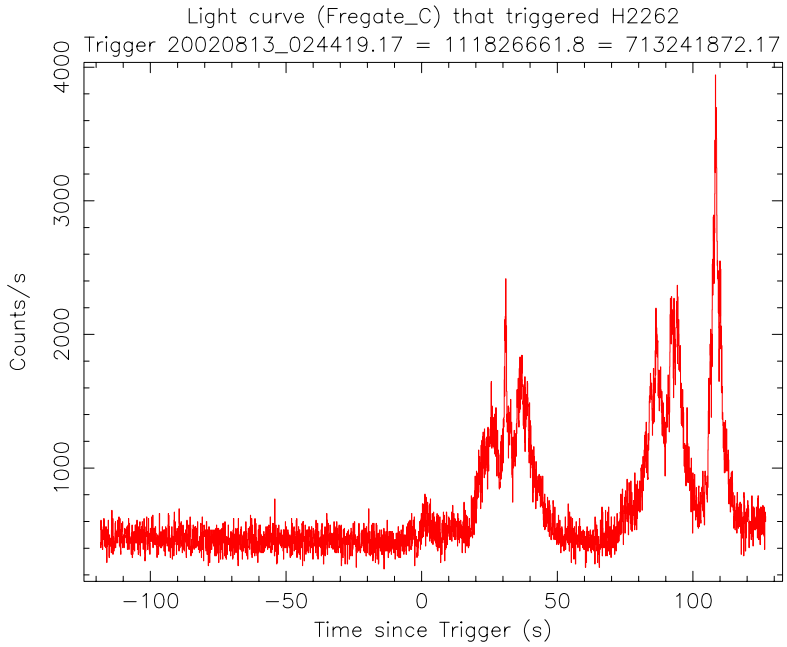

Figure 5-1: FREGATE light curve in the 30-400 keV band for GRB 020813.

Chandra began observing the GRB 020813 afterglow with the HETGS on August 13.990 (t_{burst} + 21.02 hrs) and continued until August 14.892 (t_{burst} + 42.67 hrs), with a total livetime of 76.8 ksec. The mean count rate from the High Energy Gratings (HEG) and Medium Energy Gratings (MEG) and the 0th order image was 0.12 counts/s (0.06 counts/s for the gratings alone). The afterglow candidate reported by Fox (2002) was detected and was observed to fade in brightness with time according to a power-law of index $\alpha = -1.38 \pm 0.06$ ($\chi^2_\nu = 36.4/24$) (Figure 5-3), consistent with the value reported by Vanderspek et al. (2002) and consistent with measured

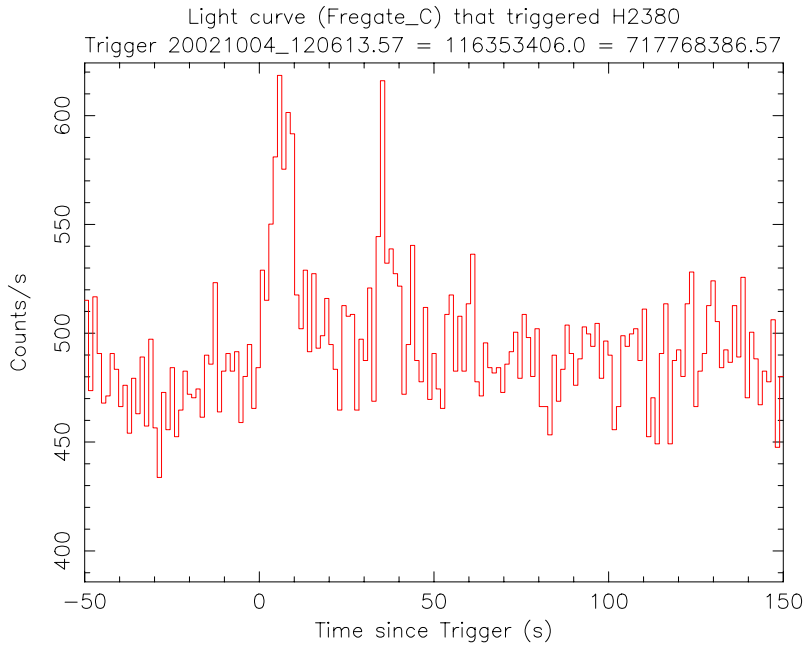

Figure 5-2: FREGATE light curve in the 30-400 keV band for GRB 021004.

values in the optical (Malesani et al., 2002). Between 0.6 and 6 keV, we measure a time-averaged flux of 2.2×10^{-12} erg cm^{-2} s^{-1}.

As first reported by Sako & Harrison (2002), *Chandra* began observing the afterglow of GRB 021004 on October 5.358 (t_{burst} + 20.49 hrs) and continued until October 6.400 (t_{burst} + 45.50 hrs), with a total livetime of 86.7 ksec. The mean count rate from the HEG and MEG gratings and the 0th order image was 0.04 counts/s (0.02 counts/s in the gratings alone). The afterglow candidate reported by Fox (2002a) was detected and was observed to fade in brightness with time. The X-ray light curve appears variable. (Similar variability has been reported in the optical for this afterglow; see e.g. Halpern et al. (2002)). The temporal fade in flux can be described by a power-law with index $\alpha = -0.9 \pm 0.1$ ($\chi^2_\nu = 83.8/27$) (Figure 5-3), consistent with the values reported by Sako & Harrison (2002) and Holland et al. (2002). The time-averaged flux between 0.6 and 6 keV is measured to be 6.3×10^{-13} erg cm^{-2} s^{-1}.

The total number of counts detected by *Chandra* in the case of GRB 020813 (GRB 021004) is $\sim$ 9 times (3 times) the number of counts detected for GRB 991216 (Piro et al., 2000) (see Table 6.1). We perform a parallel spectral/temporal analysis

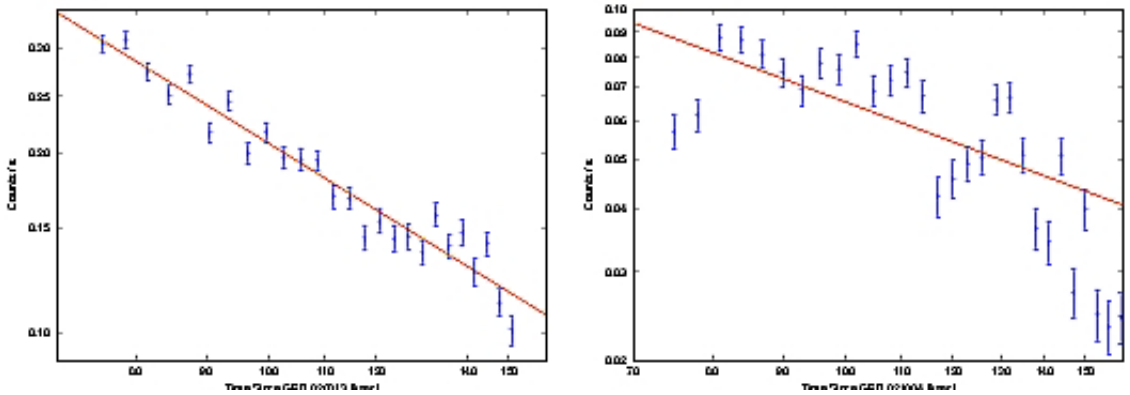

Figure 5-3: As a function of time during the observation, each afterglow count rate can be described by a power-law with index α. For GRB 020813 (left plot) the data are well described by $\alpha = -1.38 \pm 0.06$ (smooth line). The count rate for GRB 021004 is somewhat variable in time. It can be described approximately as a power-law with temporal index $\alpha = -0.9 \pm 0.1$ (smooth line).

below for the X-ray afterglow spectra of GRB 020813 and GRB 021004.

5.3 Spectral Fitting

5.3.1 Introductory Remarks

Traditionally, the field of X-ray spectroscopy has suffered from relatively low spectral resolution ($dE \sim$ 100eV at 1 keV for a CCD). Discrete spectral features must in general be regarded as broad additive components, much as one views additional continuum components. It is customary to treat the significance of a possible emission line in a data set by determining the χ^2 difference between fits of a null model (e.g. a simple power-law) and a more complex model involving the line profile function (e.g. a Gaussian). This test-statistic is then compared to the standard, tabulated reference distributions to determine significance. This is the likelihood ratio test or, equivalently, the F-test. Protassov et al. (2002) argue that this procedure is critically flawed, because the null value of the Gaussian norm (i.e. zero) lies on the boundary of the parameter space of the more complex model, and this invalidates the assumption of normality. Those authors suggest instead a rigorous procedure involving generation

of the prior distribution for each null model parameter using Markov Chain Monte Carlo (MCMC) methods (see, e.g., van Dyke et al., 2001). Realizations of the null model are then used to construct the true test-statistic distribution. While this procedure starts each Monte Carlo iteration with a technically correct null model, fits of the more complex model are unreliable for our purposes. This is because standard minimization routines tend to get stuck in local minima of the parameter space. Overcoming this deficiency through grid searches of the parameter space is time-consuming and impractical. It is common practice in the literature for lines in X-ray afterglow spectra to simply quote the deprecated F-statistic probabilities or, in rare instances (i.e. GRB 011211, Reeves et al. (2002)), to attempt Monte Carlo simulations. Both are suspect.

The above picture is subtly different in the case of high resolution ($dE \sim 1$ eV at 1 keV) gratings spectroscopy. As discrete features can be very narrow compared to the energy range of the full data set, it is often possible to fit the continuum emission independently from the line emission. Statistically significant lines can be present without appreciably affecting the continuum model fit. For broad lines, however, the problem will remain coupled as described above, and one must check for this. Assuming the lines are narrow, the analysis of the statistical significance of the lines can be greatly simplified, as demonstrated by the simple counting technique employed in Section 5.3.3.

5.3.2 Data Reduction and Continuum Fits

We reduce the HETGS spectral data from the standard L2 event lists using IDL and custom scripts, described in Marshall et al. (2002). For the 0th order spectral data, we use the CIAO[1] processing exclusively. Each data set is corrected for quantum efficiency degradation[2] due to contamination in the ACIS chips, prior to spectral fitting. We also "destreak" the S4 chip[3]. Spectral fitting and analysis is performed

[1]http://cxc.harvard.edu/ciao/
[2]http://asc.harvard.edu/cal/Acis/Cal_prods/qeDeg/
[3]http://asc.harvard.edu/ciao/threads/spectra_hetgacis/

with ISIS[4]. For each observation, we fit the HETGS HEG and HETGS MEG 1st-order data for the entire observation jointly. The +1 and -1 orders are combined for each grating. The data are then binned to a S/N ≥ 5 per bin, with the bin width restricted to $\delta E/E \leq 0.1$. We define S/N as the background-subtracted number of counts divided by the square root of the sum of the signal counts and the variance in the background. Bins of the maximal width with S/N < 3 are rejected, due to lack of signal. For GRB 020813, this selects an HEG energy range of $0.8 - 7.6$ keV and and MEG energy range of $0.6 - 5.2$ keV. For GRB 021004, this selects an HEG energy range of $1.0 - 4.6$ keV and and MEG energy range of $0.6 - 4.7$ keV. We fit each model by minimizing χ^2. Unless otherwise noted, all quoted errors are 90% confidence.

GRB 020813

As reported by Vanderspek et al. (2002), we find that an absorbed power-law fit to the 1st-order spectra requires no absorption column in excess of Galactic value. Therefore, in each model that we consider, we include absorption with $N_{\rm H}$ frozen to 7.5×10^{20} cm^{-2}.

The data are moderately well fit by a power-law (Figure 5-4, $\chi^2_\nu = 176.0/154$), with photon index $\Gamma = 1.85 \pm 0.04$ and normalization $(5.5 \pm 0.2) \times 10^{-4}$ photons/keV/cm^2/s at 1 keV. A thermal bremsstrahlung fit is a much poorer fit to the data ($\chi^2_\nu = 196.7/154$, rejectable at 99% confidence), with $kT = 4.6 \pm 0.5$ keV. We find consistent fits using the 0th-order data. Of note, a large fraction of the contribution to χ^2 in the case of the HETGS power-law fit arises between 1.2 and 1.5 keV. The addition of a Gaussian component in this energy range improves the χ^2 ($\chi^2_\nu = 160.5/151$). This improvement is at the 99.9% confidence level according the the likelihood ratio test ($\Delta\chi^2 = 15.5$ for 3 additional degrees of freedom). However, this method for determining significance is deprecated (see, Protassov et al., 2002), and we present Monte Carlo calculations for the significance below in Section 5.3.3. The line energy is 1.31 ± 0.01 keV, with a width of 8 ± 4 eV (1σ). The rest-frame equivalent width is 67 ± 32 eV, and the flux is $(1.6 \pm 0.8) \times 10^{-14}$ erg cm^{-2} s^{-1}. Given the optically

[4]http://space.mit.edu/CXC/ISIS/

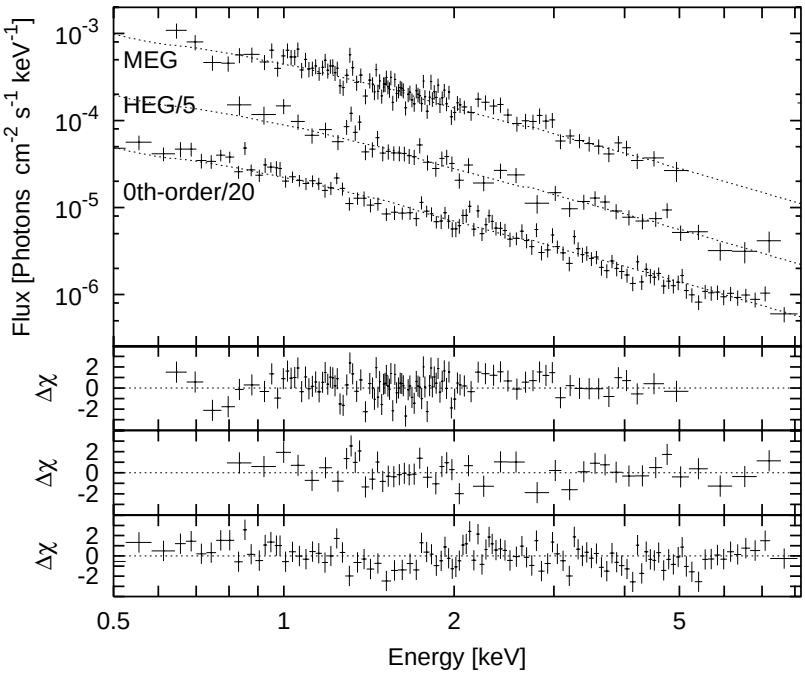

Figure 5-4: The ±1 order HETGS (HEG/MEG) data for GRB 020813 are moderately well fit by an absorbed power-law (Section 5.3). The 0th-order data (S/N ≥ 5 per bin) are also fit well by this model. Here we divide the HEG data by a factor of 5 and the 0th-order data by a factor of 20 for ease of viewing.

measured GRB host galaxy absorption redshift $z \geq 1.254$ (Price et al., 2002), a likely association for this line is S XVI Kα, blue-shifted by $0.12c$ from $z = 1.254$. The χ^2 is marginally improved ($\chi^2_\nu = 155.7/150$) with the inclusion of an additional Gaussian component of the same width, constrained to lie at predicted energy of Si XIV Kα (1.01 keV at $z = 0.99 \pm 0.01$). From the likelihood ratio test, the confidence for the pair can be estimated as 99.96% ($\Delta\chi^2 = 20.3$ for 4 additional degrees of freedom). Allowing the widths to vary jointly, the best fit width value is 10 ± 9 eV.

We also attempt to fit these data using a collisional ionization equilibrium (CIE) plasma model, as has been done previously in the case of several recent GRB afterglows observed with *XMM-NEWTON* (Reeves et al., 2002; Watson et al., 2002). We form the model using the Astrophysical Plasma Emission Database (APED) accessible through ISIS, with the redshift fixed at $z = 0.99$. We utilize a turbulence velocity $v_{\rm T}$, fixed at 2000 km/s, and thermal line profiles to produce the best-fit line widths above. We fix the abundance of metals lighter than Mg to solar. We tie the Si abundance to the S abundance, and allow Ni to vary freely. All other metals are frozen to

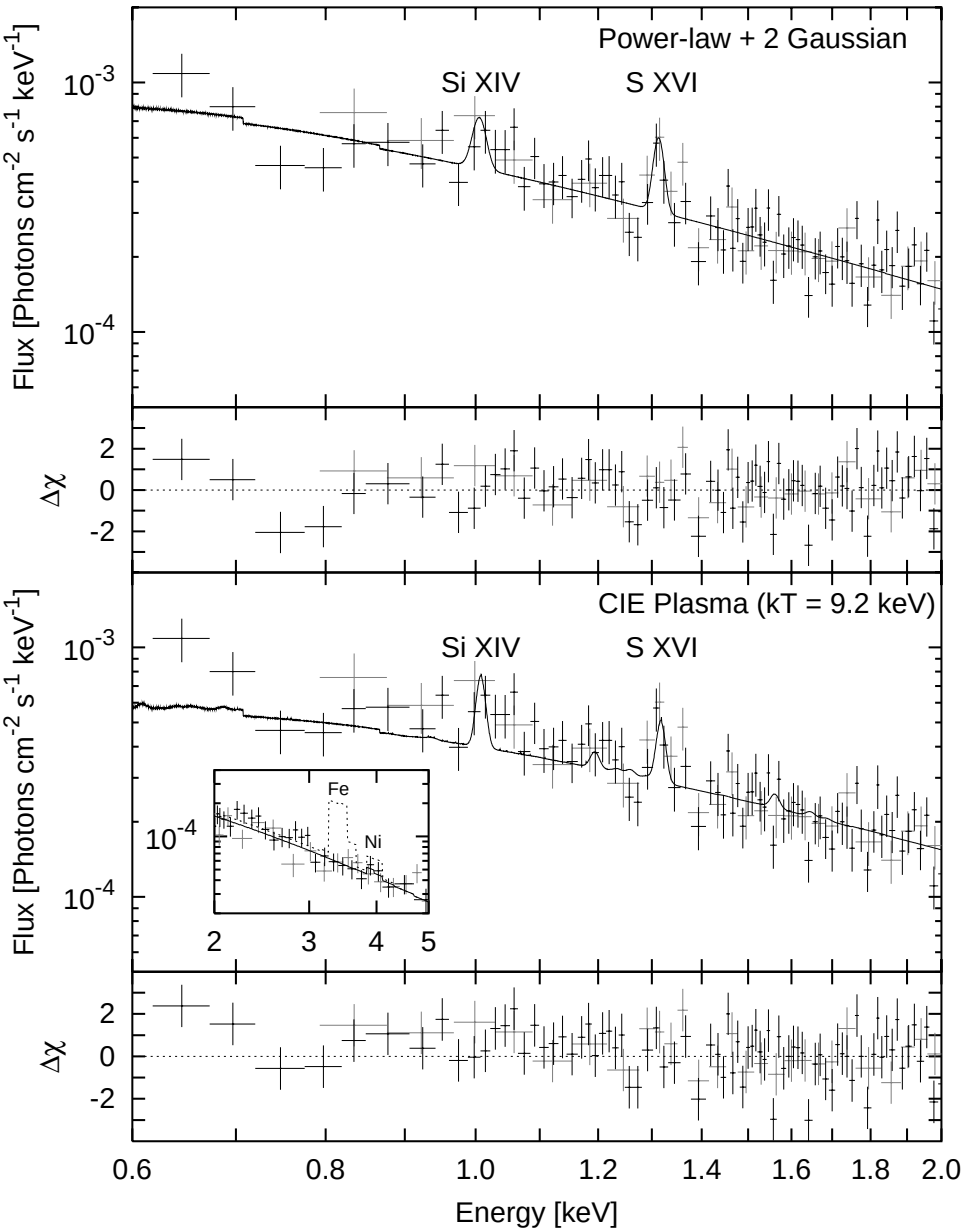

Figure 5-5: The power-law fit to GRB 020813 is improved by adding two Gaussian's at the energies of blue-shifted (by 0.12c) S XVI Kα and Si XIV Kα. The lines and continuum can be modeled less effectively by a CIE plasma model (bottom plot) containing Si, S, and Ni. The inset panel in the bottom plot shows the 2-5 keV portion of the CIE plasma model fit with (dotted line) and without (1.8 times solar abundance in) Fe; an abundance of Fe similar to the abundances for Si and S is strongly ruled out. The HEG data are plotted in grey. The MEG data are plotted in black.

zero abundance. The CIE plasma fit (Figure 5-5, $\chi^2_\nu = 177.8/152$) is slightly poorer than the pure power-law fit. Allowing the APED metal abundances previously set to zero to vary does not improve the fit. The best fit plasma temperature is 9.2 ± 1.2 keV. The best fit S,Si abundance is 2.9 times solar, and the linked abundance is greater than solar at 98% confidence ($\Delta\chi^2 = 5.5$ for 1 additional parameter). The best fit Ni abundance is 1.8 times solar. There is a low (1.6σ) significance detection of a Ni-K line in the MEG spectrum. This features appears as two bins modestly over the power-law fit in Figures 5-4, 5-5 near 4 keV. The APED model fits these bins with a blend of K lines from H and He-like Ni. The APED model with an abundance of Fe comparable to the Si and S abundances would produce a very strong and easily detectable Fe-K feature (Figure 5-5 Inset). In Table 5.1, we report 1-parameter 90% confidence upper limits to the abundances of several elements, with upper limits to the line fluxes and rest-frame equivalent widths of H-like K lines in each species. In Figures 5-6, 5-7, and 5-8 we compare the abundances, line luminosities, and rest-frame equivalent widths, respectively, to those reported for other GRB X-ray afterglows.

Element	Abund.	Flux	EW [eV]
Mg	4.4	0.5	13
Si	5.8	1.9	53
	$(2.9^{+2.9}_{-1.6})$	(1.1 ± 0.8)	(30 ± 23)
S	4.3	2.3	72
	$(2.9^{+1.4}_{-2.0})$	(1.6 ± 0.7)	(50 ± 22)
Ar	1.0	0.2	9
Ca	1.8	0.4	15
Fe	0.1	1.5	100
Ni	4.4	1.5	110
	$(1.8^{+2.6}_{-1.8})$	$1.0^{+0.5}_{-1.0}$	73^{+37}_{-73}

Table 5.1: GRB 020813 line emission upper limits at 90% confidence for APED model elemental abundances, H-like Kα line fluxes ($\times 10^{-14}$ erg cm^{-2} s^{-1}), and rest-frame H-like Kα line equivalent widths. Values determined from power-law plus Gaussian fits. The observer-frame line widths were set via $dE/E = v_t/c \approx 0.0067$. Line centers are set with $z = 0.99$.

Since, the abundances of α-particle nuclei produced by core-collapse SNe are expected to be approximately the same (see, e.g., Rauscher et al., 2002), relative to

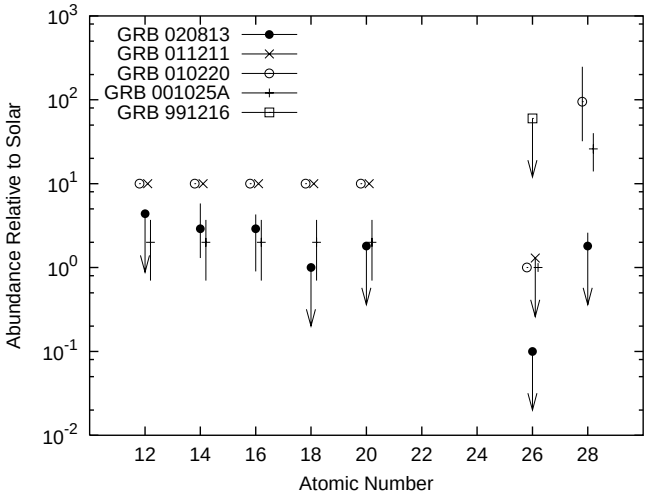

Figure 5-6: Metal abundances for the APED plasma model for GRB 020813 (solid circles), as in Table 5.1. Also plotted are the abundances reported in the literature for several other GRB X-ray afterglow spectra. The values for GRB 011211 come from Reeves et al. (2002). The values for GRB 010220 and GRB 001025A come from Watson et al. (2002). The value for GRB 991216 has been taken from Piro et al. (2000). Error bars have been plotted where available.

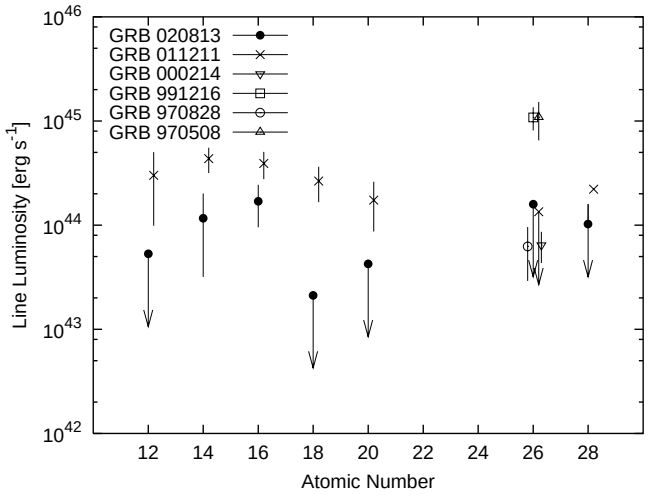

Figure 5-7: Isotropic equivalent line luminosities from Gaussian fits (Table 5.1) for GRB 020813 (solid circles, host at $z = 1.254$) and for several other GRBs in the literature. To determine luminosity distances, we use a cosmology with $\Omega_m = 0.3$, $\Omega_\Lambda = 0.7$, and $h = 0.65$. The values for GRB 011211 come from Reeves et al. (2002), with $z = 2.14$. The value for GRB 000214 comes from Antonelli et al. (2002), with $z = 0.47$. The value for GRB 991216 has been taken from Piro et al. (2000), using $z = 1$. The value for GRB 970828 comes from Yoshida et al. (1999), using $z = 0.33$. The value for GRB 970508 comes from Piro et al. (1999), using $z = 0.835$. Error bars have been plotted where available.

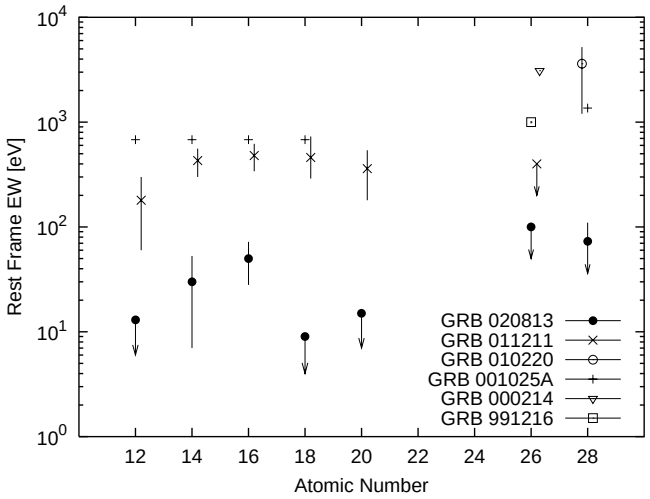

Figure 5-8: Rest-frame equivalent widths in eV from Gaussian fits (Table 5.1) for GRB 020813 (solid circles, $z = 0.99$) and for several other GRBs in the literature. The values for GRB 011211 come from Reeves et al. (2002), with $z = 1.88$. The values for GRB 010220 ($z = 1.0$) and GRB 001025A ($z = 0.7$) come from Watson et al. (2002). The value for GRB 000214 comes from Antonelli et al. (2002), with $z = 0.47$. The value for GRB 991216 has been taken from Piro et al. (2000), using $z = 1$. Error bars have been plotted where available.

solar, the low relative upper limits we find for the abundances of Ar and Ca possibly indicate that the Si and S lines are not the result of thermal emission from a hot plasma. After radioactive decay, we would expect an Fe abundance similar to the light, multiple-α metal abundances. This implies that the line fluxes from one or more of the Fe group elements (Fe, Ni, Co) should be higher than we observe. We discuss below the possibility that the lines are due to reflection. An alternative possibility, suggested in part by the APED model's apparent tendency to under-fit the continuum below $\sim$ 1.5 keV (Figure 5-4), is that we must also include a power-law component. It is then possible to use the APED model with a lower temperature ($\sim$ 2 keV), and this weakens the high energy continuum and the lines from Ar, Ca, and the Fe group elements relative to the Si and S lines. We find models with a single abundance for the α-particle nuclei and Fe which improve upon the power-law fit but do not appear to be as good as the power-law plus two Gaussian fit. If the 0th order data are included in the fit (jointly), then it is seen that the APED model does not adequately fit the data ($\chi^2 = 315.2/249$, rejectable at 99.7% confidence). Finally, we

note that the abundances quoted in Table 5.1 lose meaning if a power-law component is present in addition to a thermal component.

GRB 021004

An absorbed power-law fit to the 1st-order spectra does not require an absorption column in excess of the Galactic value, as reported by Sako & Harrison (2002). Therefore, in each model that we consider, we include absorption with $N_{\rm H}$ frozen to 4.24×10^{20} cm^{-2}.

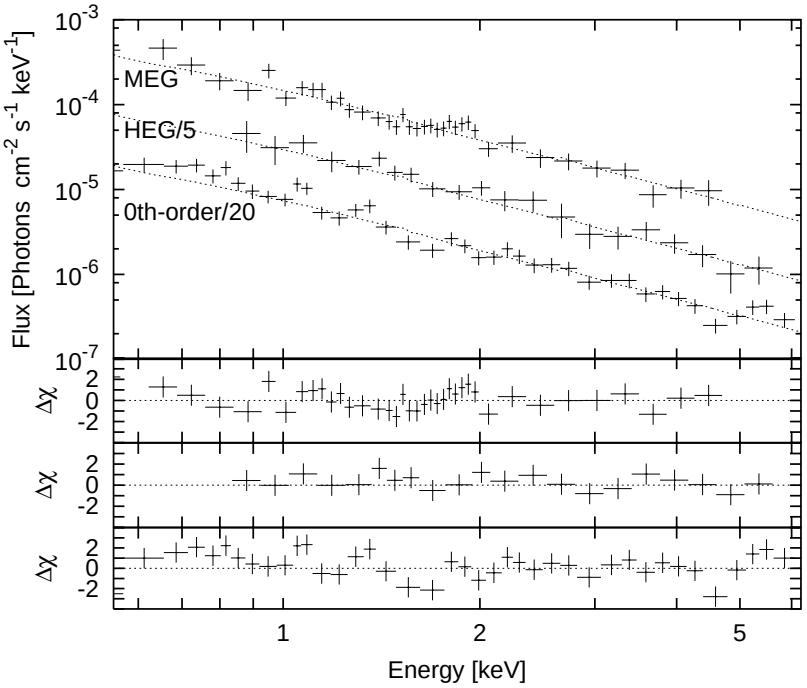

Figure 5-9: The ±1 order HETGS (HEG/MEG) data for GRB 021004 are very well fit by an absorbed power-law (Section 5.3). The 0th-order data (S/N $\geq$ 5 per bin) are also fit well by this model. Here we divide the HEG data by a factor of 5 and the 0th-order data by a factor of 20 for ease of viewing.

The data are very well fit by a power-law (Figure 5-9, $\chi^2_\nu = 39.5/55$), with $\Gamma = 2.01 \pm 0.08$ and normalization $(1.7 \pm 0.1) \times 10^{-4}$ photons/keV/cm^2/s at 1 keV, consistent with the values found by Sako & Harrison (2002) and Holland et al. (2002). A thermal bremsstrahlung fit is a somewhat poorer, though still very acceptable, fit ($\chi^2_\nu = 47.2/55$), with kT $= 3.2 \pm 0.4$ keV. We find consistent fits using the 0th order

data (Figure 5-9).

5.3.3 Line Searches

In gauging the significance of the possible lines found for GRB 020813 discussed above, we must take into account the number of trials performed (i.e. line widths and line energies searched). Considering possible lines from the Kα transitions in Mg, Si, S, Ar, Ca, Ni, Co, and Fe, with the possibility that any lines may be blue-shifted (or red-shifted) by ~ 0.1c, each bin of the spectrum is a source of potential line photons. The binning is set based on a minimum reasonable number of counts per bin, and we analyze two additional binnings just in case we were lucky (or unlucky) in choosing the initial binning.

GRB 020813

Figure 5-10 displays the power-law model found above over-plotted on the summed HEG+MEG counts, at three binnings. The finest binning is chosen so that each bin between 1.5 and 16.0 Å contains one or more counts. We rebin twice by a factor of approximately two in order to look for broader features. The 1.31 keV (9.4 Å) feature is seen in both the top and middle plots at 4.0σ. This significance describes the Poisson probability that the signal plus background counts could reach a value greater than or equal to the observed values, with the Poisson mean fixed to the number of counts predicted by the model plus the background. The probability for a chance fluctuation of this or greater significance in one or more of the 235 bins shown in Figure 5-10 is approximately 1.5%, calculated as $P_N \approx 1-(1-P_1)^N$. From Monte Carlo simulations of 10^4 spectra using the best fit power-law model above, we find $P_N = 1.4\%$. From the simulations, we find that the probability for getting two or more 4σ fluctuations (as observed) is 0.1%. Thus the line is detected at 3.3σ significance. A broad feature corresponding to the 1.01 keV line mentioned above is observed in the third panel (and also in the 1st panel) of Figure 5-10 at $\sim$ 12.2 Å, with a significance of 2.9σ. We estimate a 58% probability that a 2.9σ or greater

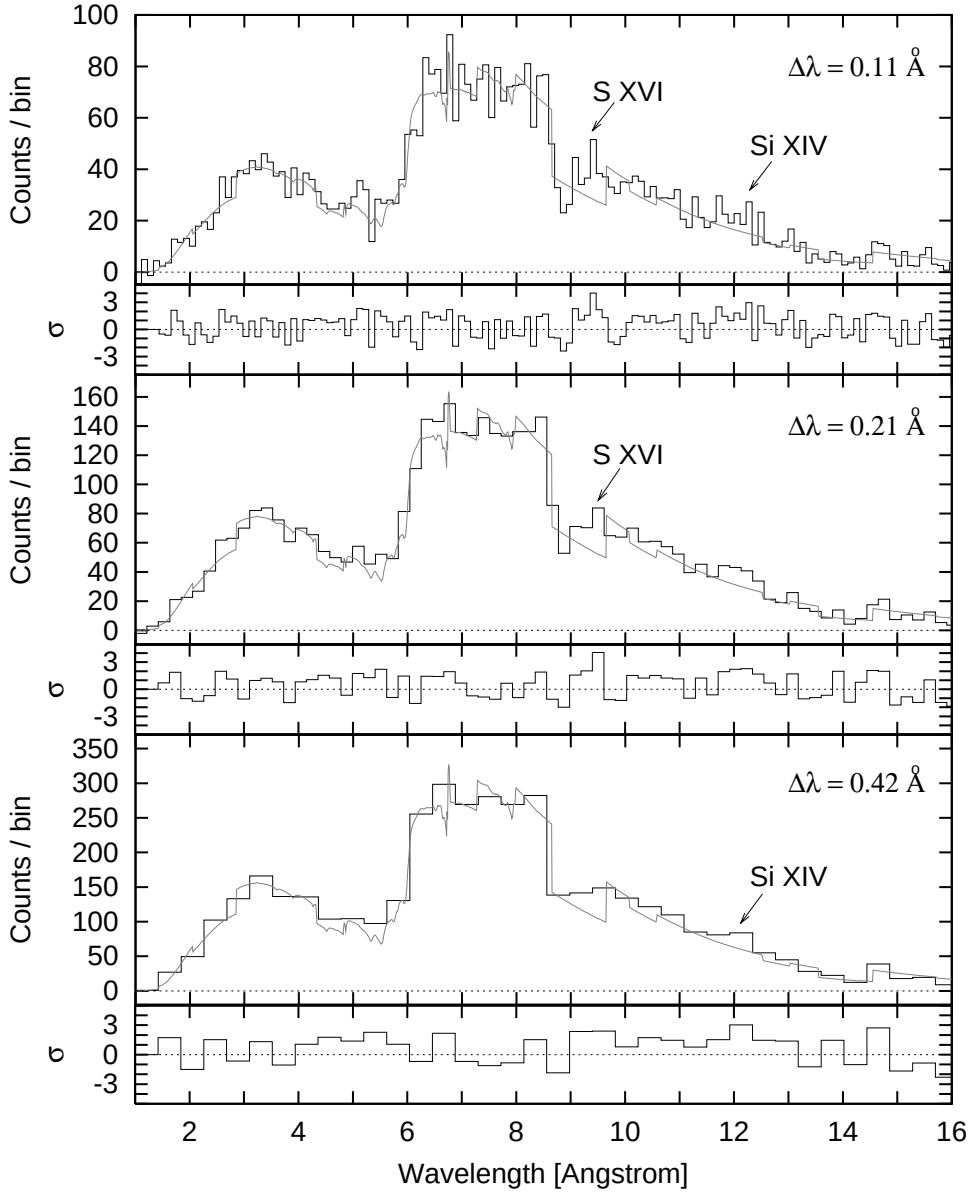

Figure 5-10: The best fit power-law model on top of the combined HETGS HEG+MEG data, at 3 binnings, for GRB 020813. The significance (reported in σ units) of deviations from the model are calculated using Poisson statistics. We associate the residuals near 9.4 Å in the top and middle plots with H-like S. We associate the high bin near 12.1 Å in the top and bottom plot with H-like Si.

fluctuation would occur by chance in one or more of the trials. From the Monte Carlo simulations, the probability for getting two or more 2.9σ fluctuations is 23%. Thus the line is detected at very low (1.2σ) significance in a blind search, and it is potentially meaningful only if the line location is constrained as in the preceding paragraph. No additional features at or above 2.9σ are present in the HETGS spectrum at the binnings searched. Finally, we derive a 3σ upper limit of 20 eV for the equivalent widths of any lines unresolved in this search (FWHM $\ll$ 0.11 Å) between 6 and 16 Å. This figure grows $\propto \lambda^{-3}$ shortward of 6 Å.

GRB 021004

For GRB 021004, we plot the combined HEG/MEG data in count space with the power-law model over-plotted in Figure 5-11, for the same binnings as in Figure 5-10. No significant features are observed. The largest fluctuation occurs in the middle panel, where one of the $\sim$ 70 bins reaches 2.6σ. There is approximately an 89% chance that this would happen by chance in one or more of the bins in that plot. At the 3σ level, this search is sensitive to moderately broad (FWHM $\sim \delta\lambda$) emission and absorption lines between 6 and 16 Å with equivalent widths greater than 50 eV. Over this same wavelength interval, we derive a 3σ upper limit of 35 eV to the equivalent widths of any narrow lines (FWHM $\ll$ 0.11 Å). These figures grow $\propto \lambda^{-3}$ shortward of 6 Å. Considering the GRB redshift of 2.328 determined in the optical by Mirabel et al. (2002), several K-lines from S, Ar, Ca, Fe, Co, and Ni would have been detected were their equivalent widths larger than these estimated limits.

5.4 Temporal Analysis

As displayed in Figure 5-12, the afterglow continua, though moderately variable in the case of GRB 021004, do not appear to evolve spectrally. To search for time-variable discrete features, we divide the summed HEG+MEG data sets into 2, 4, or 8 portions of equal numbers of counts. For each time section, we examine the counts data at 3 binnings: 0.11, 0.21, and 0.42 Å (as in Figures 5-10, 5-11). For each

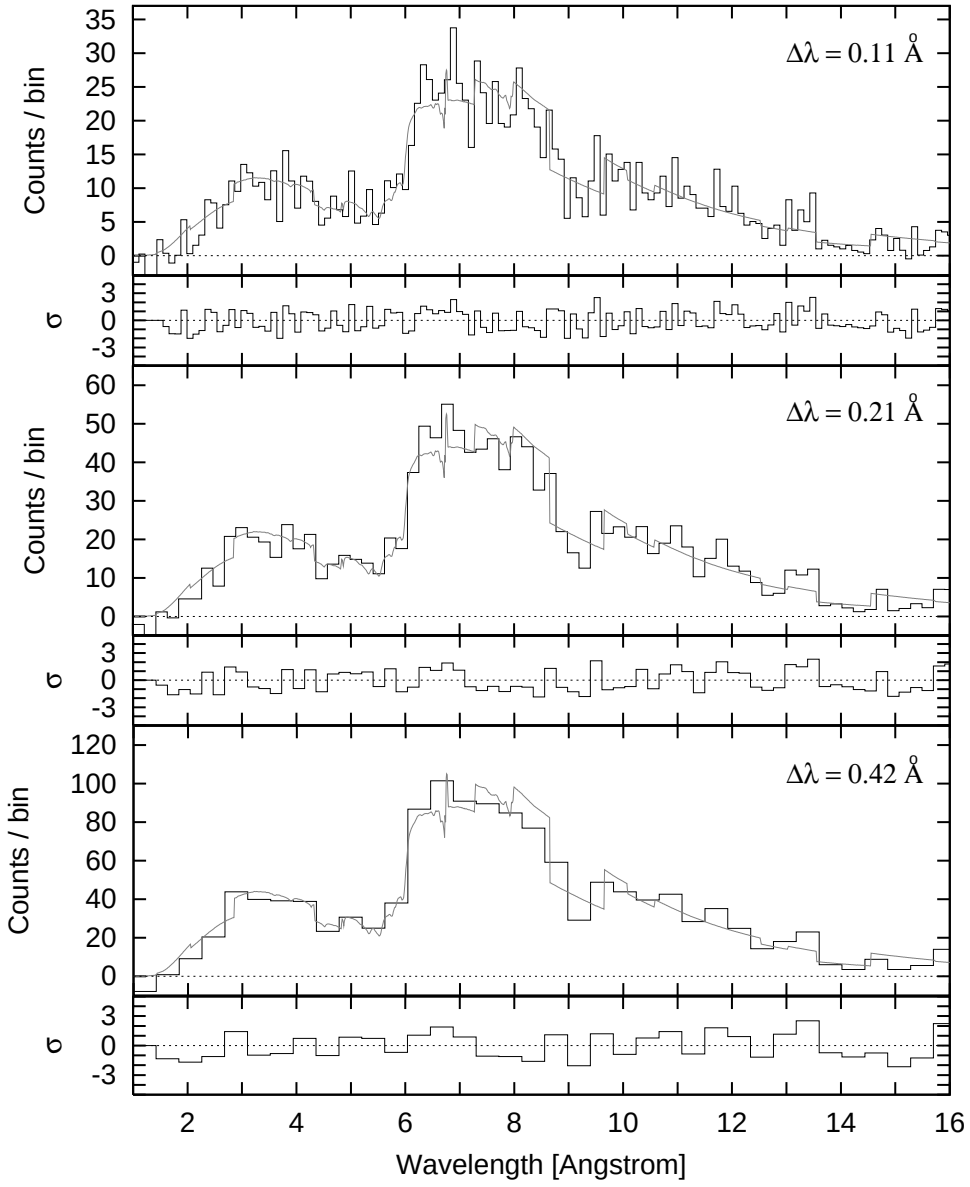

Figure 5-11: The best fit power-law model on top of the combined HETGS HEG+MEG data, at 3 binnings, for GRB 021004. No highly significant deviations from the model are observed.

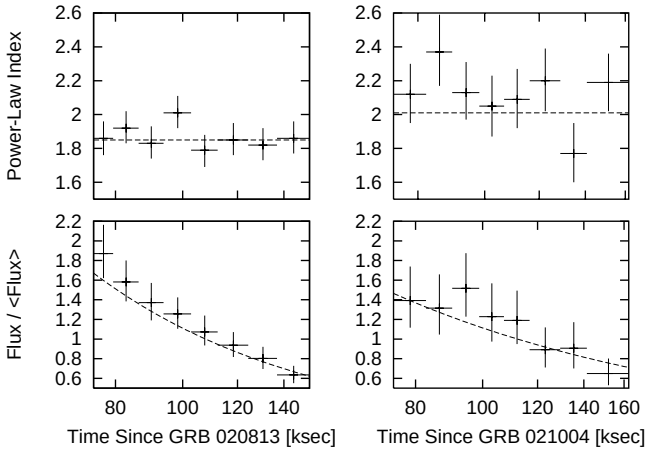

Figure 5-12: To look for spectral variability, the HETGS data for each GRB are divided into 8 regions of equal counts and fit with absorbed power-laws by minimizing the Cash (1979) statistic. The above plots show the power-law indices Γ and the (energy) fluxes found for each fit, with the best-fit Γ's derived for the entire data set and the best-fit temporal fade found for the count rates overplotted as dashed lines. The fluxes have been divided by the mean fluxes for each observation reported in Section 5.2. Error bars are 90% confidence, determined from the 1-parameter confidence intervals.

GRB afterglow, we fit absorbed power-law models to each of these 42 data sets by minimizing the Cash statistic (Cash, 1979). We then search the bins between 1 and 16 Å for deviations from the best fit model, interpreting the deviations using Poisson statistics as in Section 5.3. We set a limiting detection threshold of 3.7σ so that fewer than one chance detection is expected in 15×235 bins searched. The search yields no emission or absorption line detections in the case of GRB 021004, while for GRB 020813 only the Si and S lines (Section 5.3) are detected. The Si XIV Kα line is detected at 3.7σ ($P_N \approx 53\%$) in the second quarter (12-28.5 ksec) of data, while the S XVI Kα line (3 detections) peaks at 4.3σ ($P_N \approx 6\%$) in the first quarter (12 ksec) of data. In Figure 5-14, we plot the S XVI Kα line flux (measured with Gaussian fits of fixed width and location) and the continuum flux versus time. Using the likelihood ratio test, we find evidence for a decrease in equivalent width between the first 28.5 ksec of data and the remainder of the observation at 97% confidence ($\Delta\chi^2 = 4.7$ for 1 additional parameter).

5.5 Discussion

Evidence that the Lines are Real

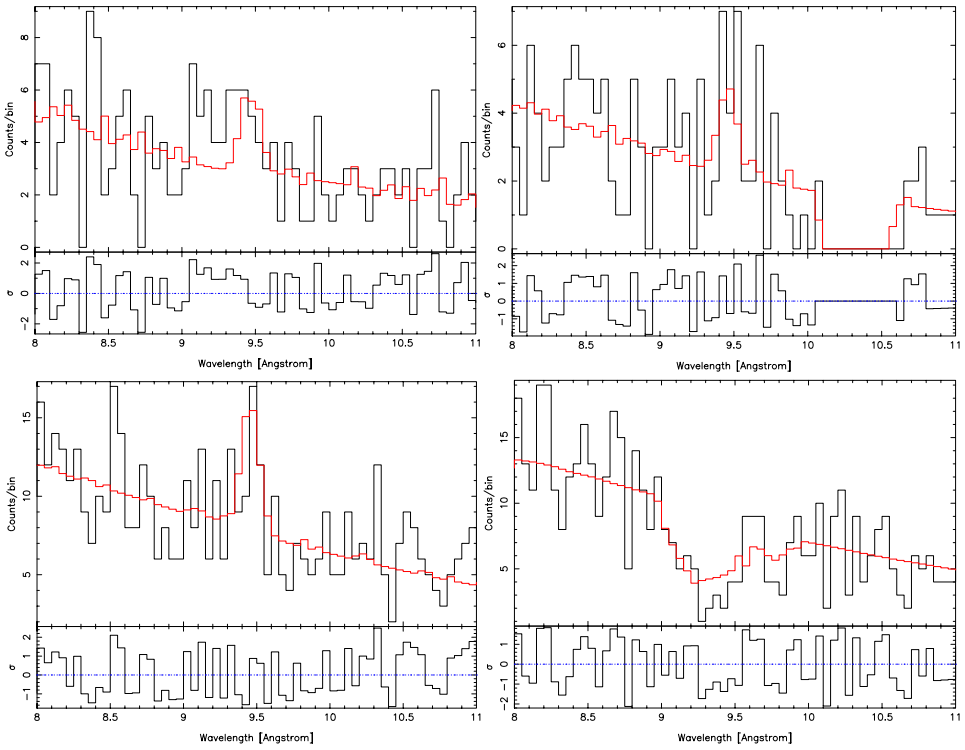

Figure 5-13: The best-fit power-law continuum plus Gaussian line models from Section 5.3.2 are plotted over the data at 0.05 Å binning for each of the four independent spectra. From top left to bottom right, the plots are of the HEG minus and plus orders and the MEG minus and plus orders. There is a chip gap at the line location in the MEG +1 order spectrum, and we use the standard CIAO processing to extract counts for this region using the satellite aspect solution. (Our analysis using IDL scripts ignores all of these counts.) As shown in Table 5.2, the line counts in each spectrum are consistent with the model derived in Section 5.3.2.

The most significant discrete feature we observe in afterglow spectrum of GRB 020813 is clearly the line we associate with S, which we detect at 3.3σ significance. This is a somewhat marginal detection. However, the reality of the line is supported by the presence of line counts in various times slices throughout the observation and in each of the four independent 1st-order spectra (MEG/HEG ± 1 orders). For the full observation no detector anomalies (e.g. flares, flickering pixels) are observed in the ACIS-S CCD regions yielding the HETGS MEG/HEG ± 1 order counts from this

Grating	Expected Line Counts	Detected Line Counts
HEG -1	9.3	$9.3^{+10.1}_{-6.6}$
HEG $+1$	7.5	$9.2^{+11.7}_{-5.6}$
MEG -1	25.8	$17.9^{+15.1}_{-9.6}$
MEG $+1$	10.8	$3.2^{+9.8}_{-3.2}$

Table 5.2: Line photons are detected in each of the four independent spectra at consistent levels. The expected number of counts is determined from the Gaussian line model from Section 5.3.2. Errors are 90% confidence. There are fewer net counts in the MEG $+1$ order spectrum that in the MEG -1 order spectrum due to a chip gap.

line. The background is negligible between 0.6 and 6 keV, contributing only 3% of the total counts. Pileup in the grating spectrum is not a concern for this observation due to the very low count rate. Excess counts corresponding to the line are detected in each independent spectrum, and the numbers are consistent at the 1.5σ level. The combined 1st-order spectra (MEG/HEG) show a consistent number of excess counts at the 1σ level. The validity of this line detection is possibly strengthened by an association with S XVI Kα and by a marginal detection of a line at the expected energy for Si XIV Kα. We have performed a parallel reduction for the GRB 021004 afterglow data, and this has yielded no convincing evidence for discrete spectral features.

Interpretation

Although we find marginal evidence for temporal variability in the line emission for GRB 020813 (Section 5.4), the lines are detected in the full 76.8 ksec observation, and the full data set is moderately well fit by a plasma in collisional ionization equilibrium (Section 5.3). Figures 5-6-5-8 show the line and metallicity parameters we derive in relation to those reported for other GRBs in the literature. Our required abundances are only modestly super-solar (Section 5.3), in contrast to those reported for several other GRBs. The line luminosities are quite low, and the rest-frame equivalent widths are an order of magnitude smaller than those reported for any other GRB. Figure 5-14 shows the GRB 020813 continuum and S XVI line fluxes versus time alongside the data for GRB 011211 from Reeves et al. (2002). In comparison to GRB 011211, it appears that the longevity of the line emission (and also the narrowness of the lines)

was critical to their detection, whereas the 10 times stronger continuum could easily have hidden less persistent emission.

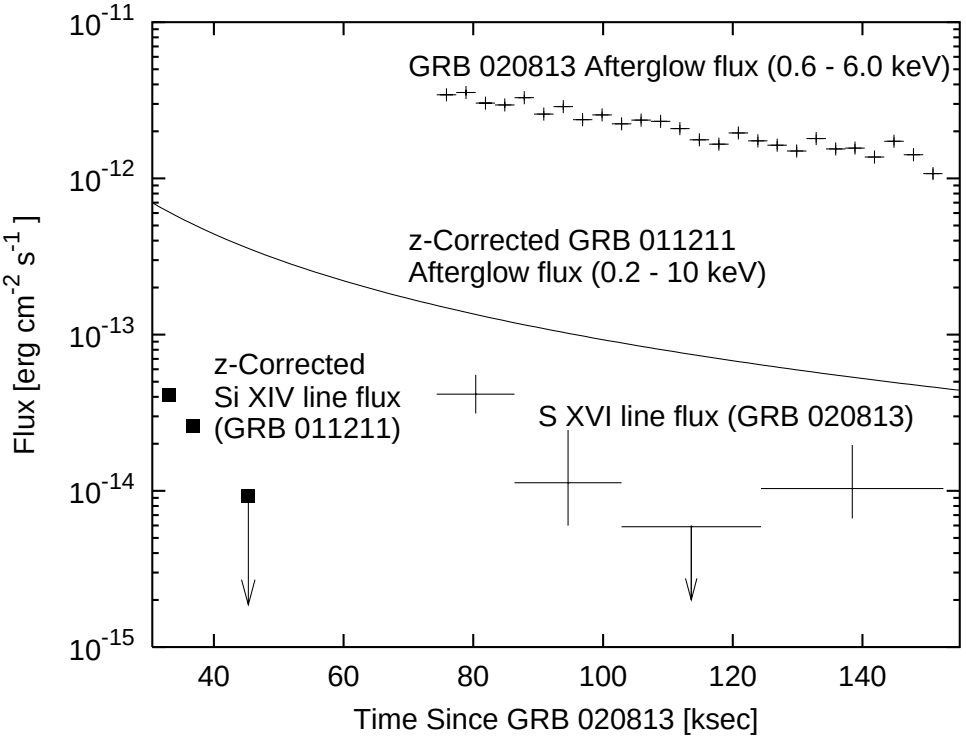

Figure 5-14: The points on the left show the Si XIV Kα line flux for GRB 011211 from Reeves et al. (2002), corrected to the redshift of GRB 020813. The integrated afterglow flux for GRB 012111 is also plotted and extrapolated. We employ a cosmology with $\Omega_m = 0.3$, $\Omega_\Lambda = 0.7$, and $h = 0.65$. At a later time (~ 50 ksec later in the GRB frame), we measure a similar line flux. However, the GRB 020813 afterglow flux is approximately an order of magnitude higher that that of GRB 011211. On the right, we plot the measured line flux from S XVI Kα, and the afterglow flux, versus time since GRB 020813. Error bars and the one upper limit are at 1σ confidence.

We can interpret the longer duration and later onset of the lines for GRB 020813 relative to GRB 011211 (Figure 5-14) as a purely geometrical effect due to observing emitting material residing at a larger radius R from the GRB. For radially expanding emitting material heated by GRB photons or by the GRB shock, the narrowness of the lines requires that the emission comes from only a small solid angle ($\Omega \lesssim 0.4$), as viewed from the GRB, consistent with GRB beaming models (Frail et al., 2001). The line duration ($t_{\rm line} \gtrsim 76.8$ ksec) can be attributed to time delays across a thin shell (Figure 5-15), and this leads to the requirement $R = \frac{ct_{\rm line}}{1+z}\frac{2\pi}{\Omega} \gtrsim 10^{16}$ cm. An

estimate $R \lesssim 10^{18}$ cm for the maximum likely R is determined using the smallest solid angle found for a GRB jet in Frail et al. (2001). For the reprocessing material to lie this far out from the GRB, it must have gotten there prior to the GRB. The line identifications we have made (Section 5.3) require a blue-shift $\sim 0.1c$, and this high an outflow velocity implicates expanding SN ejecta rather than a stellar wind. The SN would have gone off 0.1 to 10 years prior to the GRB. The need for a precursor SN can be avoided if the GRB host (absorption) redshift is taken as a lower limit on the redshift, rather than the actual redshift. In that case, an identification of the S XVI and Si XIV lines with Ar XVIII and S XVI ($z = 1.53$, no blue-shift), respectively, could be made.

In the case of GRB 011211, Reeves et al. (2002) assert that a shell of thermal plasma at $R \sim 10^{15}$ cm can account for the afterglow spectrum and for the duration of the reported emission lines. Taking into account radiation transfer across the shell, Lazzati (2002) argues that a larger radius is required ($R \gtrsim 10^{17}$ cm), because the large afterglow luminosity implies a high density, which implies a cooling time much shorter than the observed line duration. Following Lazzati (2002), we find that a thermal model for GRB 020813 also implies $R \gtrsim 10^{17}$ cm, except for the case (discussed below) where the luminosity of the thermal component is actually overwhelmed by a (~ 10 times brighter) power-law continuum component. In this case, a solution with $R \sim 10^{16}$ cm is possible. The density is low ($n \sim 10^8$ cm^{-3}), and this implies a shell with thickness $dR \sim R/10$ for $\tau_{\rm T} = 0.1$. At larger radii, the shell must be either very thin or very clumped for the contained mass to be similar to that expected from SNe ($M_{\rm ejecta} \lesssim 20 M_\odot$, Woosley & Weaver (1995)).

It is our opinion that the acceptable thermal model fit to the HEG+MEG data is not to be trusted, and this is reinforced by the poor fit that that model yields when the 0th order data are included (Section 5.3.2). This makes sense, as the wider energy response of the 0th order data should allow for more sensitivity to the curvature in the thermal model continuum. We see three additional reasons, which arise from complexities in our modeling, to be cautious in interpreting our results as evidence for a persistent thermal component. First, we observe lines with best fit

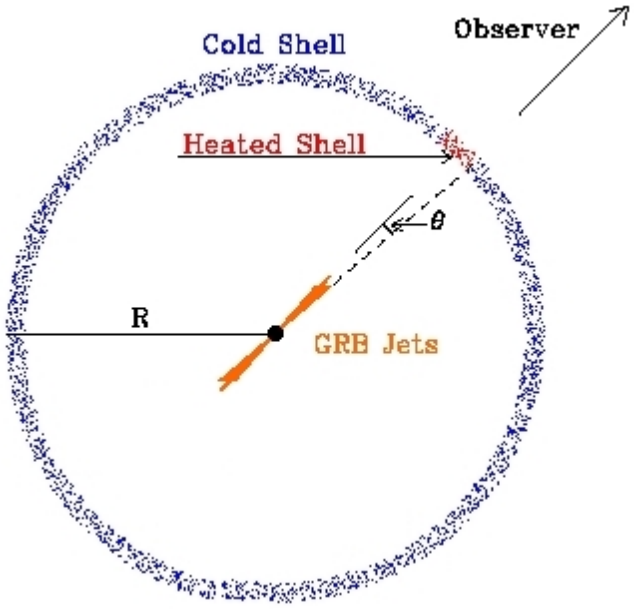

Figure 5-15: Cartoon of a thin, SN shell heated by GRB photons or by the GRB shock over a narrow solid angle $\Omega = 2\pi(1 - \cos\theta/2) \lesssim 0.4$. The heated shell radiates isotropically. Figure adapted from Lazzati (2002).

widths an order of magnitude larger than the thermal line widths. We account for this in the thermal model by introducing a turbulence velocity of 2000 km/s. It is also possible that this broadening is kinematical. Second, the best-fit CIE plasma model has marginally dissimilar abundances for the multiple-α elements (Figure 5-6) and very low abundances for the Fe group elements relative to the multiple-α elements (Figure 5-6, Figure 5-5 Inset). This would require an unusual chemical composition for the emitting medium, a mechanism beyond the APED model for suppressing emission from metals other than Si and S, or the addition of a power-law continuum component to the model as discussed in Section 5.3. Third, the data do not tightly constrain the relative contributions to the continuum from the CIE plasma and from this possible power-law component. Indeed, the continuum appears non-thermal, as would be expected for the X-ray afterglow of the burst.

These considerations argue strongly against a thermal model, and the *XMM-NEWTON* observers who initially favored that model (Reeves et al., 2002) appear to be moving toward photo-ionization models (see, Watson et al., 2003). Reflection

models may more naturally describe a spectrum with broad lines superposed on a power-law continuum (see, e.g., Ballantyne et al., 2001; Vietri et al., 2001). In these models, the line broadening is due to Compton scattering. If the electron temperature is similar to the line energy, we expect $\sigma_E/E \sim (kT/m_e c^2)^{1/2} \sim 0.05$ (at 1.3 keV) for a single scattering. Because this is already a factor ~ 5 times larger than the observed widths, we require the reflector to not be highly ionized. Consulting Figure 5-16, it appears that our observed dissimilarity in line luminosities (Table 5.1, Figure 5-7) may further reinforce this conclusion. The reflection models of Lazzati, Ramirez-Ruiz, & Rees (2002), with ionization parameter ξ in the range $10 < \xi < 100$, can produce Si and S line luminosities which are an order of magnitude greater than luminosities of lines from Ar, Ca, and Fe. In the case of GRB 011211, Lazzati et al. (2002) argue that the large line equivalent widths rule out nearby reprocessor models. This is not the case for GRB 020813, and the line duration may be set by a delayed energy injection rather than by the geometry of the reprocessing material (see, Rees & Meszaros, 2000; Meszaros & Rees, 2001). In this case, we would not need a two-step (SN then GRB) explosion.

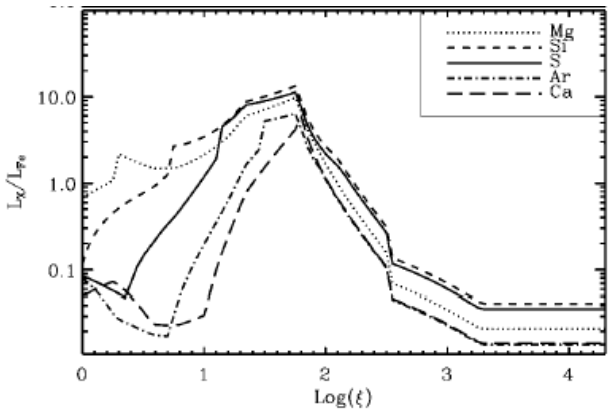

Figure 5-16: Flux in light metal lines relative to the flux in Fe as a function of the ionization parameter ξ, taken from Lazzati, Ramirez-Ruiz, & Rees (2002). Light metals dominate for $\xi < 100$.

In conclusion, we detect lines from an over-abundance of light metals characteristically produced in massive stars during pre-supernova nucleosynthesis in the X-ray afterglow of GRB 020813. The long S XVI line duration and narrow line widths can

be explained via the geometry of the emitting material, and this would likely require a two-step explosion as in the supranova (Vietri & Stella, 1998) scenario. The time delay between the SN and GRB is $\gtrsim 2$ months in this picture. In contrast, our weak detection of a Ni feature, with no detection of Fe (or Co), suggests a very short time delay ($\lesssim 1$ week) between the SN and the GRB. As discussed in Woosley, Zhang & Heger (2002), it is not likely possible to observe a GRB through a SN remnant this young; the Ni feature may indicate that the geometric picture is wrong. A thermal model adequately fits the full data set. A bright Fe (or Ni or Co) feature is not observed, however, and this is perhaps the strongest reason to favor a reflection model, where an Fe line can be quenched by Auger auto-ionization (Lazzati et al., 2002).

Chapter 6

Three Additional Long/Soft GRBs

6.1 Introduction

In Chapter 5, I discussed two high resolution spectra from *Chandra* and the discovery of spectral lines in the X-ray afterglow spectrum of GRB 020813. In that chapter, GRB 021004 was used much as a control to verify the analysis used to find the GRB 020813 lines. There are three additional bursts with high resolution *Chandra* spectra, and I now analyze these data to search for discrete spectral features. Table 6.1 shows the exposure times and net counts found for each of the five *Chandra* high resolution spectra. Of the three discussed in this chapter, only the data for GRB 991216 yielded a claimed line detection in the literature (Piro et al., 2000). My collaborators and I analyzed the GRB 030328 data (Butler et al., 2003f; Ford et al., 2003; Butler et al., 2003g) and reported no line detections. Null detections for GRB 020405 were reported by Mirabel et al. (2002a). I present a more detailed discussion of these data in this chapter. To summarize, I find that the Fe line for the GRB 991216 is robustly detected, while no significant discrete spectral features are present in the spectra for GRB 020405 and GRB 030328.

GRB	Exp (ksec)	Counts 0th Order	Counts ±1 Order	Comment
GRB 991216	9.7	456	737	Fe line and RRC reported.
GRB 020405	50.6	718	1304	
GRB 020813	76.9	3457	4243	S and Si lines reported.
GRB 021004	86.7	1098	1330	
GRB 030328	92.7	372	430	

Table 6.1: High resolution spectroscopic measurements of GRB X-ray afterglows have received greater and greater attention (i.e. exposure time) from *Chandra*. Five have been observed to date, two with the LETGS (GRB 020405 and GRB 030328), and three with the HETGS. The 0th order flux for GRB 020405 is smaller relative to the gratings (±1 order) flux in comparison with the other GRBs, because the 0th order image lies on ACIS-S2 rather than the more sensitive ACIS-S3.

6.2 Observations

The prompt GRB and *Chandra* observations for GRB 991216 and GRB 020405 are reported in Piro et al. (2000) and Mirabel et al. (2002a), respectively. GRB 991216 was detected by *BeppoSAX*, while GRB 020405 was detected by the IPN.

6.2.1 GRB 030328

Using Directors Discretionary Time, the bright and long duration GRB 030328 was observed with the *Chandra* Low Energy Transmission Gratings Spectrometer (LETGS) beginning March 29.112 UT (15.33 hours after the burst) and lasting until March 30.278 UT (43.32 hours after the burst). The GRB was detected and localized by *HETE* (Villasenor et al., 2003c), and a $2'$ radius SXC error region was circulated. The Gamma-ray light curve is shown in Figure 6-1. The fluence of the burst was approximately 3.0×10^{-5} erg cm^{-2} and the peak flux over 5.2 s was approximately 7.3×10^{-7} erg cm^{-2} s^{-1} in the 30-400 keV band.

The total livetime of the *Chandra* observation was 94.0 ksec. The afterglow candidate reported by (Peterson & Price, 2003) was clearly detected, and the mean, background-subtracted counting rate was 0.012 counts/s, including the dispersed signal from the LETGS and the 0th order flux. The decay in brightness over the full observation can be described by a power-law with a index $\alpha = -1.5 \pm 0.1$ (Figure

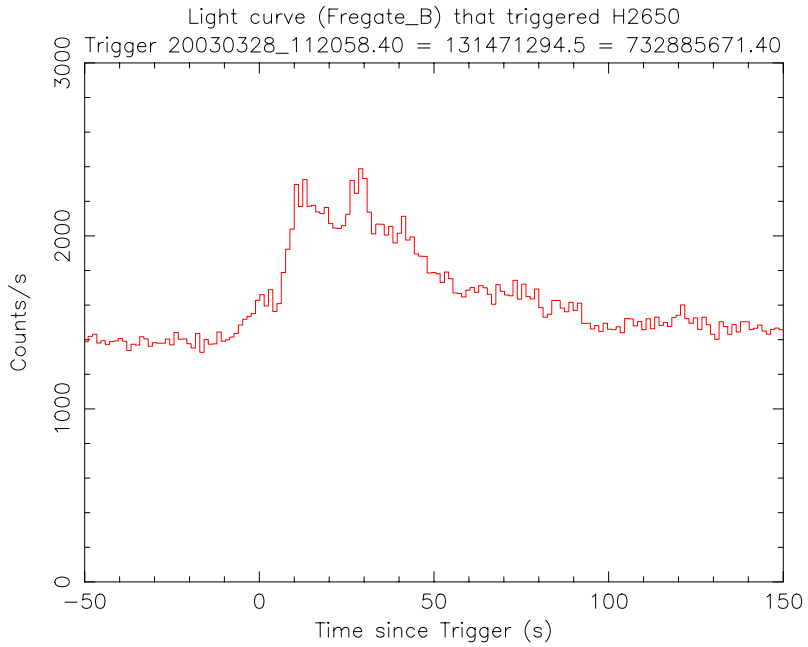

Figure 6-1: FREGATE light curve in the 30-400 keV band for GRB 030328.

6-2), consistent with the value reported by Ford et al. (2003).

6.3 Data Reduction and Continuum Fits

The HETGS spectral data are reduced from the standard L1 event lists using IDL and custom scripts, described in Marshall et al. (2002). For the 0th order spectral data, the CIAO[1] processing is used. Each data set is corrected for QE degradation[2] due to contamination in the ACIS chips, prior to spectral fitting. The S4 chip is also destreaked[3]. Spectral fitting and analysis is performed with ISIS[4].

I employ a standard procedure for fitting the continuum in each of the three burst afterglows, and the theory is discussed in Section 5.3. I fit the dispersed gratings counts (summed ± 1 orders for the LETGS or summed HEG and MEG ± 1 orders for the HETGS) and the counts in 0th order by jointly minimizing χ^2, requiring a S/N of 3.5 or more per spectral bin. This translates into a requirement of 12 or more

[1]http://cxc.harvard.edu/ciao/
[2]http://asc.harvard.edu/cal/Acis/Cal_prods/qeDeg/
[3]http://asc.harvard.edu/ciao/threads/spectra_hetgacis/
[4]http://space.mit.edu/CXC/ISIS/

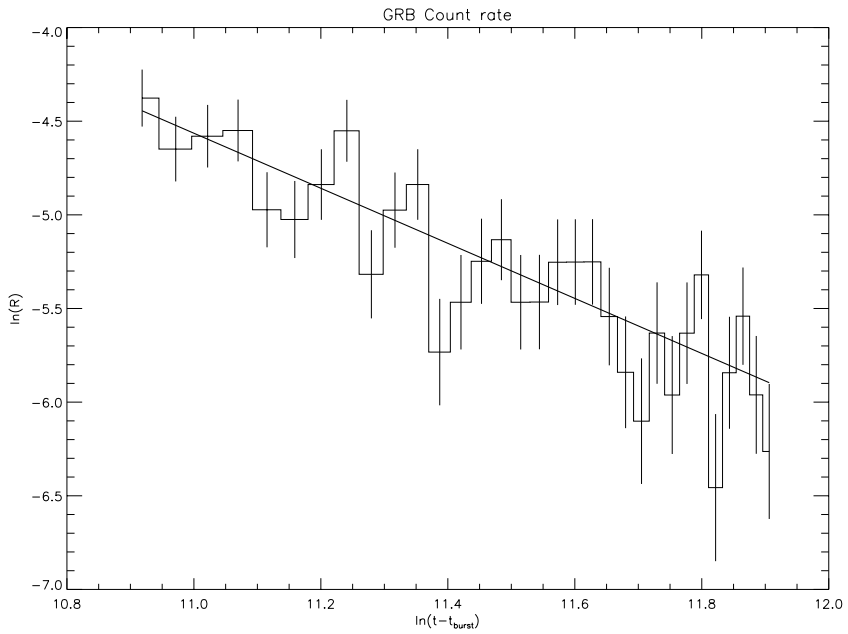

Figure 6-2: The afterglow count rate R fades approximately as a power-law with the time from the burst $t - t_{\rm burst}$. The best-fit temporal slope is $\alpha = -1.5 \pm 0.1$. The χ^2 is 34.27 for 30 degrees of freedom, and the fit is rejectable at only 73% confidence.

counts per spectral bin, as needed for Gaussian statistics to be valid. I have verified that this procedure yields continuum fits consistent with those for GRB 020813 and GRB 021004 reported in Section 5.3. It is useful to fit the 0th order simultaneously because of the wider energy range. I bin up the data only so much as necessary for Gaussian statistic to be valid so that discrete spectral features are as unlikely as possible to effect the continuum fits. In Section 6.4 I use the continuum models derived below to search for lines. Unless otherwise noted, all errors are at 90% confidence.

6.3.1 GRB 991216

The gratings and 0th order data are shown in Figure 6-3. In the 0.5 to 7.0 keV band, the data are rather poorly fit ($\chi^2_\nu = 114.3/86$, rejectable at 98% confidence) by an absorbed power-law with photon index $\Gamma = 1.9 \pm 0.2$ and a line of sight column density $N_H = (3.1 \pm 0.7) \times 10^{21}$ cm^{-2}, consistent with the Galactic value in the source direction. As suggested by Piro et al. (2000), the fit is improved at approximately 3.1σ significance ($\Delta\chi^2 = 20.51$ for 6 additional degrees of freedom) with the addition

of a recombination edge (best fit threshold energy 4.5 keV, plasma temperature 7.3 keV, and normalization 1.1×10^{-4} photons cm^{-2} s^{-1}) and an emission line (best fit energy 3.4 keV, width 39 eV, and flux 7.8×10^{-14} erg cm^{-2} s^{-1}). Individually, each feature only improves the fit at $\sim 2\sigma$ significance, somewhat in contrast to the claims of Piro et al. (2000), where the edge alone was reported to have significance 2.8σ. In that work, it appears that the line was fit using the gratings data alone, while the resulting power-law plus line model was then fit to the 0th order data alone to derive the edge parameters. Nonetheless, the energies derived for these two features are consistent with those reported by Piro et al. (2000). Please refer to Piro et al. (2000) for the detailed discussion and interpretation of these features. Both are argued to be due to Fe at $z \sim 1$. Using the power-law plus Gaussian plus edge model, the time-averaged integrated afterglow flux in the 0.5 to 7.0 keV band is found to be 2.7×10^{-14} erg cm^{-2} s^{-1}. The power-law portion of this model will be used for the line searches in Section 6.4. The model $N_H = 3.8 \times 10^{21}$ cm^{-2} and $\Gamma = 2.2$. This is the same Γ value found and used by Piro et al. (2000), and the N_H value is consistent with the value used there.

6.3.2 GRB 020405

The gratings and 0th order data are shown in Figure 6-4. In the 0.4 to 6.3 keV band, the data are moderately well fit ($\chi^2_\nu = 140.7/124$, rejectable at 86% confidence) by an absorbed power-law with photon index $\Gamma = 2.0 \pm 0.2$. I find a line of sight column density $N_H = (2.4 \pm 0.5) \times 10^{21}$ cm^{-2}. These values are consistent with those reported by Mirabel et al. (2002a). The column density is larger than the Galactic value in the source direction (4.3×10^{21} cm^{-2}) at 7.5σ significance ($\Delta\chi^2 = 65.6$ for 1 additional degree of freedom). The time-averaged integrated afterglow flux in the 0.4 to 6.3 keV band is found to be 9.5×10^{-15} erg cm^{-2} s^{-1}.

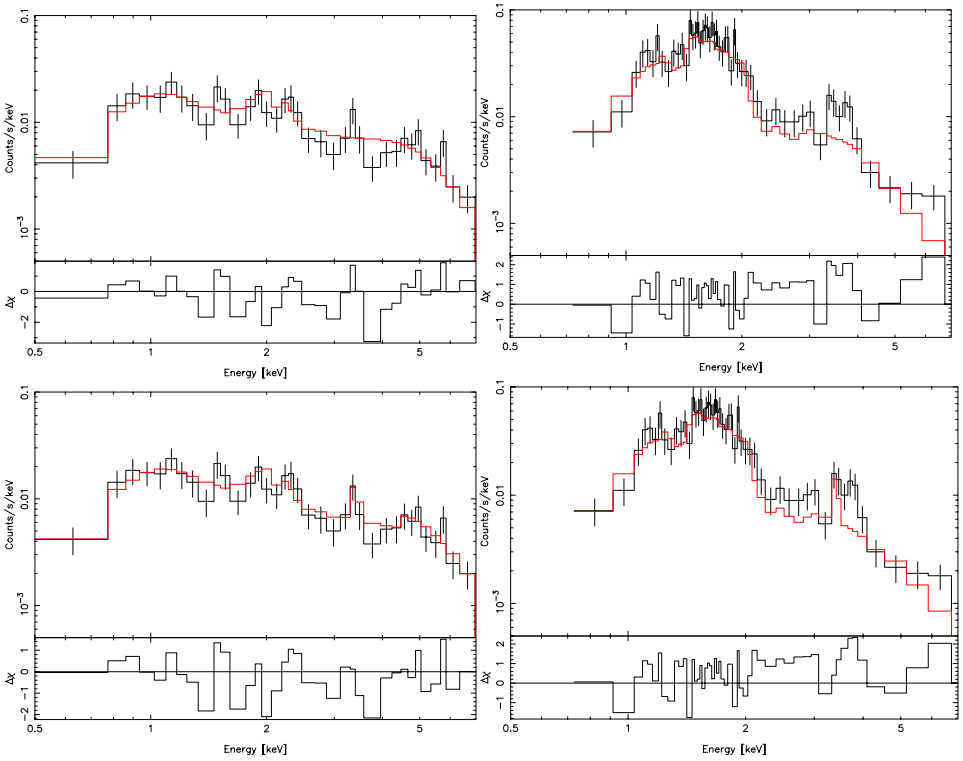

Figure 6-3: In the top two panels, the best-fit power-law model for GRB 991216 is plotted on top of the 0th order (left plot) and HETGS (right plot) data. In the bottom two panels, the power-law plus Gaussian plus edge model is plotted on top of the 0th order (left plot) and HETGS (right plot) data. Notice that the line (near 3.4 keV) appears to be broader in the HETGS data than in the 0th order data.

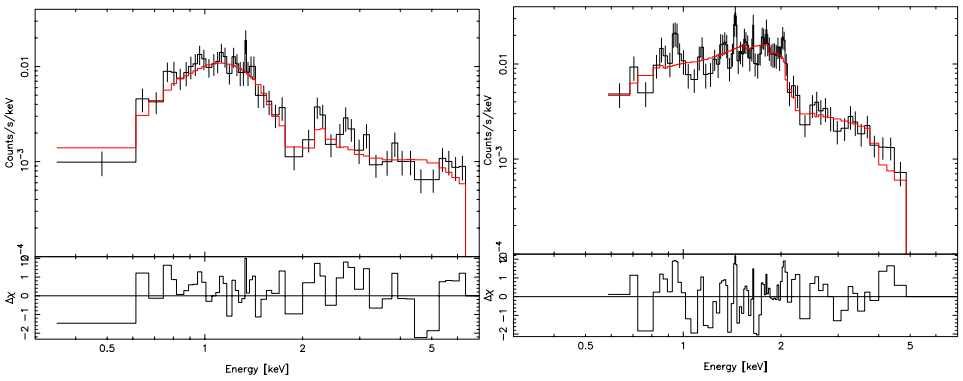

Figure 6-4: The best-fit power-law model for GRB 020405 is plotted on top of the 0th order (left plot) and HETGS (right plot) data.

6.3.3 GRB 030328

The gratings and 0th order data are shown in Figure 6-5. In the 0.3 to 5.7 keV band, the data are well fit ($\chi^2_\nu = 53.95/59$, rejectable at only 34% confidence) by an absorbed power-law with photon index $\Gamma = 2.1 \pm 0.2$. I find a line of sight column density $N_H = (9 \pm 5) \times 10^{20}$ cm^{-2}, consistent with the anticipated Galactic absorption in the source direction. These errors are 90% confidence 1-parameter confidence intervals. The time-averaged integrated afterglow flux in the 0.3 to 5.7 keV band is found to be 2.4×10^{-15} erg cm^{-2} s^{-1}.

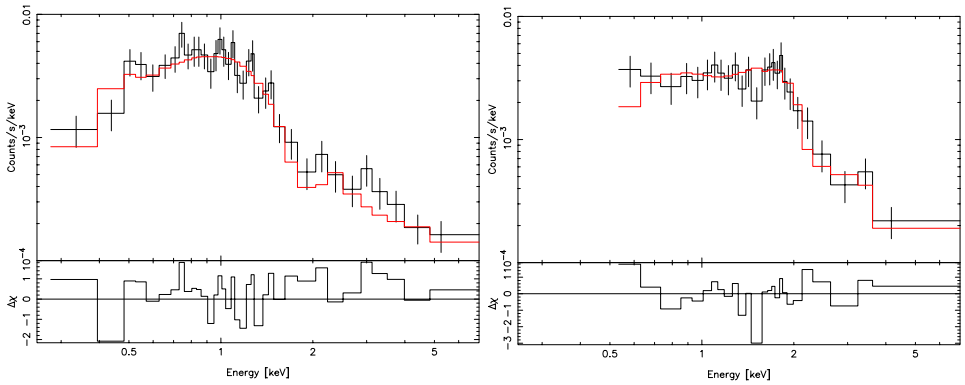

Figure 6-5: The best-fit power-law model for GRB 030328 is plotted on top of the 0th order (left plot) and HETGS (right plot) data.

6.4 Line Searches

6.4.1 GRB 991216

Figure 6-6 displays the power-law model found above over-plotted on the summed HEG+MEG counts, at three binnings as was done for GRB 020813 and GRB 021004 in Section 5.3.3. Eleven bins in the vicinity of the Fe line feature are observed to fluctuate beyond the 3σ significance for a single trial. The highest significance is 5σ in the bottom panel. In Section 6.3, the best fit line model was derived from joint fits to the gratings and 0th order data, and this was observed to be narrower than the HETGS residuals. This effect is also apparent from Figure 6-7, where the

line appears to be narrow in the MEG +1 order, whereas it is broad in the other gratings spectra. Conservatively, one can be confident that the bin at 3.63 Å in the middle panel of Figure 6-6 contains a real signal. The single-trial significance of the fluctuation in that bin is 4.9σ, and the significance for 239 bins (as are in Figure 6-6) is $> 3.7\sigma$. To establish a very tight, conservative bound, I use the pure power-law model from Section 6.3. The significance of the line is then found to be 2.9σ (4.3σ single trial). Background is negligible underneath the line, and I conclude that the line is robustly detected. Finally, fluctuations over 3σ in four bins near the Fe edge feature are observed, and the highest single-trial significance is 3.9σ. It is difficult to verify the reality of this feature, because of the lack of counts in each of the four independent spectra shown in Figure 6-7. Also, I find no evidence for a potential feature due to H-like S near 7 Å, as reported in Piro et al. (2000).

6.4.2 GRB 020405

Figure 6-8 displays the power-law model found above for GRB 020405 over-plotted on the LETGS counts, at three binnings. I consider wavelengths out to 26 Å. The LETGS is preferred to the HETGS for GRBs with hosts at $z > 1$. In particular, there is more sensitivity to the Kα lines from S and Si. The binnings in Figure 6-8 are approximately those for which lines were found and reported by Butler et al. (2003h) for the *Chandra* HETGS spectrum of GRB 020813 (at $z_{\rm eff} = 0.99$). At the time of the *Chandra* observation, no redshift was known for GRB 020405, and it was later established that $z = 0.695$ (Masetti et al., 2002). Between 1 and 26 Å, there are five bins in Figure 6-8 with fluctuations more significant than 3σ (single trial). The most significant (3.7σ) occurs in the top panel near 8.55 Å. A feature near 6 Å is found in the bottom (3.1σ) and middle (3.4σ) panels. Finally, features near 13.2 Å (3.6σ, bottom panel) and 14.45 Å (3.1σ, bottom panel) are found. None of these individually have N-trial confidences greater than 98%. The feature near 8.55 Å is not present in both orders of the LETGS (Figure 6-9), and I conclude that this feature is not a valid spectral line. The three remaining features can be identified with Kα transitions in Ar (Ar XVIII) and Mg (Mg XI and Mg XII), consistent with

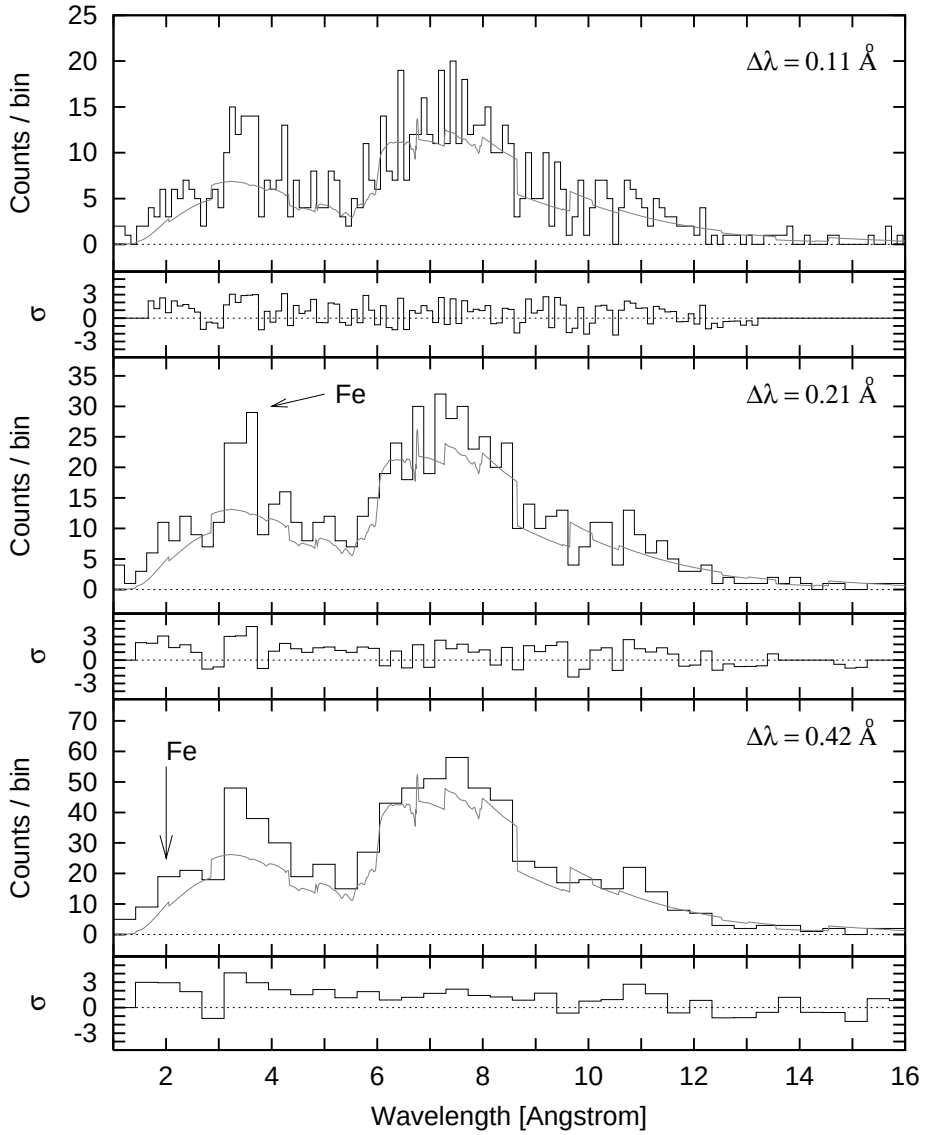

Figure 6-6: The best fit power-law model on top of the combined HETGS (MEG and HEG ± 1 order) data, at 3 binnings, for GRB 991216. The significance (reported in σ units) of deviations from the model are calculated using Poisson statistics. The Fe line is clearly observed near 3.6 Å, and the edge appears to be present as well (near 2 Å in the bottom plot).

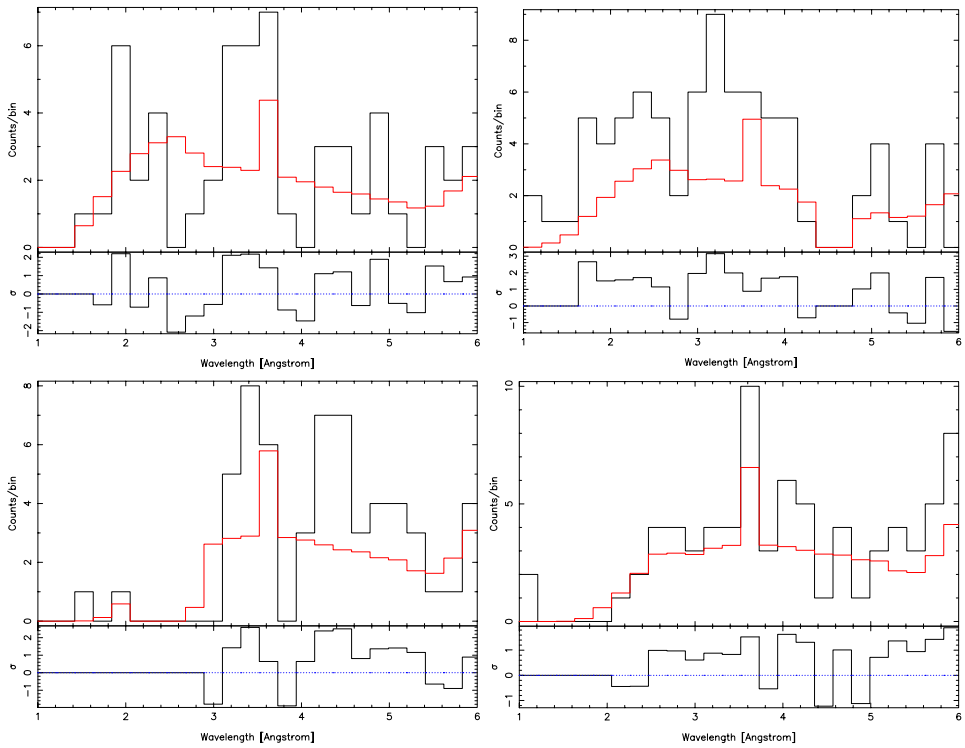

Figure 6-7: The power-law continuum plus Gaussian line plus edge model from Section 6.3 for GRB 991216 are plotted over the data at 0.21 Å binning for each of the four independent spectra. From top left to bottom right, the plots are of the HEG minus and plus orders and the MEG minus and plus orders. Notice that the model (which was derived from joint fits to the 0th order and gratings data) for the line is narrower than the residuals for all but the MEG +1 order data. The fluctuation at that wavelength bin is likely real.

$z = 0.63 \pm 0.03$. This identification requires a modest blue-shift ($v/c = 0.04 \pm 0.02$) from the host redshift. Upper limits on line luminosities and line equivalent widths are presented in Mirabel et al. (2002a). Though I have found possible faint spectral lines, I concur with Mirabel et al. (2002a) that no moderate or high significance discrete features are present in these data.

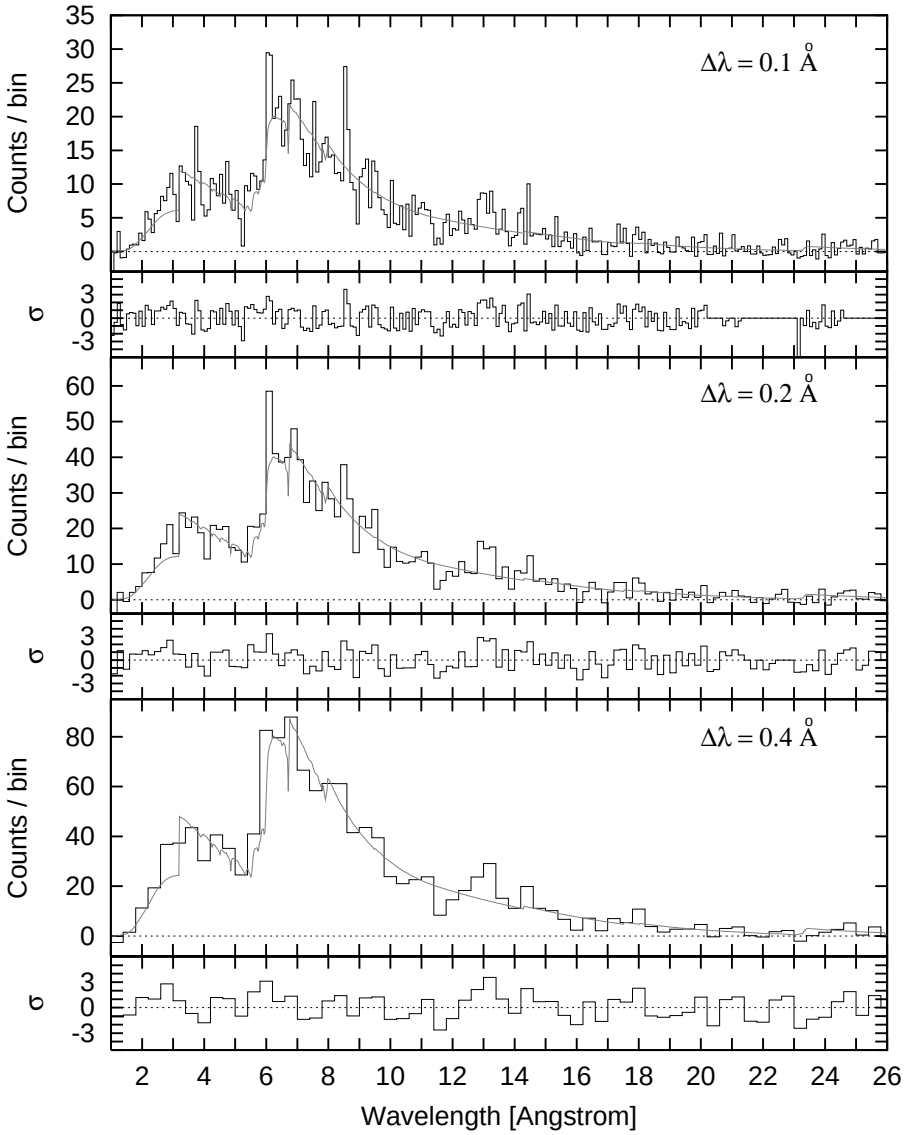

Figure 6-8: The best fit power-law model on top of the combined LETGS ±1 order data, at 3 binnings, for GRB 020405. The significance (reported in σ units) of deviations from the model are calculated using Poisson statistics.

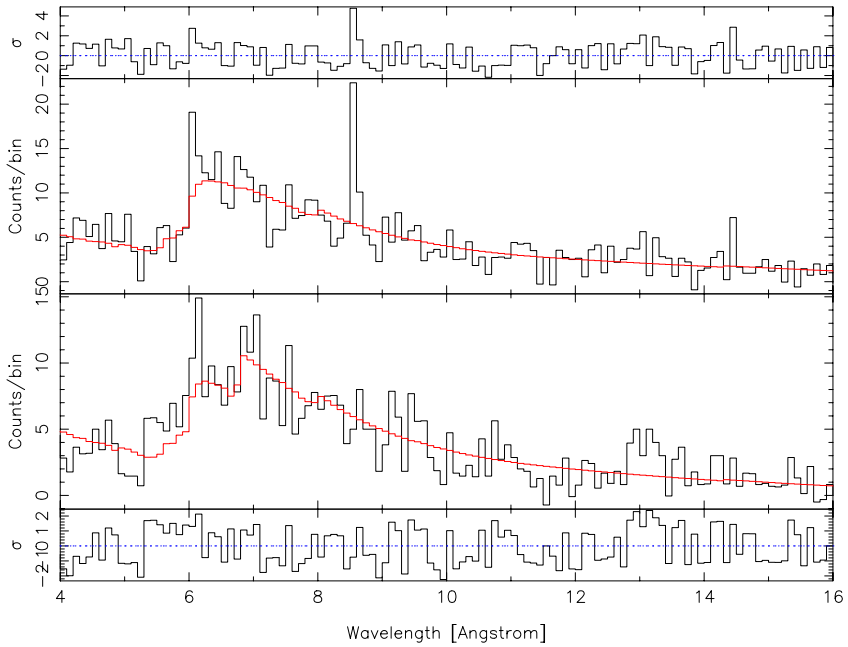

Figure 6-9: For 0.2 Å binning, the ±1 orders of the LETGS for GRB 020405 are plotted separately. The feature near 8.5 Å is present only in the +1 order (top plot). The feature near 6 Å is present in both orders.

6.4.3 GRB 030328

Figure 6-10 displays the power-law model found above over-plotted on the LETGS counts, at three binnings. Between a 1 and 26 Å, the most significant fluctuation (4.9σ) occurs at 23.1 Å in the middle plot of Figure 6-10. This feature is also present in the top (2.3σ) and bottom (3.5σ) plots. Two additional bins fluctuate at approximately the 3σ level. These are both in the top panel of Figure 6-10 (5.45 Å and 19.65 Å). There is a 50% chance that a 3σ fluctuation should occur at random (from $P_N = 1 - (1 - P)^N$) in one or more of the 249 bins in that panel. Moreover, as the features are seen in only one panel, they are likely noise. The probability for a chance fluctuation at the 4.9σ level in one of the 124 bins in the middle panel is, however, quite low (roughly 1 in 10^4).

An absorption redshift $z \geq 1.52$ has been determined for the optical afterglow of GRB 030328 by Martini, Garnavich, & Stanek (2003). At this redshift the possible line discussed in the preceding paragraph is identified with the Kα transition of He-like Mg, Mg XI (rest-frame wavelength 9.168 Å). Holding the best-fit power-law model

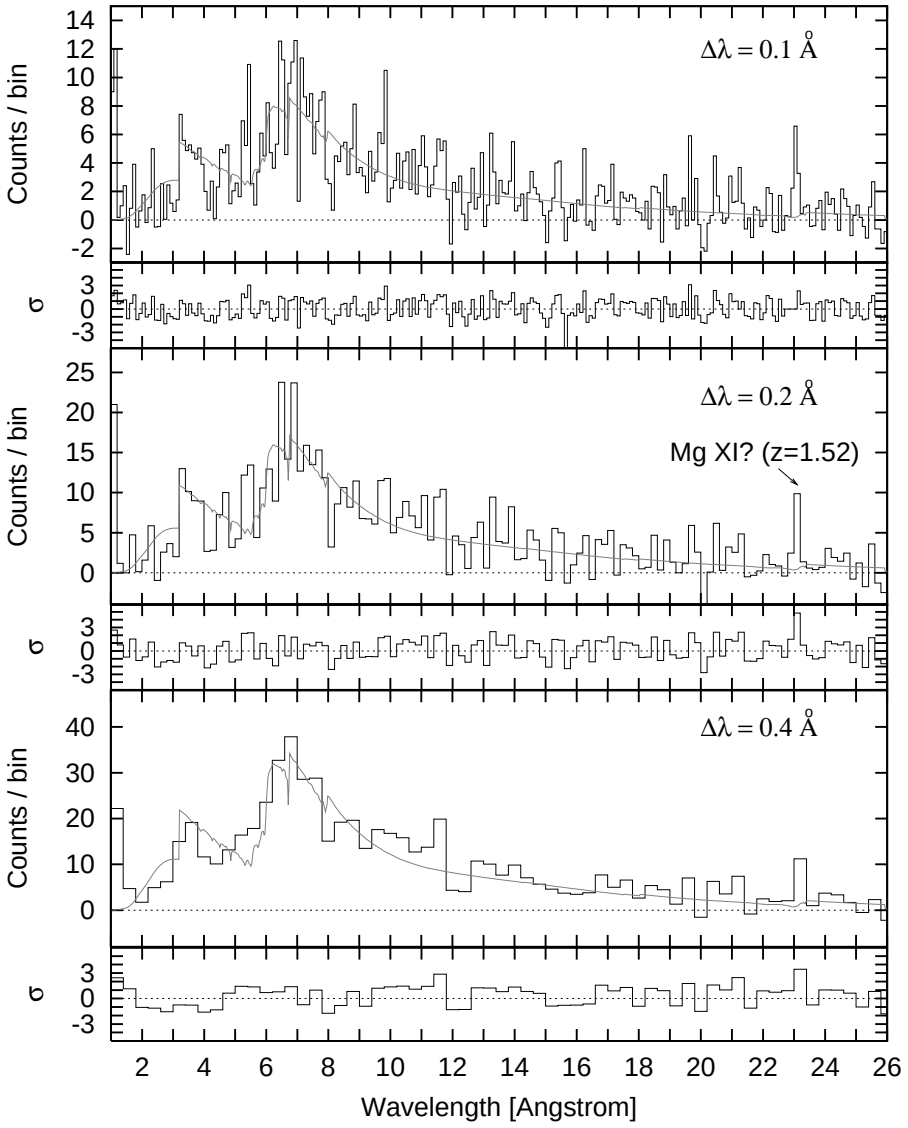

Figure 6-10: The best fit power-law model on top of the combined LETGS ±1 order data, at 3 binnings, for GRB 030328. The significance (reported in σ units) of deviations from the model are calculated using Poisson statistics. I associate the residuals near 23.1 Å in each of the three plots with with He-like Mg.

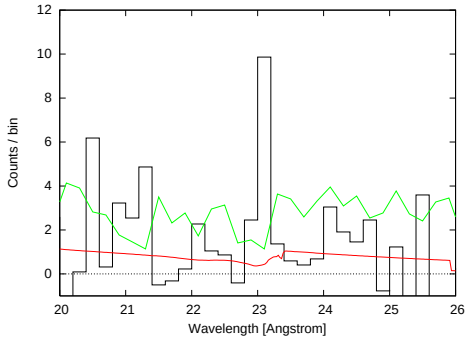

Figure 6-11: Background fluctuations dominate in the vicinity of the proposed Mg XI line. For 0.2 Å binning, the data, model (smooth curve) and background (jagged curve) are plotted. The background has been smoothed over ten 0.025 Å bins.

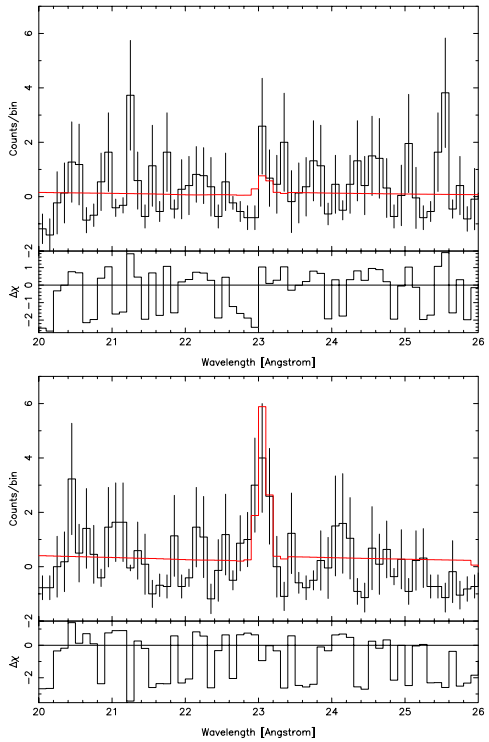

Figure 6-12: Most of the Mg XI line counts (10 of 11.6) come from the LETGS +1 order (bottom plot). This is consistent with the difference in instrumental effective areas between the −1 and +1 orders (top and bottom plots, respectively) as can be seen from the best fit continuum plus Gaussian model.

parameters fixed, and fitting a Gaussian to the data in the top panel of Figure 6-10 by minimizing the Cash (1979) statistic, the line flux is $1.5^{+1.3}_{-0.5} \times 10^{-14}$ erg cm^{-2} s^{-1}, while the width is $0.06^{+0.04}_{-0.02}$ Å, and the centroid wavelength is 23.1 ± 0.1 Å. The identification of the line with Mg XI implies a redshift for the X-ray afterglow of $z = 1.52 \pm 0.01$, consistent with the absorption system detected in the optical.

Ion	$E_{\rm line}$ (keV)	$L_{\rm line}(\times 10^{44}$ erg s$^{-1})^a$	EW (eV)^b
Ni_XXVIII	8.074	≤ 0.8	≤ 280
Co_XXVII	7.502	≤ 0.8	≤ 260
Fe_XXVI	6.953	≤ 0.8	≤ 250
Fe_XXV	6.701	≤ 0.8	≤ 240
Ca_XX	4.100	≤ 0.6	≤ 120
Ca_XIX	3.903	≤ 0.2	≤ 40
Ar_XVIII	3.319	≤ 0.2	≤ 30
Ar_XVII	3.140	≤ 0.6	≤ 90
S_XVI	2.613	≤ 0.7	≤ 100
S_XV	2.462	≤ 0.7	≤ 90
Si_XIV	2.001	≤ 1.0	≤ 120
Si_XIII	1.865	≤ 1.3	≤ 140
Al_XIII	1.729	≤ 1.1	≤ 110
Mg_XII	1.472	≤ 1.2	≤ 110
Mg_XI	1.353	≤ 1.3	≤ 100

Table 6.2: 90% confidence upper limits to the rest-frame equivalent widths and line luminosities for Kα lines of several ions.

[a] Isotropic luminosity calculated using a cosmology with $h = 0.65$, $\Omega_\Lambda = 0.7$, and $\Omega_m = 0.3$. I have used $z = 1.52$ for the host galaxy.

[b] The rest-frame equivalent width estimates have been made using a delta function line model and dividing by the continuum at the line energy.

As shown in Figure 6-12, the net counts from the possible Mg XI line come almost entirely from the LETGS +1 order. Unfortunately, this precludes a consistency check between the two independent spectra. The proposed Mg XI feature is quite close to the detector Oxygen K-edge, though this is likely to be only a small effect. More importantly, it is apparent from Figure 6-11 that fluctuations in the background dominate any fluctuations in the source continuum underneath the line. Thus, the question of whether or not the line is real is essentially a question of whether or not

the background has been estimated properly. From Figure 6-12, it appears that we may have wound up by chance with a low estimate for the background. In that plot, there are approximately 10 line counts over 0.5 counts in the model and an estimated 1.1 counts in the background. It is apparent that the background frequently is as high as 4 counts. Using this value, the single-trial significance of the line decreases from 4.9σ to 2.7σ, and no detection can be claimed.

In Table 6.2, I derive 90% confidence upper limits to the line luminosities and rest-frame equivalent width for Kα lines of several ions. These are determined by fitting a delta function line model at each energy to the data as reduced in Section 6.3. Comparing to Figure 5-7, these line luminosity limits are lower than the luminosities of several bright line reported in the literature. The limits are, however, not strong enough to rule out the presence of faint line like those detected in the spectrum of GRB 020813 (Section 5.3.3).

6.5 Summary

Afterglow Source	Lines Detected	$z_{\mathrm{x-ray}}$	z_{optical}	Significance
GRB 991216	Fe (I–XXVI)	~ 1	≥ 1.02	$> 3.7\sigma$
GRB 020405	Ar XVIII, Mg XI, Mg XII	0.63 ± 0.03	0.695	$< 2\sigma$
GRB 030328	Mg XI	1.52	≥ 1.52	$< 1\sigma$

Table 6.3: In the above table, lines detected in the spectra of GRB 991216, GRB 020405, and GRB 030328 are shown along with the implied redshift ($z_{\mathrm{x-ray}}$). This z can be compared to that measured in the optical (z_{optical}). For GRB 991216, the data do not constrain the ionization state of the candidate Fe line.

In the high-resolution X-ray afterglow spectra for three GRBs observed with *Chandra*, I have found extremely low significance evidence for lines in two bursts (GRB 020405 and GRB 030328) (Table 6.3). My results are consistent with their being no line emission in these spectra. I have found the Fe line claimed by Piro et al. (2000) to be moderately significant, roughly consistent with the determination ($> 4\sigma$) made by those authors.

Chapter 7

Conclusions

In the first part of thesis (Chapters 1 through 3), I discuss a suite of automated routines which have helped to verify *HETE*'s flight triggering and have helped to increase *HETE*'s burst yield by $\sim 15\%$. This software continues to run, and as long as the mission remains adequately staffed, its findings will continue to extend *HETE*'s burst yield. As data in the *HETE* archive continue to accumulate, archival searches for untriggered bursts will become increasingly interesting. My software should be very useful for conducting these. Also, hete_wave (Chapter 2) is a very powerful tool for determining burst statistics which will likely form the backbone of *HETE* GRB catalogs.

In the second part of the thesis (Chapters 4 through 6), I have focused on science results from following-up *HETE* GRBs in the X-rays with *Chandra*. We have detected an X-ray transient to an apparently optically dark burst (Section 4.2), and this position helped observers also detect a burst counterpart in the IR. I found no evidence for extinction in the X-ray data, and the afterglow was likely intrinsically faint in the optical. *HETE* appears to be solving the optically dark GRB phenomenon by showing that many GRBs appear to be "optically faint" (Section 4.2) instead. Here I am referring to long duration GRBs. Short GRBs may be optically dark because no (bright?) afterglow emission is present at any frequency.

Broadly, there are two classes of GRB progenitor models. The first involves the merger of two compact objects, either a black hole and a neutron star or two black

holes (see, e.g., Eichler et al., 1989). The strongest observational motivation for this type of progenitor is the delineation between short/hard GRBs and long/soft GRBs in the *BATSE* sample (Figure 1-2). Hurley et al. (2002) were able to derive upper limits for four short/hard GRBs, but those authors were unable to derive strict enough upper limits to exclude the fluxes typically reached by faint long/soft GRB afterglows. In Chapter 4, I discuss the best follow-up campaign to date of a short GRB. This has yielded observational support for the compact merger scenario, because our upper limits to the brightness of the GRB 020531 afterglow imply that the afterglow was likely intrinsically faint or that it faded very rapidly relative to what is typical for long/soft GRBs (Section 4.1.3). This is consistent with the notion that compact systems undergoing mergers ought to be situated in relatively clean environments.

In the second class of GRB progenitor models, the GRB arises due to the collapse of a massive star. In the "collapsar" picture (Woosley, 1993), the GRB jet punches through the surface of a massive star during a failed Type Ib or Ic SN. In the "supranova" picture (Vietri & Stella, 1998), a SN explosion leaves behind a rapidly spinning neutron star which spins down on the timescale of years and collapses to a Kerr black hole, generating a GRB. One striking difference between these two models is the presences of (or lack of) a significant time delay between SN and GRB. In Chapter 5, I discuss light metal lines from Si and S detected in the afterglow spectrum of GRB 020813. Much of my focus was on determining whether the lines are real or not. If they are real, then the implied stellar material rules out merger models. As I have discussed in Section 5.5, the longevity and narrowness of the lines implies a relatively old remnant as in the supranova picture, if we assume that these are due to geometrical effects. However, this two-step explosion scenario seems contrived, and it requires potentially large amounts of line-emitting material far away from the explosion site. Rather than having the line emission arise from material at $R \sim 10^{17}$cm, it seems more probable that lines from metals known to be present in the outer layers of massive stars ought to be produced at radii ($R \sim 10^{15}$cm) more like stellar radii. This is one reason to favor the single-step collapsar explosion picture, and we pointed out in Section 5.5 that the low line equivalent widths also possibly favor nearby reprocessor

models.

In Chapter 6, I carefully analyzed the X-ray afterglow spectra for GRB 991216, GRB 020405, and GRB 030328. I applied the methods used to find lines for GRB 020813, and I found no strong evidence for previously unclaimed features. Because no false alarms were raised, I am more confident in our detections for GRB 020813. The Fe line for GRB 991216 appears to be very real, independently confirming the claims of Piro et al. (2000). The Fe line for GRB 991216 is very strong (EW$\sim$ 500 eV) relative to the lines found in GRB 020813 (EW$\sim$ 50 eV), as shown in Figures 5-6, 5-7, and 5-8. Piro et al. (2000) argue that the line and emission edge are likely produced via photo-ionization in a scenario like that of the supranova (see also, Vietri et al., 2001). It is widely accepted, that the lines should be generated under photo-ionization (reflection). It is, however, disputed that the supranova picture is correct for this burst. Rees & Meszaros (2000) argue that nearby reprocessor models can equally well produce the observed Fe features. They envisage a "millisecond superpulsar" or a "highly magnetized torus around a black hole" which is active $\sim$1.5 days after the GRB has punched a whole through the outer layers of the massive progenitor star. If such an object could produce the high equivalent width line in GRB 991216, then it could also likely produce the lines in GRB 020813. For GRB 020813, the challenge would likely be in keeping the engine stable over the long line duration period ($\sim$1day).

Finally, Woosley (2003) has suggested a possibly simpler understanding. As the GRB jet works its way out of the progenitor star, mildly relativistic material accumulates behind the jet in a sort of "cocoon." This may mildly shock-up material from a Wolf-Rayet wind surrounding the progenitor star. Such a wind has been inferred from optical observations in the case of GRB 021004 (Mirabel et al., 2003). Delayed energy injection on the timescale of hours (from something like a jet cocoon perhaps) is claimed for this burst by Fox et al. (2003) from a shallow early decline in the optical afterglow light curve . If this delay can be days in the case of GRB 020813, and if the cocoon can stably power the lines for a day, then this understanding might be correct.

I have speculated a great deal in the closing of this section and in the closing of this thesis. Continued observations of GRB X-ray afterglows will be required before we can sure-footedly explore these realms of possibility.

Bibliography

Antonelli, L. A., et al. 2000, *The Astrophysical Journal*, 545, L39

Atteia, J-L. et al. 2003, in AIP Conf. Proc. 662, Gamma-Ray Burst and Afterglow Astronomy 2001, ed. G. Ricker, & R. Vanderspek (AIP Press: New York), 17

Atteia, J-L. et al. 2003a, *GRB Circular Network*, 2256

Ayani, K., & Yamaoka, H. 2003, *GRB Circular Network*, 2257

Ballantyne, D. R., et al. 2001, *The Astrophysical Journal*, 559, L83

Berger, E., et al. 2002, *The Astrophysical Journal*, 581, 981

Bloom, J. S., et al. 1999, *Nature*, 401, 453

Boer, M., et al. 2002, *GRB Circular Network*, 1408

Boer, M., et al. 2002a, *GRB Circular Network*, 1420

Borozdin, K. N., & Trudoyubov, S. P. 2002, astro-ph/0205208

Bourban, G. 2003, *GRB Circular Network*, 1820

Bromm, V. & Loeb, A. 2002, *The Astrophysical Journal*, 575, 111

Butler, N. R. et al. 2002, *GRB Circular Network*, 1272

Butler, N. R. et al. 2002a, *GRB Circular Network*, 1415

Butler, N. R. et al. 2002b, *GRB Circular Network*, 1426

Butler, N. R. et al. 2003a, *GRB Circular Network*, 2328

Butler, N. R. et al. 2003b, *GRB Circular Network*, 2347

Butler, N. R., et al. 2003c, in AIP Conf. Proc. 662, Gamma-Ray Burst and Afterglow Astronomy 2001, ed. G. Ricker, & R. Vanderspek (AIP Press: New York), 63

Butler, N. R. et al. 2003d, *GRB Circular Network*, 2269

Butler, N. R. et al. 2003e, *GRB Circular Network*, 2279

Butler, N. R. et al. 2003f, *GRB Circular Network*, 2007

Butler, N. R. et al. 2003g, *GRB Circular Network*, 2076

Butler, N. R., et al. 2003h, astro-ph/0303539, to appear in *The Astrophysical Journal*

Butler, N. R., & Doty, J. 2003, in AIP Conf. Proc. 662, Gamma-Ray Burst and Afterglow Astronomy 2001, ed. G. Ricker, & R. Vanderspek (AIP Press: New York), 45

Canizares, C. R., et al. 2002, *The Astrophysical Journal*, 539, L41

Cash, W. 1979, *The Astrophysical Journal*, 228, 939

Connaughton, V., et al. 1997, *International Astronomical Union Circular*, 6785

Costa, E., et al. 1997, *Nature*, 387, 783

Costa, E., et al. 1999, *Astronomy and Astrophysics Supplement*, 138, 425

Crew, G. B. et al. 2002, *GRB Circular Network*, 1734

Daubechies, I. 1988, Commun. Pure Appl. Math., 41, 909

Doty, J. et al. 2003, in AIP Conf. Proc. 662, Gamma-Ray Burst and Afterglow Astronomy 2001, ed. G. Ricker, & R. Vanderspek (AIP Press: New York), 38

Dullighan, A., et al. 2003, in press

Eichler, D., et al. 1989, *Nature*, 340, 126

Fishman, G. J., et al. 1989, in Proc. Gamma-Ray Observatory Science Workshop, ed. W. N. Johnson (Greenbelt: GSFC), 3

Ford, P. G., et al. 2003, *GRB Circular Network*, 2027

Fox, D. W., & Blake, C. 2002, *GRB Circular Network*, 1470

Fox, D. W. 2002a, *GRB Circular Network*, 1564

Fox, D. W. 2002b, *GRB Circular Network*, 1241

Fox, D. W. 2002c, *GRB Circular Network*, 1249

Fox, D. W. 2002, *GRB Circular Network*, 1731

Fox, D. W. 2002a, *GRB Circular Network*, 1427

Fox, D. W., et al. 2003, *Nature*, 422, 284

Frail, D. A., et al. 2001, *The Astrophysical Journal*, 562, L55

Frail, D. A., & Berger, E., et al. 2002, *GRB Circular Network*, 1418

Frail, D. A., & Berger, E., et al. 2003, *GRB Circular Network*, 2270

Freeman, P. E., Kashyap, V., Rosner, R., & Lamb, D. Q. 2002, *The Astrophysical Journal*, 138, 185

Galama, T., et al. 1998, *Nature*, 395, 670

Giblin, T. W., et al. 2002, *The Astrophysical Journal*, 570, 573

Graziani, C. 2003, in AIP Conf. Proc. 662, Gamma-Ray Burst and Afterglow Astronomy 2001, ed. G. Ricker, & R. Vanderspek (AIP Press: New York), 79

Greiner, J., Rau, A., & Klose, S. 2003, *GRB Circular Network*, 2271

Haar, A. 1910, Math. Ann., 69, 331

Halpern, J., et al. 2002, *GRB Circular Network*, 1578

Henden, A. 2003, *GRB Circular Network*, 2267

Holland, S. T., et al. 2002, astro-ph/0211094

Hurley, K., et al. 2002, *The Astrophysical Journal*, 567, 447

Hurley, K., et al. 2002a, *GRB Circular Network*, 1402

Hurley, K., et al. 2002a, *GRB Circular Network*, 1407

Hurley, K., et al. 2002a, *GRB Circular Network*, 1461

in't Zand, J. J. M., et al. 2003, astro-ph/0305361

Jager, R., et al. 1997, *Astronomy and Astrophysics Supplement*, 125, 557

Jansen, F. et al. 2001, *Astronomy and Astrophysics*, 365, L1

Kawai, N. et al. 2002, *GRB Circular Network*, 1816

Kawai, N. et al. 2003, in AIP Conf. Proc. 662, Gamma-Ray Burst and Afterglow Astronomy 2001, ed. G. Ricker, & R. Vanderspek (AIP Press: New York), 25

Khokhlov, A., et al. 1999, *The Astrophysical Journal*, 524, L107

Klebesadel, R. W., Strong, I. B., & Olson, R. A. 1973, *The Astrophysical Journal*, 182, L85

Kolaczyk, E. D. 1997, *The Astrophysical Journal*, 483, 340

Königl, A., & Granot, J. 2002, *The Astrophysical Journal*, 547, 134

Kouveliotou, C., et al. 1993, *The Astrophysical Journal*, 413, L101

Kraft, R., Burrows, D., & Nousek, J. 1999, *The Astrophysical Journal*, 374, 344

Kulkarni, S. R., et al. 1998, *Nature*, 395, 663

Kulkarni, S. R., et al. 1999, *Nature*, 398, 389

Kulkarni, S. R., et al. 2002, *GRB Circular Network*, 1428

Lamb, D. Q. 2000, *Physics Reports*, 333, 505

Lamb, D. Q., et al. 2002, *The Astrophysical Journal* (submitted)

Lamb, D. Q., & Reichart, D. E. 2000, *The Astrophysical Journal*, 535, 1

Lazzati, D. 2002, astro-ph/0210301

Lazzati, D., Ramirez-Ruiz E., & Rees, M. J. 2002, *The Astrophysical Journal*, 572, L57

Levan, A. et al. 2003, *GRB Circular Network*, 1818

Li, W., et al. 2003, *The Astrophysical Journal*, 586, L9

Malesani, D., et al. 2002, *GRB Circular Network*, 1500

Marshall, H. L., et al. 2002, *The Astrophysical Journal*, 564, 941

MacFadyen, A. I., Woosley, S. E., Heger, A. 2001, *The Astrophysical Journal*, 550, 410

Martini, P., Garnavich, P., & Stanek, K. Z. 2003, *GRB Circular Network*, 1980

Masetti, N., et al. 2002, *GRB Circular Network*, 1330

Meszaros, P. & Rees, M. 2001, *The Astrophysical Journal*, 556, L37

Metzger, M. R., et al. 1997, *Nature*, 387, 878

Miceli, A., et al. 2002, *GRB Circular Network*, 1416

Mirabel, N., et al. 2002, *GRB Circular Network*, 1618

Mirabel, N., et al. 2002a, astro-ph/0209516

Mirabel, N., et al. 2003, astro-ph/030361

Mirabel, N., & Halpern, J. 2003, *GRB Circular Network*, 2273

Monnelly, G. P. et al. 2001, *GRB Circular Network*, 1190

Monnelly, G. P. 2002, Ph.D. Thesis, MIT.

Paciesas, W., et al. 1999, *The Astrophysical Journal Supplement*, 122, 465

Park, H. S. et al. 2002, *GRB Circular Network*, 1736

Peterson, B. A., & Price, P. A. 2003, *GRB Circular Network*, 1974

Piro, L., et al. 1999, *Astronomy and Astrophysics Supplement*, 138, 431

Piro, L., et al. 2000, Science, 290, 955

Press, W. H., et al. P. 1997, Numerical Recipes in C (2d ed.; Cambridge: Cambridge University Press)

Price, P. A., et al. 2002, *GRB Circular Network*, 1475

Protassov, R., et al. 2002, *The Astrophysical Journal*, 571, 545

Rauscher, T., et al. 2002, *The Astrophysical Journal*, 576, 323

Reeves, J. N., et al. 2002, *Nature*, 415, 512 (R02)

Rees, M., Meszaros, P. 2000, *The Astrophysical Journal*, 545, L73

Reeves, J. N., et al. 2002, astro-ph/0206480

Reichart, D. E. 2001, *The Astrophysical Journal*, 554, 643

Reichart, D. E., & Price, P. A. 2002, *The Astrophysical Journal*, 565, 174

Ricker, G. R. et al. 2001, *GRB Circular Network*, 930

Ricker, G. R. et al. 2001a, *GRB Circular Network*, 1185

Ricker, G. R. et al. 2002, *GRB Circular Network*, 1229

Ricker, G. R. et al. 2002, *GRB Circular Network*, 1399

Ricker, G. R. et al. 2003, in AIP Conf. Proc. 662, Gamma-Ray Burst and Afterglow Astronomy 2001, ed. G. Ricker, & R. Vanderspek (AIP Press: New York), 3

Rosati, P., et al. 2002, *The Astrophysical Journal*, 566, 667

Rutledge, S., & Sako, M. 2002, *Monthly Notices of the Royal Astronomical Society* Submitted, (astro-ph/0206073)

Sahu, K. C., et al. 1997, *Nature*, 387, 476

Sako, M., & Harrison, F. A. 2002, *GRB Circular Network*, 1624

Sakamoto, T. 2003, private communication

Shirasaki, Y., et al. 2002, *GRB Circular Network*, 1565

Stanek, K. Z., et al. 2003, astro-ph/0304173

Stern, B. E., et al. 2001, *The Astrophysical Journal*, 563, 80

Strohmayer, T. E., et al. 1998, *The Astrophysical Journal*, 500, 873

Tavenner, T. et al. 2003, in AIP Conf. Proc. 662, Gamma-Ray Burst and Afterglow Astronomy 2001, ed. G. Ricker, & R. Vanderspek (AIP Press: New York), 97

Valentini, G., et al. 2003, *GRB Circular Network*, 2258

Vanderspek, R., et al. 2002, *GRB Circular Network*, 1504

Vanderspek, R., et al. 2003, in AIP Conf. Proc. 662, Gamma-Ray Burst and Afterglow Astronomy 2001, ed. G. Ricker, & R. Vanderspek (AIP Press: New York), 101

Vanderspek, R. et al. 2003a, *GRB Circular Network*, 1997

van Dyke, D. A., et al. 2001, *The Astrophysical Journal*, 548, 224

Vietri, M., & Stella, L. 1998, *The Astrophysical Journal*, 507, L45

Vietri, M., et al. 2001, *The Astrophysical Journal*, 550, L43

Villasenor, J., et al. 2002, *GRB Circular Network*, 1471

Villasenor, J., et al. 2003, in AIP Conf. Proc. 662, Gamma-Ray Burst and Afterglow Astronomy 2001, ed. G. Ricker, & R. Vanderspek (AIP Press: New York), 33

Villasenor, J., et al. 2003a, in AIP Conf. Proc. 662, Gamma-Ray Burst and Afterglow Astronomy 2001, ed. G. Ricker, & R. Vanderspek (AIP Press: New York), 107

Villasenor, J., et al. 2003b, *GRB Circular Network*, 2261

Villasenor, J., et al. 2003c, *GRB Circular Network*, 1978

Watson, D., et al. 2002, *Astronomy and Astrophysics*, 393, L1

Watson, D., et al. 2003, astro-ph/0306284

Weisskopf, M. C., et al. 2002, Publications of the Astronomical Society of the Pacific, 114, 1

Woosley, S. E. 1993, *The Astrophysical Journal*, 405, 273

Woosley, S. E. 2003, private communication

Woosley, S. E., & Weaver, T. A. 1995, *The Astrophysical Journal Supplement*, 101, 181

Woosley, S. E., Zhang, W., & Heger, A. 2003, in AIP Conf. Proc. 662, Gamma-Ray Burst and Afterglow Astronomy 2001, ed. G. Ricker, & R. Vanderspek (AIP Press: New York), 185

Wonziak, P. et al. 2002, *GRB Circular Network*, 1757

Yoshida, A., et al. 1999, *Astronomy and Astrophysics Supplement*, 138 433

Appendix A

Acronym List

4Br 4th BATSE Catalog (revised)
ACIS Advanced CCD Imaging System
AGN Active Galactic Nucleus
APED Astrophysical Plasma Emission Database
BATSE Burst and Transient Source Experiment
CCD Charge Coupled Device
CDFS Chandra Deep Field South
CIE Collisional Ionization Equillibrium
CME Coronal Mass Ejection
DAUB4 Daubechies 4-component Wavelet

DSP Digital Signal Processor
DV Data Variance
DWT Discrete Wavelet Transform
DXRB Diffuse X-ray Background
EPIC European Photon Imaging Camera
FFT Fast Fourier Transform
FRED Fast Rise Exponential Decline
FREGATE French Gamma-ray Telescope
FWHM Full Width at Half Maximum
FWZM Full Width at Zero Maximum
GCN GRB Coordinates Network
GRB Gamma-ray Burst
HEG High Energy Grating
HETE High Energy Transient Explorer
HETGS Hight Energy Transmission Grating
IDL Interactive Data Language
IPN Inter-Planetary Network
IR Infra-Red
LETGS Low Energy Transmission Grating

MCMC Markov Chain Monte Carlo
MEG Medium Energy Grating
MV Model Variance
PGS Primary Ground Station
PHA Pulse Heigth Analyzer
POS POSition histogram data
PSPC Position Sensitive Proportional Counter
QE Quantum Efficiency
RRC Radiative Recombination Continuum

S/N Signal over Noise Ratio
SAA South Atlantic Anomaly
SGR Soft-Gamma Repeater
SN Supernova
SOD Seconds of Day
STIS Space Telescope Imaging Spectrograph

SXC Soft X-ray Camera
TH Time-History data
TIPSH Translationally Invariant Poisson Smoothing using Haar wavelets
ToO Target of Oppurtunity
VHF Very High Frequency
WXM Wide Field X-ray Monitor
XRB X-ray Burst
XRF X-ray Flash